

QUANTITATIVE 3D IMAGING OF THE CRANIAL MICROVASCULAR ENVIRONMENT AT  
SINGLE-CELL RESOLUTION

by  
Alexandra Nicole Rindone

A dissertation submitted to Johns Hopkins University in conformity with the requirements for the  
degree of Doctor of Philosophy

Baltimore, Maryland  
February 2022

© 2022 Alexandra N. Rindone  
All rights reserved

# Abstract

Vascularization is critical for skull development, maintenance, and healing. Yet, there remains a significant knowledge gap in the relationship of blood vessels to cranial skeletal progenitors during these processes. One of the key challenges to studying the cranial microvascular environment is the lack of adequate imaging technologies to observe 3D cellular structures throughout the skull. The objective of this thesis is to engineer a platform to visualize and analyze the microvascular environment of the entire murine calvarium at single-cell resolution. In Aim 1, a quantitative light-sheet microscopy (QLSM) platform capable of imaging and quantifying cellular structures in the calvarium is developed by combining whole-mount immunostaining, optical tissue clearing, light-sheet microscopy, and advanced 3D image analysis. This platform is then applied to generate single-cell resolution 3D maps of blood vessel and skeletal progenitor subtypes in the frontoparietal bones. From these maps, it was discovered that Osterix<sup>+</sup> osteoprogenitors and Gli1<sup>+</sup> skeletal stem cells were spatially correlated with CD31<sup>hi</sup>Emcn<sup>hi</sup> vessels, especially inside and nearby the transcortical canals. Aims 2 and 3 build upon these findings by studying how the prevalence and spatial distribution of blood vessels and skeletal progenitors change during postnatal growth, remodeling, and healing. These Aims collectively show that the relationship between CD31<sup>hi</sup>Emcn<sup>hi</sup> vessels and skeletal progenitors is maintained during postnatal cranial bone growth, stimulated remodeling, and healing. However, this relationship is significantly weakened by conditionally knocking down platelet-derived growth factor-BB (PDGF-BB) in TRAP<sup>+</sup> preosteoclasts/osteoclasts, suggesting that these cells could play an important role in maintaining the cranial microvascular niche. These findings provide a foundational framework for understanding how blood vessels and skeletal progenitors spatially interact in cranial bone and will enable more targeted

studies into the mechanisms of skull pathologies and treatments. Additionally, the QLSM platform developed in this thesis can be readily adapted to study numerous cell types and investigate other elusive phenomena in cranial bone biology.

**Primary Reader and Advisor:** Warren Grayson, Ph.D.

**Secondary Reader:** Mei Wan, Ph.D.

**Thesis Committee:** Daniel L. Coutu, Ph.D., Warren L. Grayson, Ph.D., Scot C. Kuo, Ph.D., and Mei Wan, Ph.D.

# Acknowledgements

First and foremost, I am incredibly grateful for the assistance, guidance, and support of my mentors during my PhD studies. My PhD advisor, Professor Warren Grayson, has been instrumental to my success as a student and my growth as a scientist, offering invaluable guidance and support throughout my studies, and encouraging me to take risks with my projects. I am also thankful for the continued guidance of my thesis committee members. Professor Mei Wan provided our lab with invaluable insight into the fields of bone vascular and stem cell biology, helped us design and interpret our studies, and provided technical assistance with several of our experiments. Professor Daniel Coutu at the University of Ottawa generously allowed me to visit his lab in Canada for one month so that I could train on their specialized bone imaging and analysis techniques, and offered continued guidance during my thesis research. Professor Scot Kuo offered insight and advice that was instrumental in optimizing our light-sheet imaging set-up and image analysis pipeline. He also ensured that I had access to the computers and software necessary to analyze the large light-sheet datasets that were essential to my experiments.

I am also very grateful for the assistance of several other researchers involved in my studies. Xiaonan Liu devoted a lot of his time to my project, breeding the *Pdgfb<sup>CKO</sup>* mice and performing microCT scanning of all the calvaria analyzed in my experiments. Stephanie Farhat, Jasmine Hu, and other members of the Coutu lab were very generous with their time during my visit to the University of Ottawa, training me on essential techniques, providing assistance with the confocal microscope, and helping me navigate, explore, and enjoy the Ottawa region. I am incredibly thankful for their hospitality during my visit. Dr. Alexander Perdomo-Pantoja performed the cranial defect surgeries and has helped



me throughout my PhD studies with animal husbandry and surgeries. I am also appreciative of Dr. Timothy Witham for collaborating with our lab and providing essential resources that enabled us to perform the cranial defect surgeries with Dr. Perdomo-Pantoja. With respect to imaging and image analysis, Yuan Cai at the Integrated Imaging Center went out of her way to provide assistance throughout my study, offering training on the microscope, helping me troubleshoot issues with my imaging protocol, and checking the light-sheet alignment weekly to ensure that the microscope was working properly for my experiments. Dr. Hoku West-Foyle at the JHU SOM Microscope Facility provided training and valuable advice on the Imaris and Arivis Vision4D software packages. Shawna Snyder, a very talented Biomedical Illustrator and Animator, designed and produced the schematic of the cranial microvascular environment in Chapter 5 (Figure 5.1). Lastly, Professor Jennifer Elisseff provided valuable feedback and advice on our manuscript during the preparation process, and I am deeply appreciative of her time and support.

Outside of my thesis experiments, the kindness and support of many others has helped me stay motivated and succeed. My lab-mates have been very supportive in and outside of the lab, and have made my time in the Grayson Lab a wonderful experience! Ashley Farris, Ben Hung, Ethan Nyberg, Jordie Gilbert-Honick, Justin Morrissette, Pegah Abbasnia, and Sarah Somers were especially helpful in providing training, advice, and support during my first few years of graduate school. Additionally, I would like to specifically thank Allison Horenberg, who provided a lot of assistance with my experiments during the last stage of my PhD. I am also very grateful for the help of several current and former undergraduate students with my experiments: Athenia Jones, Ebuka Achebe, James Sooknanan, Mario Antoun, Maya Lapinski, Nicky Zhang, and Tanishk Sinha. I would like to thank several professors who provided generous support during my PhD: Dr. Feilim Gabhann, Dr. Arvind Pathak, and Dr. Jordan Green. Finally, I am deeply appreciative of several funding sources that supported me during my PhD: ARCS

Metropolitan Washington Chapter, Siebel Scholars Foundation, NCWIT Collegiate Award, NIH NIDCR F31 Predoctoral Fellowship (No. 5 F31 DE029109-02), and NSF Graduate Research Fellowship.

Lastly, I am very grateful to my family and my partner, Kyle Keraga, for their unwavering support throughout my PhD. From helping me edit my applications and personal statements, to patiently listening to me ramble about my research (even when it made no sense), to helping me get through the roughest times of my PhD, they have always been at my side and done everything they can to help me succeed. I would not be where I am today without their love, guidance, and support!

# Table of Contents

Abstract .....	ii
Acknowledgements .....	iv
List of Tables .....	x
List of Figures .....	xi
Introduction .....	1
Chapter 1 : Background .....	4
1.1 Skull anatomy and development.....	4
1.1.1 Anatomy .....	4
1.1.2 Development .....	7
1.2 Angiogenic-Osteogenic Coupling in Bone .....	10
1.2.1 Bone Blood Vessels and Their Relationship to Osteoprogenitors .....	10
1.2.2 Factors that Facilitate Angiogenic-Osteogenic Coupling in Bone .....	13
1.2.3 Angiogenic-Osteogenic Coupling in Cranial Bone .....	18
1.3 3D Bone Imaging Technologies.....	20
1.3.1 3D Tissue Sectioning and Immunohistochemistry .....	20
1.3.2 Intravital Microscopy .....	22
1.3.3 Tissue Clearing and Light Sheet Microscopy.....	23
1.3.4 Limitations in 3D Bone Imaging Technologies .....	24
Chapter 2 : Development of a Quantitative Light-sheet Microscopy (QLSM) Platform to Generate 3D Maps of the Cranial Microvascular Environment.....	26
2.1 Introduction .....	26
2.2 Methods.....	27
2.2.1 Materials.....	27
2.2.2 Study Approval.....	28
2.2.3 Experimental Animals .....	28
2.2.4 Murine Calvarial Harvest.....	28
2.2.5 Whole Mount Immunostaining and Optical Clearing .....	28
2.2.6 Light-sheet Imaging.....	29
2.2.7 Image Processing and Analysis .....	30
2.2.8 Statistics.....	31

2.3 Results.....	31
2.3.1 3D Quantitative Light-sheet Imaging of Murine Calvaria.....	31
2.3.2 3D Map of Calvarial Vessels and Skeletal Progenitors.....	35
2.4 Conclusion.....	37
Chapter 3 : Changes to the Cranial Microvascular Environment During Postnatal Cranial Bone Growth and Remodeling .....	38
3.1 Introduction .....	38
3.2 Methods.....	39
3.2.1 Materials.....	39
3.2.2 Study Approval.....	39
3.2.3 Experimental Animals .....	39
3.2.4 PTH Administration .....	39
3.2.5 Murine Calvarial Harvest.....	40
3.2.6 Whole Mount Immunostaining and Optical Clearing .....	40
3.2.7 Light-sheet Imaging.....	40
3.2.8 Image Processing and Analysis .....	40
3.2.9 MicroCT Scanning.....	40
3.2.10 Statistics.....	41
3.3. Results.....	41
3.3.1 Post-natal Growth Shifts the Distribution of Vessel Phenotypes and Osterix+ Progenitors.....	41
3.3.2 PTH Stimulates Osterix+ Progenitor Proliferation, but Does Not Alter Vessel Phenotype Distribution .....	44
3.3.3 Loss of Preosteoclast PDGF-BB Secretion Decreases the Spatial Affinity of Skeletal Progenitors to CD31 <sup>hi</sup> Emcn <sup>hi</sup> Vessels.....	46
3.4 Conclusion .....	48
Chapter 4 : Relationship Between the Microvasculature and Skeletal Progenitors During Cranial Bone Healing .....	50
4.1 Introduction .....	50
4.1.1 Critical-Sized Defect Determination .....	51
4.1.2 Biology of Cranial Bone Healing .....	54
4.2 Methods.....	56

4.2.1 Materials.....	56
4.2.2 Study Approval.....	56
4.2.3 Experimental Animals .....	56
4.2.4 Calvarial Defect Procedure .....	56
4.2.5 Murine Calvarial Harvest.....	57
4.2.6 Whole Mount Immunostaining and Optical Clearing .....	57
4.2.7 Light-sheet Imaging.....	57
4.2.8 Image Processing and Analysis .....	57
4.2.9 MicroCT Scanning.....	58
4.2.10 Statistics .....	58
4.3 Results.....	58
4.3.1 CD31 <sup>hi</sup> Emcn <sup>hi</sup> vessels and Gli1+ progenitors infiltrate into calvarial defect following injury.....	58
4.3.2 Localized Defect Injury Stimulates Systemic Expansion of Gli1+ Progenitors in the Periosteum .....	59
4.4 Conclusion .....	62
Chapter 5 : Conclusions and Future Perspectives.....	64
5.1 Conclusions and Impact .....	64
5.2 Future Directions .....	70
5.2.1 Mapping Nerves and Immune Cells in Native and Injured Calvaria .....	70
5.2.2 Studying Cellular Response to Transplanted Stem Cells and Biomaterials During Cranial Bone Healing .....	71
5.2.3 Adapting Quantitative Light-sheet Microscopy to Study the Human Skull Microvasculature .....	72
Bibliography .....	74
Appendix I: Key Reagents and Resources .....	82
Appendix II: List of Publications .....	86

# List of Tables

<b>Table 1.1: Methods for imaging the bone microvascular environment in 3D. ....</b>	<b>25</b>
--	-----------

# List of Figures

Figure 1.1: Anatomy of the calvarium. ....	5
Figure 1.2: Layers of the adult calvarium and its surrounding tissues. ....	7
Figure 1.3: Developmental origins of the murine calvarium. ....	9
Figure 1.4: Long bone consists of two distinct subtypes of capillaries. ....	12
Figure 2.1: Quantitative 3D light-sheet imaging pipeline. ....	32
Figure 2.2: 3D light-sheet imaging of the murine calvarium at single-cell resolution. ....	33
Figure 2.3: Quantitative analysis pipeline for characterizing calvarial blood vessel phenotype and skeletal progenitor distribution in 3D. ....	34
Figure 2.4: 3D map of the microvascular environment in 4-week-old murine calvaria. ....	36
Figure 3.1: Changes in vessel phenotype and skeletal progenitor distribution following postnatal development. ....	42
Figure 3.2: Distribution of skeletal progenitors in different regions of the calvarium. ....	43
Figure 3.3: PTH administration increases the number of Osterix+ progenitors, but does not significantly affect Gli1+ progenitor number or CD31 <sup>hi</sup> Emcn <sup>hi</sup> vessel volume. ....	45
Figure 3.4: Knocking out PDGF-BB expression in TRAP+ osteoclasts decreases CD31 <sup>hi</sup> Emcn <sup>hi</sup> vasculature and their association with Osterix+ and Gli1+ skeletal progenitors. ....	47
Figure 3.5: Osteoclasts reside in the marrow cavities and transcortical canals. ....	48
Figure 4.1: CD31 <sup>hi</sup> Emcn <sup>hi</sup> vessels and skeletal progenitors expand and infiltrate into subcritical-sized defects during healing. ....	61
Figure 4.2: Localized calvarial injury stimulates systemic skeletal progenitor expansion. ....	62
Figure 5.1: Schematic representing the spatial distribution and prevalence of vessels and skeletal progenitors in the calvarium. ....	64
Figure 5.2: Application of QLSM to image nerves and macrophages in the calvarium. ....	71
Figure 5.3: Application of QLSM to study the interactions of transplanted stem cells and blood vessels following injury. ....	72

# Introduction

Vascularization is essential for the development, growth, and maintenance of craniofacial bone. Blood vessels provide oxygen and essential nutrients, support hematopoiesis, and transport hormones to and from the bone<sup>1</sup>. During development, vessels provide a template for mineralization during intramembranous and endochondral ossification of craniofacial bones<sup>2</sup>, and vascular abnormalities have been linked to craniofacial syndromes such as mandibular hypoplasia<sup>3</sup>, hemifacial microsomia<sup>4</sup>, cleft palate<sup>5</sup>, and craniosynostosis<sup>6</sup>. Furthermore, angiogenesis is necessary for bone formation during distraction osteogenesis<sup>7</sup> and defect healing<sup>8</sup> in the skull. However, there remains a significant knowledge gap in the relationship between blood vessels and osteoprogenitors during craniofacial bone growth, remodeling, and healing.

The distribution of craniofacial vessel subtypes and their spatial relationship to skeletal progenitors remains poorly understood due to a lack of adequate imaging technologies. Methods used in long bone involve slicing the tissue into thick sections (~100  $\mu\text{m}$ ) along its long axis, enabling visualization of cellular structures throughout the different anatomical regions of the bone. However, these techniques are difficult to adapt to craniofacial bone due to its irregular, curved geometry. As an alternative to tissue sectioning, intravital microscopy has been used to evaluate the microvascular environment in the calvarium. Using this method, studies have demonstrated that the majority of osteoblasts reside in close proximity (<10  $\mu\text{m}$ ) to vessels within marrow cavities<sup>9</sup> and that vessels deep within the marrow space exhibit less blood flow and oxygen tension than those near the endosteum<sup>10,11</sup>, an active site of bone remodeling. However, due to the inherent limitations of intravital microscopy, these studies were confined to imaging small regions ( $\text{mm}^2$  areas) and, and their results could not be extrapolated to different regions of the calvarium.



Recent developments in optical tissue clearing and light-sheet microscopy are a promising avenue for characterizing the microvascular environment of large, irregularly-shaped tissues such as the skull. Using these techniques, one can image bones in 3D at single-cell resolution<sup>12,13</sup>, providing a means of assessing cellular microenvironments within different anatomical regions of bone. However, the specific methods employed by these studies are limited to using endogenous fluorescence for labeling cellular structures and would not be capable of visualizing different vessel and cell types simultaneously. Furthermore, there remains a lack of quantitative methods to assess the 3D spatial relationships of cellular structures in large light-sheet imaging datasets (>100 GB). These shortcomings impair the otherwise-powerful ability of light-sheet imaging to study the relationship between vessel phenotypes and skeletal progenitors in the skull.

In this thesis, I present a 3D imaging platform that we developed to comprehensively study the microvascular environment in cranial bone. First, I provide an in-depth background on skull anatomy, angiogenic-osteogenic coupling in bone, and 3D bone imaging technologies and identify key knowledge gaps in the field. Then, I discuss the methods, results, and conclusions from my three thesis aims. In Aim 1, I develop a quantitative 3D imaging platform to visualize and quantify the cranial microvasculature and skeletal progenitors throughout the murine calvarium. Using this method, I create a 3D map of the different blood vessel and skeletal progenitor subtypes in the calvaria of juvenile mice (4-weeks-old) to evaluate how blood vessels spatially interact with skeletal progenitors during postnatal growth. In Aim 2, I build upon Aim 1 by studying how the prevalence and spatial distribution of blood vessels and skeletal progenitors changes following postnatal growth and after stimulation or suppression of bone remodeling activity. Finally, in Aim 3, I evaluate how different blood vessel and skeletal progenitor subtypes infiltrate and interact with each other in subcritical-sized cranial defects during healing. Together, these findings provide a foundational framework that will progress our knowledge of

craniofacial bone biology and inform the development of therapies to treat skull abnormalities and injuries.

# Chapter 1 : Background

In this chapter, I provide a background of critical concepts in my thesis research. First, I give an overview of the anatomy of the skull and describe what is known about its prenatal and postnatal development. Then, I provide a background on angiogenic-osteogenic coupling in bone and highlight the deficiencies in our knowledge about the cranial bone microvasculature. Lastly, I describe the current technologies used to image blood vessels, skeletal progenitors, and other cell types in bone, including a discussion of their advantages and limitations in the context of imaging cranial bone.

## 1.1 Skull anatomy and development

### 1.1.1 Anatomy

The human skull consists of 22 bones that are divided into two regions: the neurocranium and the viscerocranium<sup>14</sup>. The neurocranium, also known as the cranial bones, is the superior portion of the skull and serves as a protective barrier to the underlying brain<sup>14</sup>. By contrast, the viscerocranium makes up the facial bones and provides structural support for facial functions such as mastication<sup>14</sup>. This section primarily will focus on the anatomy and development of the neurocranium—particularly the calvarium—in humans and mice.

In humans, the neurocranium is made up of the calvarium (also known as the calvaria or cranial/skull vault) and the skull base<sup>15</sup>. The calvarium protects the brain and consists of frontal bones, parietal bones, and portions of the temporal and occipital bones, while the skull base enables the passage of neurovascular structures through the skull and consists of the ethmoid bone, sphenoid bone, and some portions of the occipital, frontal, and temporal bones<sup>15</sup>. The cranial bones are connected by the cranial sutures—stiff, fibrocartilaginous joints that affords slight movements between the interconnected bones<sup>16</sup>. In the calvarium, the bones are connected by the sagittal suture (parietal-

parietal), coronal suture (frontal-parietal), lambdoid suture (frontal-occipital), and squamous suture (parietal-temporal) (**Figure 1.1**)<sup>16</sup>. During early postnatal development, there is also a suture in between the two frontal bones called the metopic suture<sup>16</sup>. This suture fuses within the first year of birth, while the other cranial sutures fuse later in adulthood<sup>17,18</sup>.

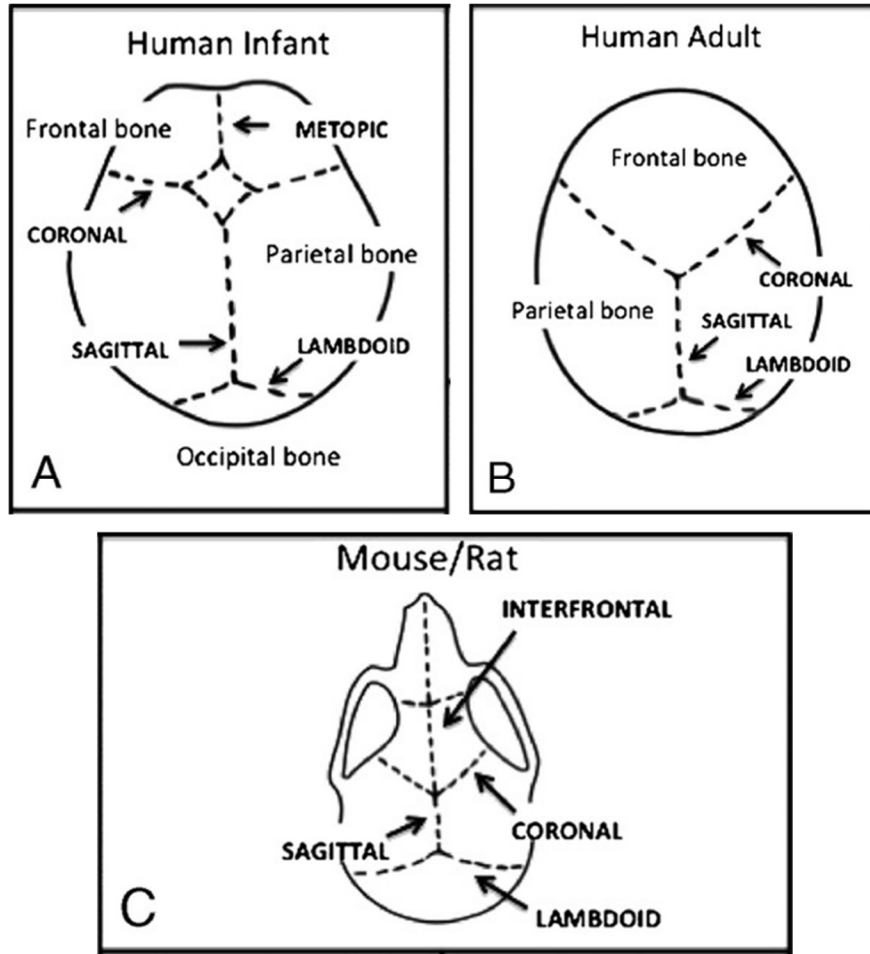


**Figure 1.1: Anatomy of the calvarium.** The bones and sutures are shown in the calvaria of a human infant, human adult, and mouse. The metopic and interfrontal sutures fuse during early postnatal development. Figure adapted from Grova *et al.* (Ref. 36).

While the structure of the murine calvarium is similar to that in humans, there are some differences. There is an extra bone between the occipital and parietal bones called the interparietal bone that is rarely present in the human skull<sup>19</sup>. Additionally, the suture between the two frontal bones is referred to as the interfrontal rather than the metopic suture; although, these sutures both fuse

during early postnatal development<sup>20</sup>. The other calvarial sutures in mice—coronal, sagittal, and lambdoid—do not fuse in adulthood and remain patent throughout their lifespan<sup>20</sup>.

Each bone in the calvarium contains common layers that span from the scalp to the brain (**Figure 1.2**). The periosteum, a fibrous tissue, is the superficial layer that extends across the surface of the cranial bones and is in contact with the scalp<sup>21</sup>. Likewise, the dura mater is a fibrous tissue that spans the endocranial surface of the bone and is connected to the brain<sup>22</sup>. Both of these tissues are highly vascularized and contain skeletal progenitor cells that may contribute to skull bone growth and repair; although the precise progenitor populations may be different between the periosteum and dura mater<sup>21,23,24</sup>. The cranial bone consists of two cortical plates that are separated by a porous trabecular layer—also known as the diploe—that contains bone marrow<sup>25</sup>. The cranial bone marrow is highly vascularized and contains numerous cell populations such as immune cells and skeletal progenitors. Within the cortical bone plates, there are emissary canals that connect blood vessels in the scalp to intracranial venous sinuses<sup>26</sup>. In addition, recent studies have identified small vascular channels—referred to as the transcortical canals in this thesis—that connect the vasculature of the skull bone marrow to the dura mater and periosteum and enable vascular-mediated transport of immune cells from the bone marrow to the brain<sup>27,28</sup>.

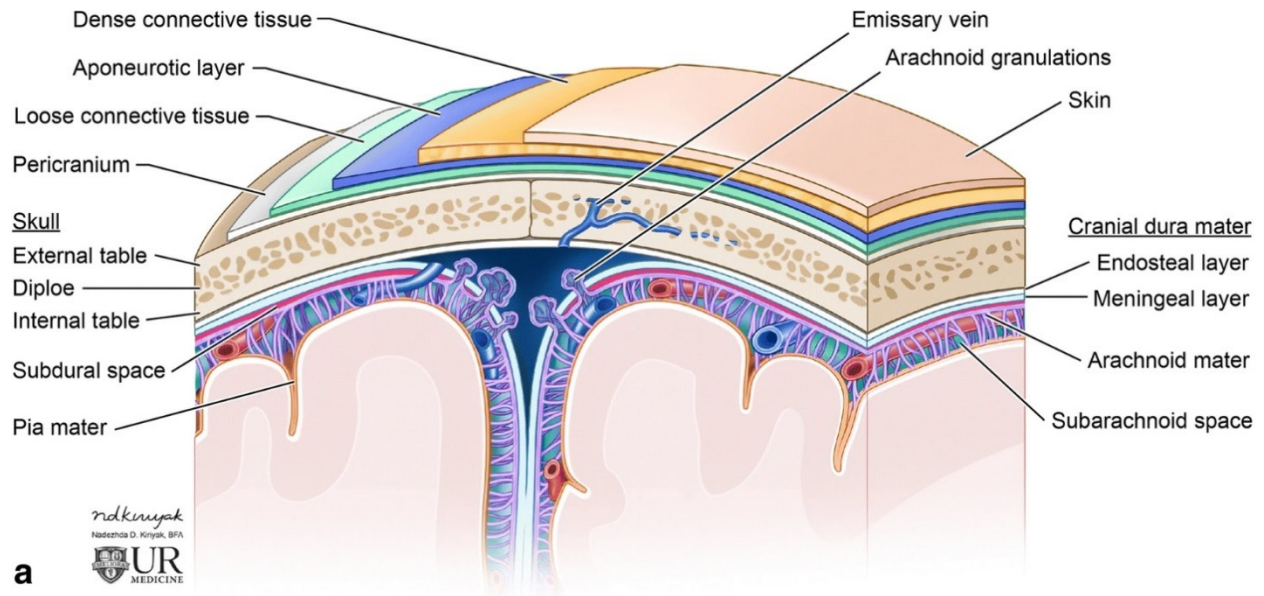


**Figure 1.2: Layers of the adult calvarium and its surrounding tissues.** The layers of the calvarium from the ectocranial to endocranial direction include the periosteum (also known as the pericranium), ectocranial cortical table, diploe (cancellous bone containing marrow), endocranial cortical table, and dura mater. The periosteum is adjacent to the connective tissues of the scalp while the dura mater is dually attached to the skull and the brain. The dura mater consists of conjoined endosteal and meningeal layers that are separated only at the superior sagittal sinus. Vasculature is present in all layers and is interconnected via transcortical vessels (bone marrow to periosteum/dura mater vessels) and emissary veins (periosteum to dura mater vessels). Figure adapted from Gomez *et al.* (Ref. 25).

### 1.1.2 Development

Calvarial bone grows and develops through intramembranous ossification<sup>29</sup>. This is a process by which mesenchymal stem cells condense and differentiate directly into osteoblasts to form new bone<sup>29</sup>. By contrast, the skull base and some facial bones form via endochondral ossification, a process by which bone forms through an intermediate cartilage template<sup>29</sup>. During embryonic development, mesenchymal cells migrate to the region between the surface ectoderm and brain, differentiate into osteoblasts, and undergo ossification and mineralization<sup>30</sup>. These ossification centers mineralize apically and laterally to form the flat bones of the calvarium<sup>31</sup>. Once the leading edges of adjacent bones approach each other, the sutures develop to form a flexible fibrocartilaginous joint between the bony structures<sup>32</sup>. The leading edges of the bone that are connected to the sutures are called the osteogenic fronts and contain a rich source of osteoprogenitors that enable continued calvarial bone growth<sup>30</sup>. In

addition to providing mechanical flexibility to the developing skull, the sutures house cranial skeletal stem cells that provide a source of osteoprogenitors to the neighboring osteogenic fronts, periosteum, and dura mater and enable the sutures to remain patent during embryonic development<sup>33,34</sup>. As the bone and sutures develop, the fibrous membranes of the periosteum and dura mater grow around the bone and provide mechanical tension that displaces the bones and stimulates further bone growth<sup>30</sup>.

During postnatal development, calvarial growth continues into adulthood as the underlying brain expands<sup>35</sup>. Bone growth is stimulated by the expansion of the meninges and periosteum via mechanical tension placed on the sutures<sup>35</sup>. The mechanical strain stimulates bone formation at the osteogenic fronts while the width of the sutures remains constant, enabling cranial bone growth to continue as the brain expands<sup>35</sup>. During this process, the metopic suture (interfrontal suture in mice) fuses early during postnatal development, but the other calvarial sutures remain patent until adulthood in human and for the remainder of the lifespan in mice<sup>36</sup>. Along with growth at the osteogenic fronts, the calvarial bone expands and thickens apically through mineralization along the ectocranial surface and resorption at the endocranial surface<sup>35</sup>. Additionally, while most of the calvarial bone remains unicortical during fetal development, the diploe (bone marrow) form during postnatal development and divide the cortical bone into ecto- and endocranial layers<sup>32</sup>. These modeling and remodeling processes result in the formation of a thicker cortical table in the ectocranial versus endocranial portion of the bone<sup>32</sup>.

Although all calvarial bones grow through the intramembranous pathway, there are differences in their embryological origin (**Figure 1.3**). The parietal, occipital, and portions of the temporal bones originate from the mesoderm, while the frontal and other parts of the temporal bones come from the neural crest<sup>37</sup>. In mice, the interparietal bone has a mixed origin of neural crest and mesoderm-derived cells<sup>30</sup>.

The fibrous tissues of the calvarium also originate from different germ layers. The periosteum is and dura mater are generally derived from the same origin as the bone they surround<sup>30,38</sup>. By contrast, several of the cranial sutures originate at the neural crest-mesoderm boundary<sup>39</sup>. The sagittal and coronal sutures have different origins from their surrounding bone(s), originating from the neural crest and mesoderm, respectively<sup>39</sup>. However, the metopic/interfrontal suture—which fuses during early postnatal development and does not substantially contribute to postnatal cranial bone growth— is derived from the neural crest and is from the same origin as the adjacent frontal bones<sup>39</sup>. The origin of the lambdoid suture remains unknown, and it is unclear whether this suture lies on the neural crest-mesoderm interface<sup>39</sup>.

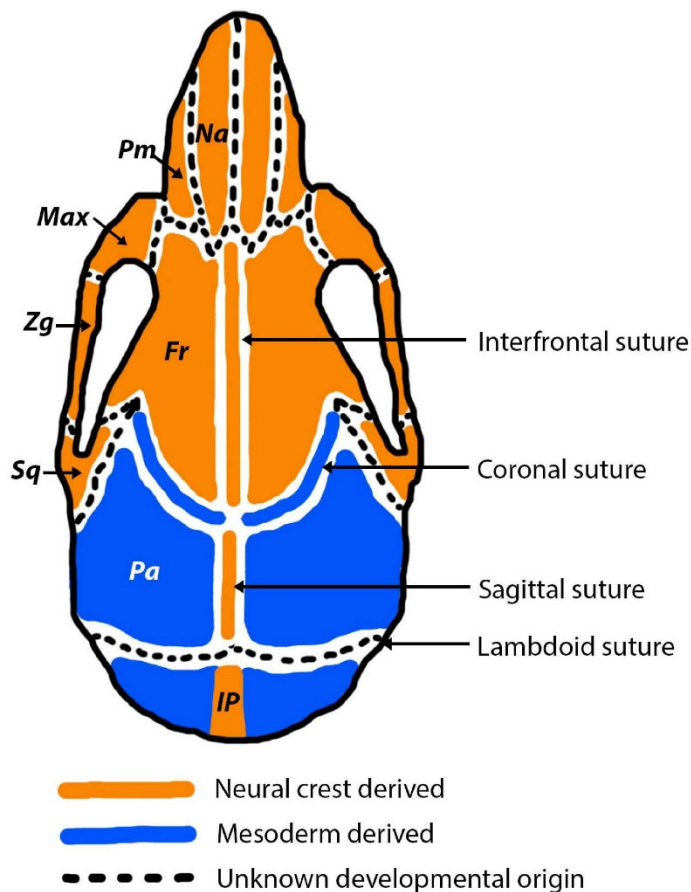


**Figure 1.3: Developmental origins of the murine calvarium.** The coronal suture, parietal bones, and most of the interparietal bone are derived from the neural crest (orange), while the interfrontal suture, sagittal suture, part of the interparietal bone, and frontal bones originate from the mesoderm (blue). The origin of the lambdoid suture is unknown (dotted lines). Figure adapted from White *et al.* (Ref. 39).



## 1.2 Angiogenic-Osteogenic Coupling in Bone

Bone is a highly vascularized tissue, receiving approximately 10-15% of the total cardiac output in humans<sup>40</sup>. Blood vessels are prevalent throughout the different regions of the bone, including the periosteum, bone marrow, and cortical bone, and they serve multiple functions that contribute to proper bone growth and maintenance<sup>1</sup>. As in other organs, blood vessels provide oxygen and nutrients and remove waste to enable proper cellular metabolism<sup>1</sup>. They also deliver soluble signals transmitted by other tissues, such as growth factors, hormones, and neurotransmitters, and contribute to hematopoietic stem cell maintenance and mobilization<sup>1,41</sup>. With respect to osteogenesis, blood vessels are known to engage in bi-directional signaling with osteoprogenitors/osteoblasts and provide signaling cues necessary for bone development and healing—a process referred to as angiogenic-osteogenic coupling<sup>42</sup>. This section will provide an overview of angiogenic-osteogenic coupling in bone—with most of the focus on long bone—and discuss the knowledge gaps that remain with respect to the relationships between blood vessels and osteoprogenitors/osteoblasts in cranial bone.

### 1.2.1 Bone Blood Vessels and Their Relationship to Osteoprogenitors

Vascularization is an essential process that occurs in coordination with osteogenesis during bone development and healing. Since the 1980s, it has been presumed that blood vessels act as a scaffold for mineralization and is critical for osteogenesis<sup>43-45</sup>. One of the first models for angiogenic-osteogenic coupling was proposed by *Caplan, 1991* based on experimental observations from a chick tibia during development<sup>46</sup>. In this model, osteoblasts secrete osteoid to form the first mineral layer in the developing bone, followed by the invasion of capillaries<sup>46</sup>. Then, osteoblasts in the adjacent region deposit osteoid in the direction opposite of the capillaries, resulting in an additional mineral layer that forms around the capillaries and connects to the first layer<sup>46</sup>. This process continues to occur as the bone develops—with the vasculature serving as a template for mineralization—and enables the

formation of highly structured lamellar bone<sup>47</sup>. While this model lacked mechanistic insight, it established the importance of studying the spatial relationships between the bone vasculature and osteoprogenitors/osteoblasts.

Wang *et al.* (2007)<sup>48</sup> was the first to identify a direct molecular link between angiogenesis and osteogenesis during bone development. In this study, they used the Cre-lox system (a recently established technology at the time) to conditionally knock out von Hippel-Lindau (VHL) in osteoblasts to evaluate the effects of HIF-1 $\alpha$  signaling on angiogenic-osteogenic coupling (HIF-1 $\alpha$  is an oxygen-sensing protein that is known to stimulate angiogenesis in tissues under hypoxic conditions by upregulating VEGF expression<sup>49</sup>). They targeted VHL because it tags HIF-1 $\alpha$  for proteasomal degradation, and disrupting its expression would result in increased HIF-1 $\alpha$  signaling in osteoblasts<sup>49</sup>. Using this transgenic mouse model, they found a significant increase in localized VEGF production, vascularization, and mineralization in long bones, suggesting that HIF-1 $\alpha$  signaling was stimulating angiogenesis and osteogenesis<sup>48</sup>. Knocking down HIF-1 $\alpha$  expression in osteoblasts decreased vascular and bone mineral volume, further confirming this relationship<sup>48</sup>. To determine whether HIF-1 $\alpha$  was stimulating osteogenesis through a cell autonomous or non-autonomous mechanism, they knocked down VHL in mouse primary osteoblasts and cultured them *in vitro*<sup>48</sup>. Disrupting VHL expression did not affect *in vitro* osteoblast proliferation, apoptosis, osteogenic gene expression, or mineralization<sup>48</sup>. Taken together, these results demonstrated that HIF-1 $\alpha$  signaling in osteoblasts enhanced mineralization through cell-nonautonomous mechanisms and coupled angiogenesis to osteogenesis in long bone.

While Wang *et al.* demonstrated that angiogenesis is directly coupled to osteogenesis in bone, the precise roles of blood vessels in stimulating bone growth was still unknown. A pair of papers by Kusumbe *et al.*<sup>50</sup> and Ramasamy *et al.*<sup>51</sup> in 2014 discovered two distinct subtypes of capillaries in long bone and unveiled how one of these subtypes directly couples angiogenesis to osteogenesis during bone growth. To identify the distinct types of bone vasculature, they established a protocol that enabled 3D

visualization and analysis of the long bone microvasculature in  $\sim 100 \mu\text{m}$  thick sections<sup>52</sup>. Using this technique, they discovered two different types of capillaries—termed “Type H” and “Type L”—that could be readily distinguished through their levels of CD31 and Endomucin (Emcn) expression<sup>50</sup> (**Figure 1.4**). Type H vessels were high in CD31 and Emcn expression, had a columnar morphology, were located nearby sites of active mineralization (metaphysis and endosteum), and had higher metabolic and angiogenic activity<sup>50</sup>. Furthermore, they were spatially associated with osteoprogenitors and osteoblasts ( $\sim 70\text{-}80\%$  osteoprogenitors/osteoblasts within  $20 \mu\text{m}$  of a Type H vessel) and expressed higher levels of genes associated with osteoprogenitor survival and proliferation<sup>50</sup>. By contrast, Type L vessels were low in CD31 and low/medium in Emcn expression, had a sinusoidal morphology, were located in the bone marrow (diaphysis), and were not spatially associated with osteoprogenitors<sup>50</sup>.

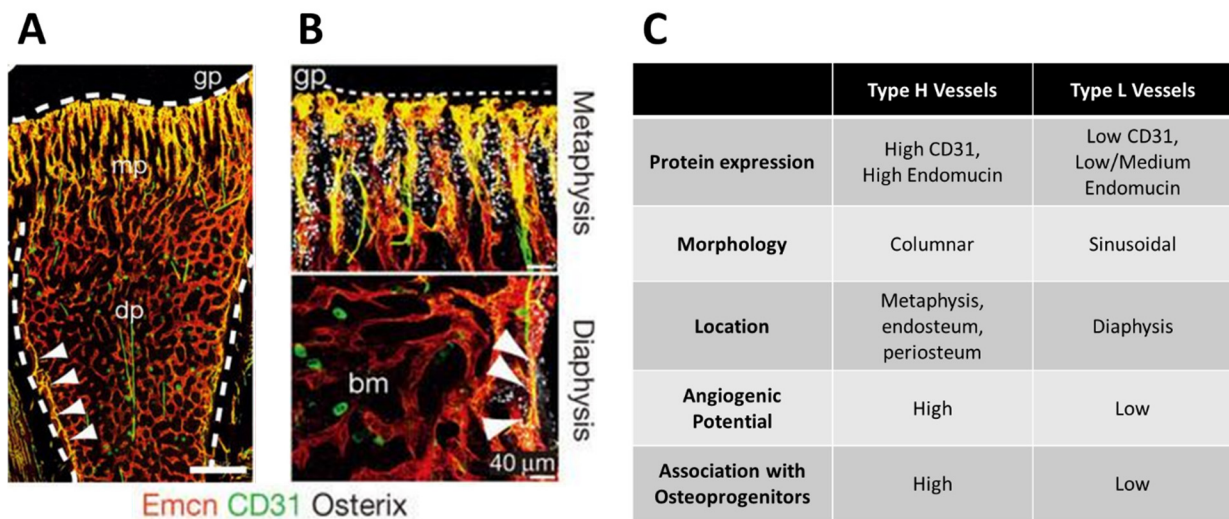


**Figure 1.4: Long bone consists of two distinct subtypes of capillaries.** **A** Blood vessel subtypes in long bone, as denoted through their levels of CD31 (green) and Endomucin (Emcn, red) expression. **B** Relationship of blood vessel subtypes with Osterix+ osteoprogenitors (grey). CD31<sup>hi</sup>Emcn<sup>hi</sup> vessels in the metaphysis and endosteum (white arrowheads) are spatially correlated with osteoprogenitors. **C** Characteristics of Type H and Type L vessels. Scale bars:  $300 \mu\text{m}$  (**A**),  $40 \mu\text{m}$  (**B**) Images and information in the table are adapted from Kusumbe *et al.* (Ref. 50).

To determine whether Type H vessels were coupled to osteogenesis, they performed experiments that targeted Notch activity in bone endothelial cells, as Notch is known to regulate angiogenesis in various organs and tumors<sup>51,53</sup>. Using models that conditionally knocked down genes in

endothelial cells to inhibit or promote Notch signaling (*Rbpj*<sup>iΔEC</sup> and *Fbxw7*<sup>iΔEC</sup>, respectively), they found that Notch signaling is necessary for Type H vessel growth, growth plate maintenance, and mineralization in the metaphysis<sup>51</sup>. By contrast, knocking down Notch activity in osteoblasts had a negligible effect on bone vasculature, growth plate morphology, and mineral density, demonstrating that osteogenesis was dependent on endothelial cell-autonomous Notch signaling<sup>51</sup>. To understand this mechanism, they quantified the expression of angiocrine factors in the endothelial cells and found that *Noggin* was the most upregulated gene when Notch signaling was stimulated (compared *Fbxw7*<sup>iΔEC</sup> and control endothelial cells)<sup>51</sup>. Administration of recombinant *Noggin* protein for two weeks in 15-day-old mice restored the Type H vasculature, growth plate morphology, and mineralization rate in *Rbpj*<sup>iΔEC</sup> mice, demonstrating that this molecule was a critical factor in coupling angiogenesis to osteogenesis in long bone<sup>51</sup>. Taken together, these papers established a pivotal framework for how blood vessels interact with osteoprogenitors in bone and have enabled new lines of investigation into the angiogenic-osteogenic coupling processes during bone development, remodeling, and healing.

## **1.2.2 Factors that Facilitate Angiogenic-Osteogenic Coupling in Bone**

While these studies establish the initial framework for how angiogenesis is coupled to osteogenesis in bone, numerous signaling cascades, cell types, and physiological processes are known to influence these processes. Here, I provide an overview of the key factors known to facilitate angiogenic-osteogenic coupling in long bone: preosteoclast and osteoclast signaling, HIF-1 $\alpha$  signaling, and blood flow-induced shear stress on endothelial cells.

### *1.2.2.1 Preosteoclast and Osteoclast Signaling*

Osteoclasts are bone-resorbing cells that are formed by monocyte/macrophage lineage precursors first differentiating into TRAP<sup>+</sup> mononuclear preosteoclasts, and then fusing to become terminally differentiated, multinucleated cells<sup>54</sup>. While it has been known for decades that osteoclasts

resorb bone and are essential for modeling and remodeling<sup>54</sup>, recent evidence has demonstrated that they also play important roles in angiogenic-osteogenic coupling.

Several studies have shown that preosteoclasts promote angiogenesis and osteogenesis in long bone. In a seminal study done by Xie *et al.* (2014)<sup>55</sup>, it was discovered that TRAP+ preosteoclasts promote CD31<sup>hi</sup>Emcn<sup>hi</sup> vessel formation during modeling and remodeling via secretion of platelet-derived growth factor-BB (PDGF-BB). To identify this effect, they first cultured monocytes and macrophages, preosteoclasts, and osteoclasts *in vitro* and isolated their conditioned medium to evaluate their effect on mesenchymal stem cell (MSC) and endothelial progenitor cell (EPC) migration<sup>55</sup>. They found that preosteoclasts—but not monocytes/macrophages or osteoclasts—significantly increased MSC and EPC migration via secretion of PDGF-BB<sup>55</sup>. To study this effect *in vivo*, they employed a conditional knockout mouse model targeting PDGF-BB in the TRAP+ cell lineage (Pdgfb<sup>CKO</sup> model), including preosteoclasts<sup>55</sup>. They found that knocking down PDGF-BB in TRAP+ preosteoclasts reduced CD31<sup>hi</sup>Emcn<sup>hi</sup> vessel amount in the periosteum and bone marrow, trabecular bone volume percentage and thickness, and cortical bone thickness<sup>55</sup>. By contrast, stimulating PDGF-BB secretion in preosteoclasts or administering exogenous PDGF-BB to the bone marrow increased the amount of CD31<sup>hi</sup>Emcn<sup>hi</sup> vessels and bone formation<sup>55</sup>. Collectively, these results demonstrated that PDGF-BB secreted by preosteoclasts is necessary for the coupling of CD31<sup>hi</sup>Emcn<sup>hi</sup> vessels to osteogenesis during long bone modeling and remodeling<sup>55</sup>. In addition, recent studies have discovered other beneficial and pathological effects of preosteoclasts on angiogenic-osteogenic coupling: Preosteoclast-derived PDGF-BB was necessary for recruitment of periosteal progenitor cells during cortical bone growth and healing<sup>56</sup>, while excess levels of PDGF-BB secreted by preosteoclasts in the subchondral bone induced aberrant angiogenesis coupled with osteogenesis and accelerated osteoarthritis<sup>57</sup>.

Besides preosteoclasts, a special subset of terminally-differentiated osteoclasts—called vessel associated osteoclasts (VAOs)—are important regulators of angiogenesis and osteogenesis during long

bone growth<sup>58</sup>. Compared to regular bone-resorbing osteoclasts, VAOs express lower levels of cathepsin K, are smaller in size, have fewer nuclei, and are spatially associated with sprouting blood vessels—rather than the lining of trabecular bone—nearby sites undergoing endochondral ossification<sup>58</sup>. Romeo *et al.* (2019)<sup>58</sup> demonstrated that Type H vessels rather than VAOs were responsible for degrading growth plate cartilage during postnatal bone growth—a finding that contradicted previous assumptions that osteoclasts were responsible for growth plate matrix degradation. However, VAOs were essential for regulating the growth of Type H vessels: Depleting VAOs resulted in reduction of the anastomosing bulges of Type H vessels and malformation of the growth plate.

Another recent study by Liu *et al.* (2021)<sup>59</sup> discovered that metaphyseal osteoclasts (presumably VAOs) are also important for preventing senescence in Type H vessels. First, they found that glucocorticoid treatment—a regimen known to decrease bone mineral density—induced Type H endothelial cell senescence<sup>59</sup>. To determine the mechanisms of glucocorticoid-induced senescence, they then screened for angiogenic molecules in bone tissue extracts and found a significant reduction in angiogenin secretion—a protein that was primarily expressed by VAOs in the primary spongiosa<sup>59</sup>. Administering recombinant angiogenin reversed the effect of glucocorticoid-induced endothelial senescence and increased bone mineral density in the metaphysis, demonstrating the importance of this VAO-secreted molecule on bone angiogenesis and osteogenesis<sup>59</sup>.

While these studies demonstrate important roles for preosteoclasts and VAOs, it remains unclear whether the classic bone-resorbing osteoclasts are essential for angiogenic-osteogenic coupling. Some reports have suggested that osteoclasts stimulate angiogenesis via secretion of soluble factors<sup>60,61</sup>. However, other studies have shown that pharmacologically inhibiting osteoclast activity does not result in decreased vasculature and could even enhance the formation of Type H vessels<sup>58,62</sup>. These discrepancies may be attributed to differences in experimental design, such as the use of *in vitro* versus *in vivo* models, type of bone studied, and type of method employed to inhibit or stimulate osteoclast

activity. Future studies will be required to fully elucidate the roles, if any, of bone-resorbing osteoclasts in bone angiogenesis.

Besides osteoclasts, other cell types such as osteoblasts, sensory nerves, and macrophages provide critical signaling factors for bone angiogenesis. As discussed earlier, osteoblasts stimulate angiogenesis in long bone via HIF-1 $\alpha$ -mediated VEGF-A secretion<sup>48</sup>. In addition, a recent study conducted by Xu *et al.* (2018)<sup>63</sup> demonstrated that osteoblast-derived SLIT3—a proangiogenic factor—stimulated ROBO1 signaling in endothelial cells and was necessary for the formation of CD31<sup>hi</sup>Emcn<sup>hi</sup> vessels during bone development and healing. Several studies have also linked sensory nerves to blood vessel formation during bone development and fracture healing, demonstrating that nerves provide signaling cues that are important for proper bone angiogenesis<sup>64,65</sup>. Lastly, a study done by Stefanowski *et al.* (2019)<sup>66</sup> showed that macrophages released VEGF-A during the first few days of fracture healing and were important for stimulating CD31<sup>hi</sup>Emcn<sup>hi</sup> vessel infiltration into the injury site. However, further research is needed to determine the extent to which each of these cell types regulate angiogenic-osteogenic coupling during bone development, remodeling, and healing.

#### 1.2.2.2 HIF-1 $\alpha$ Signaling

As reviewed earlier, HIF-1 $\alpha$  activation in osteoblasts and hypertrophic chondrocytes induces VEGF expression and is critical for the coupling of angiogenesis of osteogenesis<sup>48,67</sup>. However, endothelial cell-autonomous HIF-1 $\alpha$  signaling is also essential for proper bone angiogenesis and osteogenesis. The importance of endothelial cell HIF-1 $\alpha$  activity was first illustrated in Kusumbe *et al.* (2014)<sup>50</sup>, where they employed loss and gain of function transgenic mouse models targeting the HIF-1 $\alpha$  pathway in endothelial cells. They found that knocking down HIF-1 $\alpha$  in endothelial cells decreased the amount of metaphyseal Type H vessels and number of osteoprogenitors, while knocking down VHL (to stimulate HIF-1 $\alpha$  signaling) had the reverse effect in the tibiae of 3-week-old mice<sup>50</sup>. Furthermore, stimulating HIF-1 $\alpha$  signaling via deferoxamine mesylate (DFM) treatment in 64- to 70-week-old mice led

to partial restoration of Type H vessels, osteoprogenitors, and bone volume in the metaphysis of the proximal tibia<sup>50</sup>. To determine the mechanism by which endothelial cell-autonomous HIF-1 $\alpha$  stimulates angiogenesis, they quantified endothelial cell gene expression in DFM-treated tibia and found that there was significantly increased expression of angiogenic transcription factors including *Pdgfa*, *Pdgfb*, and *Tgfb3*<sup>50</sup>. Collectively, these data suggested that HIF-1 $\alpha$  signaling stimulates Type H vessel angiogenesis through endothelial cell-autonomous signaling.

While hypoxia is known to be a main driver of HIF-1 $\alpha$  activation, studies have shown that other stimuli may also be involved in maintaining endothelial cell-autonomous HIF-1 $\alpha$  signaling. In a recent study done by Sivaraj *et al.* (2020)<sup>68</sup>, it was found that knocking down Yap/Taz signaling in endothelial cells stimulated angiogenesis of Type H vessels—a trend that is opposite of observations in other organs with Yap/Taz signaling. To study the mechanism behind this result, they performed RNA-sequencing on Yap1/Taz <sup>$\Delta$ EC</sup> endothelial cells and found significant reductions to HIF-1 $\alpha$  target genes<sup>68</sup>. Additionally, they knocked down HIF-1 $\alpha$  along with Yap/Taz in endothelial cells and found that it negated the effects of Yap/Taz on Type H vessel formation, suggesting that crosstalk between these two pathways is important for bone angiogenesis<sup>68</sup>. In a separate study performed by Yang *et al.* (2017)<sup>69</sup>, they found that expression of a specific set of microRNAs, miR-497~195, in Type H endothelial cells was important for stimulating HIF-1 $\alpha$  signaling and maintaining bone angiogenesis and osteogenesis. Taken together, these studies demonstrate that multiple signaling mechanisms besides hypoxia likely affect HIF-1 $\alpha$  activity in Type H endothelial cells.

#### 1.2.2.3 Blood flow

Blood flow in bone blood vessels is correlated with compromised fracture healing and loss of bone mass during aging. Higher levels of blood flow have been documented in bone fractures at the early stages of healing, while non-unions have been associated with lower blood flow at the fracture site<sup>70-72</sup>. Lower blood flow has also been associated with the development of osteoporosis during



aging<sup>73</sup>. However, despite these observations, it has remained unknown what mechanisms were behind the relationship between blood flow and angiogenic-osteogenic coupling.

To investigate how blood flow affects bone angiogenesis and osteogenesis, Ramasamy *et al.* (2016)<sup>62</sup> mapped the blood flow in murine long bones and evaluated the effects of reducing flow locally in the bone. They found that Type H vessels had significantly higher blood flow and expression of shear stress-associated genes compared to Type L vessels<sup>62</sup>. Reducing bone blood flow via femoral artery ligation or prazosin administration resulted in a reduction of endothelial shear stress and Notch gene expression, Type H vessel amount, osteoprogenitor number, and metaphyseal bone volume<sup>62</sup>. However, overexpression of notch protein NICD in endothelial cells reversed these trends, demonstrating that Notch signaling served as an essential link between Type H vessel blood flow and angiogenesis<sup>62</sup>. To investigate whether blood flow was linked to age-related vascular changes, they compared the vasculature between 4-, 12-, and 80-week-old mice and found that blood flow and Notch signaling was reduced with age. However, this trend could be reversed by administration of alendronate, a drug commonly used to treat osteoporosis<sup>62</sup>. These results demonstrate how blood flow regulates angiogenic-osteogenic coupling and provide potential avenues for developing therapeutics that target the vasculature to treat osteoporosis.

### **1.2.3 Angiogenic-Osteogenic Coupling in Cranial Bone**

While similarities exist between cranial and long bones, they differ by their anatomy, developmental origins, and growth mechanisms. Long bone originates from the mesoderm and develops through an endochondral pathway, while cranial bone comes from both the neural crest and mesoderm and develops through the intramembranous ossification mechanism<sup>74</sup>. Moreover, postnatal long bone growth occurs at the growth plates—the sites most commonly studied in angiogenic-osteogenic coupling studies<sup>75</sup>. By contrast, cranial bones—which do not have growth plates—grow at the

osteogenic fronts adjacent to the sutures, and it is unclear whether blood vessels play a role in this process<sup>35</sup>. Provided these differences, it cannot be assumed that the angiogenic-osteogenic coupling mechanisms observed in long bone are the same as those in cranial bone.

Some studies have suggested that there is an intimate relationship between blood vessels and osteoprogenitors/osteoblasts in cranial bone. For instance, studies using intravital imaging demonstrated that osteoblasts reside within close proximity (<10  $\mu\text{m}$ ) to blood vessels within the bone marrow cavities and that vessels deep within the marrow space exhibit less blood flow and oxygen tension than those near the endosteum—the site where active bone remodeling occurs<sup>9–11</sup>. Additionally, studies employing a calvarial defect injury model showed that blood vessels are spatially correlated with infiltrating osteoprogenitors and potentially serve as a template for newly forming bone<sup>76,77</sup>. The presence of CD31<sup>hi</sup>Emcn<sup>hi</sup> vessels has also been documented in the calvarium, but it is unclear whether these blood vessels serve a similar function as in long bone<sup>50</sup>. Furthermore, the global distribution of different types of blood vessels in the calvarium remains poorly understood, as these studies all focused on small regions of interest.

In addition, several studies have reported differences in the angiogenic-osteogenic coupling mechanisms of cranial and long bone. Wang *et al.* (2007)<sup>48</sup> found that stimulating HIF-1 $\alpha$  expression in osteoblasts had no effect on cranial bone volume or osteoblast number, even though it significantly enhanced angiogenesis and osteogenesis in long bone. Other studies have also demonstrated differences in the timing and type of angiogenic genes upregulated during endochondral ossification of the limbs versus intramembranous ossification of the skull<sup>78,79</sup>. In experiments described by Wan *et al.* (2010)<sup>78</sup>, conditionally knocking down HIF-1 $\alpha$  in mesenchymal cells via the dermo-1 promoter resulted in a significant loss of mineralization in the parietal bone and an increase in suture width, while targeting HIF-1 $\alpha$  in Osteocalcin+ osteoblasts had no effect. These data suggest that HIF-1 $\alpha$  expression is important for cranial bone development, but the timing of expression by skeletal progenitor cells may be different

in cranial versus long bone. Another study done by De Spiegelaere *et al.* (2010)<sup>79</sup> showed that only Hif2 $\alpha$  protein was expressed by osteoblasts in mandibular bone (develops through intramembranous ossification) during porcine embryonic development, while both HIF-1 $\alpha$  and Hif2 $\alpha$  was expressed by osteoblasts and periosteal progenitors in the long bones. Despite these differences, VEGF was highly expressed in both bone types, suggesting that differential pathways could be responsible for angiogenesis and osteogenesis in skull bone versus long bone<sup>79</sup>. Taken together, the findings from these studies demonstrate the necessity to study the mechanisms of angiogenic-osteogenic coupling in cranial bone separately from long bone.

### **1.3 3D Bone Imaging Technologies**

Provided that vascular abnormalities have been linked to conditions such as craniosynostosis<sup>6,8</sup>, cleft palate<sup>5</sup>, and mandibular hypoplasia<sup>3</sup>, it is essential for the field to develop a better understanding of how angiogenesis and osteogenesis are coupled during skull bone development, remodeling, and healing. One of the key challenges to studying this process is the lack of imaging technologies to evaluate the relationship of blood vessels and osteoprogenitors in irregularly shaped bones such as the skull. In this section, I review the 3D imaging technologies that have been used to image bone and reflect on their limitations with respect to cranial bone.

#### **1.3.1 3D Tissue Sectioning and Immunohistochemistry**

Tissue sectioning and immunohistochemistry has been one of the most common techniques to observe tissue structure and composition in bone. This technique involves sectioning thin sections of bone (usually 10  $\mu\text{m}$  or less), staining it with antibodies specific to cellular or ECM proteins of interest, and imaging the sections using brightfield or fluorescence microscopy. While most studies before the 2010s used this technique to study bone vasculature and osteoprogenitors/osteoblasts, tissue

sectioning has significant drawbacks in that it only provides a fraction of the tissue volume, cannot be used to observe 3D cellular structures such as blood vessels, and can distort the tissue morphology<sup>52,80</sup>.

Recent studies have overcome these challenges by developing protocols to image thick tissue sections (>100  $\mu\text{m}$ ). In Kusumbe *et al.* (2015)<sup>52</sup>, they optimized different steps of traditional histology protocols to enable sectioning of long bone into 100  $\mu\text{m}$  slices while preserving tissue morphology. Using this protocol, they were capable of imaging numerous cell types and structures including the vasculature, osteoprogenitors, hematopoietic cells, and bone extracellular matrix<sup>52</sup>. This technological advancement enabled the discovery of specific blood vessel subtypes in long bone and their relationships to osteogenesis and hematopoiesis<sup>50,75,81</sup>.

While these sectioning methods yielded high quality 3D images of cellular structures in long bone, they were generally limited to imaging  $\sim$ 100-200  $\mu\text{m}$  thick sections due to light scattering that occurred deeper into the tissue. Recent protocol developments have overcome these issues by combining optical clearing techniques with tissue sectioning and immunostaining. Acar *et al.* (2015)<sup>82</sup> adapted the 3DISCO and Murray's clear methods to optically clear bisected long bones and image hematopoietic stem cells in the bone marrow. Using this method, they discovered that hematopoietic stem cells—labeled using a  $\alpha$ -catulin-GFP reporter and cKit antibody stain—made up only 0.02% of hematopoietic cells and predominantly resided nearby bone marrow sinusoidal vessels rather than by arterioles or bone surfaces<sup>82</sup>. In another pair of studies conducted by Coutu *et al.* in 2017 and 2018, they developed a tissue clearing method using 2,2-thiodiethanol to allow imaging of up to eight markers simultaneously in >200  $\mu\text{m}$ -thick bone sections<sup>80,83</sup>. They used this method to generate comprehensive 3D maps of non-hematopoietic cell types and extracellular matrix proteins in long bones, enabling an unprecedented analysis of the 3D cellular niches in the bone marrow and the discovery of rare cellular phenotypes that had not been previously identified from other methods<sup>83</sup>.

### 1.3.2 Intravital Microscopy

Intravital microscopy is a method that enables live 3D imaging of different cell types and matrix proteins in cranial bone, such as blood vessels, bone and immune cells, and collagen ECM. This technique involves the creation of an optical window in the parietal or frontal bones to allow for live imaging of cellular structures using modalities such as confocal or 2-photon microscopy, second harmonic generation microscopy, fluorescence life-time imaging microscopy, intrinsic optical signal imaging, and laser speckle contrast imaging<sup>77,84,85</sup>. Compared to traditional tissue sectioning and immunostaining techniques, intravital microscopy has significant advantages, as it enables imaging of intact tissues (up to ~200  $\mu\text{m}$  depth), provides high resolution (<10  $\mu\text{m}$ ), and allows for short-term (second to minutes) and long-term (days to weeks) tracking of cell populations within the same animal<sup>86</sup>.

Using intravital microscopy, studies have been able to provide some characterization of the cranial microvasculature and its relationship to osteoprogenitors and osteoblasts. In Lo Celso *et al.* (2009)<sup>9</sup>, the first major study to perform intravital microscopy on the skull, it was shown that the majority of osteoblasts reside in close proximity (<10  $\mu\text{m}$ ) to vessels within marrow cavities. Subsequent studies using this technique also demonstrated blood vessels near the endosteum (where osteoblasts reside) have higher blood flow and oxygen tension and a lower diameter compared to vessels deep within the marrow space<sup>10,11</sup>. However, it was unclear whether any of these vessels resembled the Type H vessel phenotype observed in long bone.

Several reports have also used intravital microscopy to visualize and quantify blood vessels, osteoprogenitors, and collagen deposition during native healing<sup>77,84,87,88</sup>. In Huang *et al.* (2015)<sup>77</sup>, they used intravital microscopy to track the infiltration of blood vessels and Col1+ osteoblasts following an acute 1-mm parietal bone defect injury. They found that most angiogenesis and osteoblast infiltration occurred within the first three weeks following injury and showed that osteoblasts were spatially

associated with the vasculature during the healing process<sup>77</sup>. Other studies have also shown that skeletal stem cells rapidly infiltrate into the defect within the first 1-2 weeks following injury, along with the vasculature<sup>76,89</sup>. These observations afforded by intravital microscopy implicate a link between blood vessels and osteoprogenitors/osteoblasts during healing; although, it remains unknown whether specific types of vessels interact with bone-forming cells during this process.

### **1.3.3 Tissue Clearing and Light Sheet Microscopy**

Tissue clearing and light-sheet microscopy are a paired set of techniques that have recently emerged to enable high resolution imaging of intact 3D organs. Optical tissue clearing involves a series of steps such as decolorization, delipidation, and refractive index matching to make large tissue specimens (cm<sup>3</sup>) transparent for imaging<sup>90</sup>. Light-sheet fluorescence microscopy is a technique where the focal plane of a cleared sample is selectively illuminated using a thin sheet of light (<10 μm) that is perpendicular to the direction of observation<sup>91</sup>. This configuration enables rapid acquisition of 3D images by capturing optical slices at pre-defined intervals using a high-resolution camera<sup>91</sup>. Light-sheet fluorescence microscopy is particularly advantageous for imaging large specimens because it minimizes photobleaching and can acquire single-cell resolution images of cm<sup>3</sup>-sized tissues in a timeframe of hours rather than days<sup>92</sup>.

While tissue clearing and light-sheet microscopy has been most widely used in neuroscience research, some studies have developed methods to image whole long bone tissues. Greenbaum *et al.* (2017)<sup>12</sup> was the first major study to develop a clearing and light-sheet microscopy protocol, called Bone CLARITY, to image long bone specimens at single-cell resolution. Their analysis enabled the visualization and quantification of Sox9+ skeletal progenitor cells in the mouse femur and tibia, and provided a more accurate analysis of cell quantification compared to traditional serial sectioning techniques<sup>12</sup>. Another study by Grüneboom *et al.* (2019)<sup>28</sup> adapted the simpleCLEAR protocol to visualize blood vessels in long

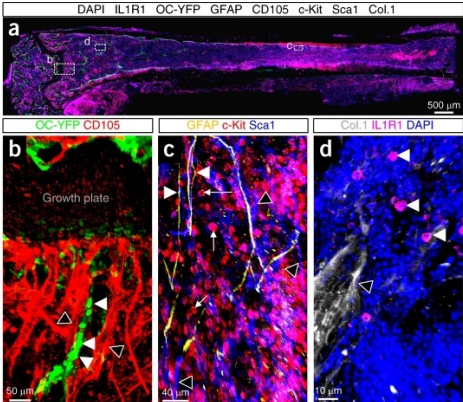
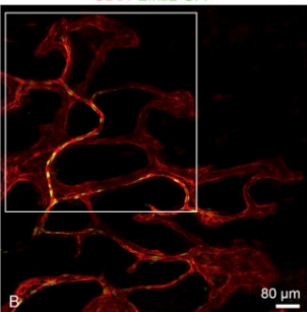
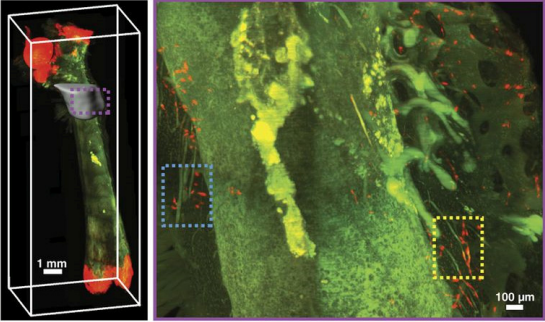
bone. This technique enabled the discovery a specific type of blood vessel—called transcortical vessel—that connected the periosteal to bone marrow vasculature and was responsible for 60-80% of the blood flow in and out of the bone<sup>28</sup>. The novel findings from these studies demonstrate the potential of tissue clearing and light-sheet microscopy to accelerate discovery and develop a more complete understanding of angiogenic-osteogenic coupling in cranial bone.

#### **1.3.4 Limitations in 3D Bone Imaging Technologies**

While each of these imaging technologies has facilitated significant advancement in bone biology, their limitations make them less suitable for studying the relationship of blood vessels and bone-forming cells in cranial bone (**Table 1.1**). Unlike long bone, which can be readily sectioned and imaged along its long axis, cranial bone is irregularly shaped and cannot be sectioned in a suitable orientation for visualizing the 3D microvasculature. Intravital microscopy has allowed for some in-depth characterization of blood vessels in the cranial bone marrow, but it is limited to a mm<sup>2</sup> field of view and does not provide a global analysis of the cranial microvasculature and its relationship to osteoprogenitors/osteoblasts<sup>11,76</sup> (viewing the entire calvarium is particularly important since it contains bones and sutures from different developmental origins). Tissue clearing and light-sheet microscopy have the potential to visualize multiple cellular structures throughout the calvarium, but current technologies are limited to using endogenous fluorescence or 1-2 antibody labels simultaneously<sup>12,13,28</sup>. Moreover, there are no readily accessible quantitative pipelines that enable the spatial analysis of cellular structures such as blood vessels and osteoprogenitors in large 3D light-sheet datasets (>100 GB per image). Light-sheet imaging methods that allow for the visualization and quantification of multiple

cellular markers should be developed the allow for comprehensive analyses of the cranial microvascular environment.

**Table 1.1: Methods for imaging the bone microvascular environment in 3D.** Representative images for each method are adapted from Coutu *et al.*, Bixel *et al.*, and Greenbaum *et al.* (Refs. 80, 11, and 12). Advantages and limitations are provided for each method.

Methods	Advantages	Limitations
 <p><b>3D Tissue Sectioning and Immunohistochemistry</b><sup>80</sup></p>	<ul style="list-style-type: none"> <li>• Uses common sectioning and staining protocols that are easy to adapt</li> <li>• Allows for multiplexing (up to 8 cellular markers)</li> <li>• Can provide subcellular resolution</li> </ul>	<ul style="list-style-type: none"> <li>• Difficult to perform on curved or irregularly shaped bones</li> <li>• Does not display the entire tissue structure</li> <li>• Imaging process may be time-intensive and cause photobleaching</li> </ul>
 <p><b>Intravital Microscopy</b><sup>11</sup></p>	<ul style="list-style-type: none"> <li>• Enables live and longitudinal imaging</li> <li>• Can be used to measure physiological parameters</li> <li>• Can provide subcellular resolution</li> </ul>	<ul style="list-style-type: none"> <li>• Difficult and time-intensive to perform</li> <li>• Provides small field of view</li> <li>• Generally limited to 1-2 cellular markers</li> </ul>
 <p><b>Tissue Clearing and Light-sheet Microscopy</b><sup>12</sup></p>	<ul style="list-style-type: none"> <li>• Can be used to image whole tissue structures, such as the skull</li> <li>• Enables rapid imaging at single-cell resolution</li> <li>• Minimizes photobleaching</li> </ul>	<ul style="list-style-type: none"> <li>• Difficult to visualize subcellular details</li> <li>• Most common protocols are limited to 1-2 cellular markers</li> <li>• Large file sizes make it difficult to process and analyze images</li> </ul>



# Chapter 2 : Development of a Quantitative Light-sheet Microscopy (QLSM) Platform to Generate 3D Maps of the Cranial Microvascular Environment

## 2.1 Introduction

Vascularization is essential for the development, growth, and maintenance of cranial bone. During development, vessels provide a template for mineralization during intramembranous and endochondral ossification<sup>2</sup>, and vascular abnormalities have been linked to syndromes in the skull such as mandibular hypoplasia<sup>3</sup>, hemifacial microsomia<sup>4</sup>, cleft palate<sup>5</sup>, and craniosynostosis<sup>6</sup>. Furthermore, a specific class of blood vessel high in CD31 and *Emcn* expression is known to be spatially coupled with osteoprogenitors and is critical for long bone development, postnatal growth, and remodeling<sup>50,55,93</sup>. However, there remains a significant knowledge gap in the relationship between the different types of blood vessels and skeletal progenitors in cranial bone.

The distribution of craniofacial vessel subtypes and their spatial relationship to skeletal progenitors remains poorly understood due to a lack of adequate imaging technologies. Methods used in long bone allow for imaging of thick sections (>100  $\mu\text{m}$ ) to visualize the microvasculature in 3D<sup>52,80</sup>, but these techniques are difficult to adapt to craniofacial bone due to its irregular, curved geometry. Intravital microscopy is an alternative method that has been applied to study calvarial blood vessels, but it is limited to imaging small regions ( $\text{mm}^2$ ) and cannot provide a global analysis of the cranial microvasculature and skeletal progenitor cells<sup>11</sup>. Recent developments in optical tissue clearing and

light-sheet microscopy are a promising avenue for characterizing the microvascular environment of large, irregularly-shaped tissues such as the skull. However, current approaches are limited to using endogenous fluorescence for labeling cellular structures and would not be capable of visualizing different blood vessel and cell types simultaneously<sup>12,13</sup>. Additionally, there remains a lack of quantitative methods to assess the 3D spatial relationships of cellular structures in large light-sheet imaging datasets (>100 GB). These shortcomings limit the application of the otherwise powerful capabilities of tissue clearing and light-sheet imaging for studying the skull.

In this Chapter, I present a quantitative 3D light-sheet microscopy (QLSM) platform that overcomes the challenges of existing techniques to provide a comprehensive analysis of the cranial bone microvasculature. This method enables quantitative characterization of blood vessels and bone cells in the murine calvarium by combining whole-mount immunostaining, optical tissue clearing, light-sheet microscopy, and advanced 3D image analysis. Using this platform, I provide single-cell resolution 3D maps of vessel subtypes and skeletal progenitors in the frontoparietal bones of the calvaria from 4-week-old mice. These novel datasets provide fundamental insight into the spatial distribution of blood vessels and their interactions with skeletal progenitors in the calvarium.

## **2.2 Methods**

### **2.2.1 Materials**

All essential antibodies, reagents, animal drugs and materials, instruments and hardware, and software used in this chapter are provided in **Appendix I**.

### **2.2.2 Study Approval**

All animal experiments were approved by the Johns Hopkins University Institutional Animal Care and Use Committee (Protocol No. MO18M188). Animals were housed and cared for in Johns Hopkins' Research Animal Resources central housing facilities.

### **2.2.3 Experimental Animals**

We used 4-week-old male C56BL/6J mice from Jackson Laboratories (Stock No. 000664) for all experiments in this chapter.

### **2.2.4 Murine Calvarial Harvest**

To harvest calvaria, we perfused the vasculature with heparinized saline (10 U/mL in 1X PBS) to remove the blood in calvarial bone prior to fixation. Mice were heavily anesthetized with ketamine (100 mg/kg) and xylazine (20 mg/kg) and subcutaneously injected with 200 U heparin to prevent premature clotting. An initial incision was made near the xiphoid process, and the chest was then cut open along the lateral edges of the rib cage to provide access to the heart. Heparinized saline was perfused into the left ventricle via a blunt 20G needle at a rate of 10 mL/min. The right atrium was opened just prior to perfusion to enable open circulation. Following perfusion, calvaria were harvested—taking special care to preserve the periosteum and dura mater—and were fixed in 4% methanol-free paraformaldehyde overnight at 4°C. Fixed calvaria were washed with PBS three times prior to staining.

### **2.2.5 Whole Mount Immunostaining and Optical Clearing**

To enable 3D light-sheet imaging of calvaria, we performed whole mount immunostaining to label blood vessel phenotypes and skeletal progenitors and optically cleared the calvaria following staining. First, samples were blocked overnight at 4°C using a solution comprised of 10% V/V normal donkey serum in wash buffer (0.1M Tris, 0.15M NaCl, 0.05% V/V Tween-20, 20% V/V dimethylsulfoxide, pH 7.5), and then using a biotin blocking kit for 8h at room temperature to mask endogenous biotin.

Samples were stained with primary antibodies for CD31, Emcn, and Osterix or Gli1 for 7 days, fluorophore- and biotin-conjugated secondary antibodies for 7 days, and a streptavidin conjugate for 5 days to enable signal amplification of Emcn. All antibodies and conjugates were diluted in the same buffer used for blocking. Calvaria were washed five times over a 24h period between antibody and streptavidin incubation steps. Following staining, samples were cleared using a graded series of 2,2-thiodiethanol (TDE in TBS-Tween; 25%, 50%, 75%, 90%, 100% x 2). Each clearing step was performed for 2h at room temperature or overnight at 4°C. Calvaria were stored in 100% TDE at 4°C prior to imaging.

### **2.2.6 Light-sheet Imaging**

We imaged calvaria using a custom light-sheet imaging protocol that enabled us to achieve adequate signal intensity and quality throughout the entire volume. Calvaria were mounted and immersed into a glass imaging chamber containing 100% TDE. The chamber was loaded into a LaVision Biotec Ultramicroscope II that was pre-aligned to match the refractive index of TDE. Whole calvarial samples were imaged using three separate acquisitions: 1) a 3 x 1 tile using both double sided illumination at the center of the sample, 2) a 3 x 2 tile using left-sided illumination at the left portion of the sample, and 3) a 3 x 2 tile using right-sided illumination at the right portion of the sample. Tiles were overlapped by 15% within each acquisition and 30-35% along the x-axis between different acquisitions to facilitate stitching. The following hardware and settings were used for all scans: 2.5X zoom with a 2X dipping cap (5X magnification, 1.3  $\mu\text{m}$  x-y pixel size), 5.5 Megapixel sCMOS camera, 20 ms exposure time, 0.154 numerical aperture, and 2.5  $\mu\text{m}$  z step size. Based upon the assumption that the light-sheet followed a Gaussian beam profile, the estimated light-sheet width was 2.3-3.2  $\mu\text{m}$  at the center of each tile and 284.2  $\mu\text{m}$  at the horizontal edges of each tile for all scans<sup>94,95</sup>. Different channels were imaged using 561, 640, and 785 nm lasers and 590/33, 620/60, and 845/55 filters, respectively. Laser powers were optimized for each antibody and held constant between scans.

## 2.2.7 Image Processing and Analysis

We performed all image processing and analysis using Imaris 9.5 software and a Dell Precision 7820 Tower workstation. The workstation was equipped with a Dual Intel Xeon Gold 6240 processor, 384 GB DDR4 SDRAM (2666 MHz speed), 512 GB and 1 TB SATA SSDs, NVIDIA Quadro RTX5000 graphics card (16 GB GDDR6 memory), and Windows 10 Pro for Workstations. All data was stored and analyzed using Samsung T5 2TB External SSDs connected via USB 3.2 or USB 3.2 Type-C ports.

To pre-process the images for analysis, we converted LaVision Biotec raw .ome.tif files to the Imaris file format (.ims) for each individual tile using Imaris File Converter 9.5. Tiles were manually aligned along the x-y axes and stitched into one 3D image using Imaris Stitcher 9.5.

Following image pre-processing, we implemented a custom analysis pipeline in Imaris 9.5 to enable us to characterize vessel phenotypes and skeletal progenitors. First, a pre-defined VOI containing six distinct rectangular regions was positioned for each dataset, with the VOI dimensions remaining constant across all datasets. The sagittal and interfrontal sutures were avoided due to their lower signal quality. Following VOI specification, CD31<sup>hi</sup> and Emcn<sup>hi</sup> vessels were segmented using the Surfaces module with a 10  $\mu\text{m}$  radius for background subtraction and  $10^4 \mu\text{m}^3$  volume filter to eliminate subcellular-sized segments. Osterix+ and Gli1+ cells were segmented using the Spots module using a pre-measured spot size in the axial and lateral dimensions (5  $\mu\text{m}$  lateral, 15  $\mu\text{m}$  axial for Gli1+ cells; 6  $\mu\text{m}$  lateral, 18  $\mu\text{m}$  axial for Osterix+ cells). Thresholds were optimized for each experimental group to minimize background in the segmented objects. Following this initial segmentation, images were down-sampled by a factor of two in each dimension to facilitate a second round of segmentation for vessel phenotypes. In the down-sampled datasets, binary masks for C31- and Emcn-segmented vessels were created and re-segmented using the “Split Objects” Surfaces function (10  $\mu\text{m}$  seeding point diameter). CD31<sup>hi</sup>Emcn<sup>-</sup> and CD31<sup>hi</sup>Emcn<sup>hi</sup> vessels were segmented using the CD31 mask and filtered based upon the absence or presence of masked Emcn signal within each object, respectively. CD31<sup>lo</sup>Emcn<sup>hi</sup> vessels

were segmented based upon the Emcn mask and filtered to remove objects co-localized with masked CD31 signal. During all segmentation steps, “shortest distance calculation” was activated to enable measurements of individual cells to their nearest vessel. Cells touching their nearest vessel were designated as 0  $\mu\text{m}$  away from the vessel.

Once all image segmentation was complete, we exported Surface and Spots statistics for vessel phenotypes and skeletal progenitors, respectively, to enable data analysis in third party software. XiT software<sup>80</sup> was used to plot the spatial distance of individual Osterix+ or Gli1+ cells relative to each vessel phenotype in 3D. GraphPad Prism and Microsoft Excel were used to plot and analyze vessel volume, cell number, and vessel-cell distance measurements.

## **2.2.8 Statistics**

We used GraphPad Prism 5 software to perform all statistical analyses. All measurements were performed on distinct samples for each type of analysis. Statistical comparisons were performed using a two-tailed t-test, one-way ANOVA with Tukey’s post-hoc test, or two-way ANOVA with Bonferroni’s post-hoc test. Statistical tests performed and sample sizes for each dataset is designated in the figure captions. All p-values less than 0.05 were considered statistically significant.

## **2.3 Results**

### **2.3.1 3D Quantitative Light-sheet Imaging of Murine Calvaria**

To visualize vessel phenotypes and skeletal progenitors in the murine calvarium, we developed and optimized an imaging pipeline comprised of whole-mount immunostaining, optical tissue clearing, and light-sheet imaging (**Figure 2.1A**). We adapted a staining regimen used in long-bone sections<sup>80</sup> to achieve adequate antibody penetration and labeling of up to three molecular markers: CD31 and Emcn for vessels and Osterix or Gli1 for skeletal progenitor subpopulations. Osterix is a marker for skeletal

progenitors that are restricted to the osteoblast lineage<sup>50</sup>, while Gli1 marks less-differentiated skeletal stem cells<sup>33,96</sup>. To achieve high-quality visualization of each marker, we used fluorophores spanning the red to infrared spectrum, as ultraviolet and green dyes resulted in high levels of background and light scattering during imaging. We cleared the calvaria by removing the blood prior to staining and incubating in a graded series of 2,2-thiodiethanol (TDE) following staining. This method did not require us to decalcify bone to achieve adequate bone tissue clearing and maintained the geometry of the calvarium (**Figure 2.1B-C**). Following clearing, we imaged calvaria using light-sheet microscopy, which allowed us to rapidly acquire high-resolution data and minimize photo-bleaching through the duration of the scan (~5 hr per sample). Our resulting images captured the 3D distribution of different vessel phenotypes and skeletal progenitors in the calvarium with high axial and lateral resolution (**Figure 2.2A-D**).

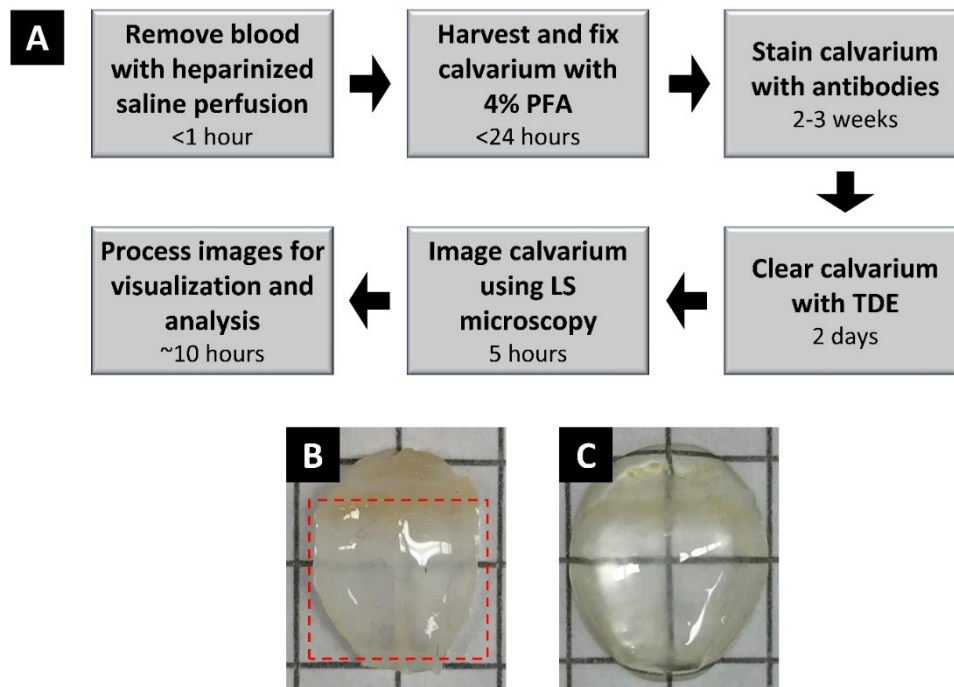


**Figure 2.1: Quantitative 3D light-sheet imaging pipeline.** **A** Diagram displaying the steps to harvest, stain, clear, and image calvaria for data analysis. The entire procedure—including quantitative analysis—takes 3-4 weeks to complete. **B** Non-decalcified calvarium before optical clearing. The dotted red lines indicate the region of the calvarium that was imaged. **C** Non-decalcified calvarium following clearing with TDE.

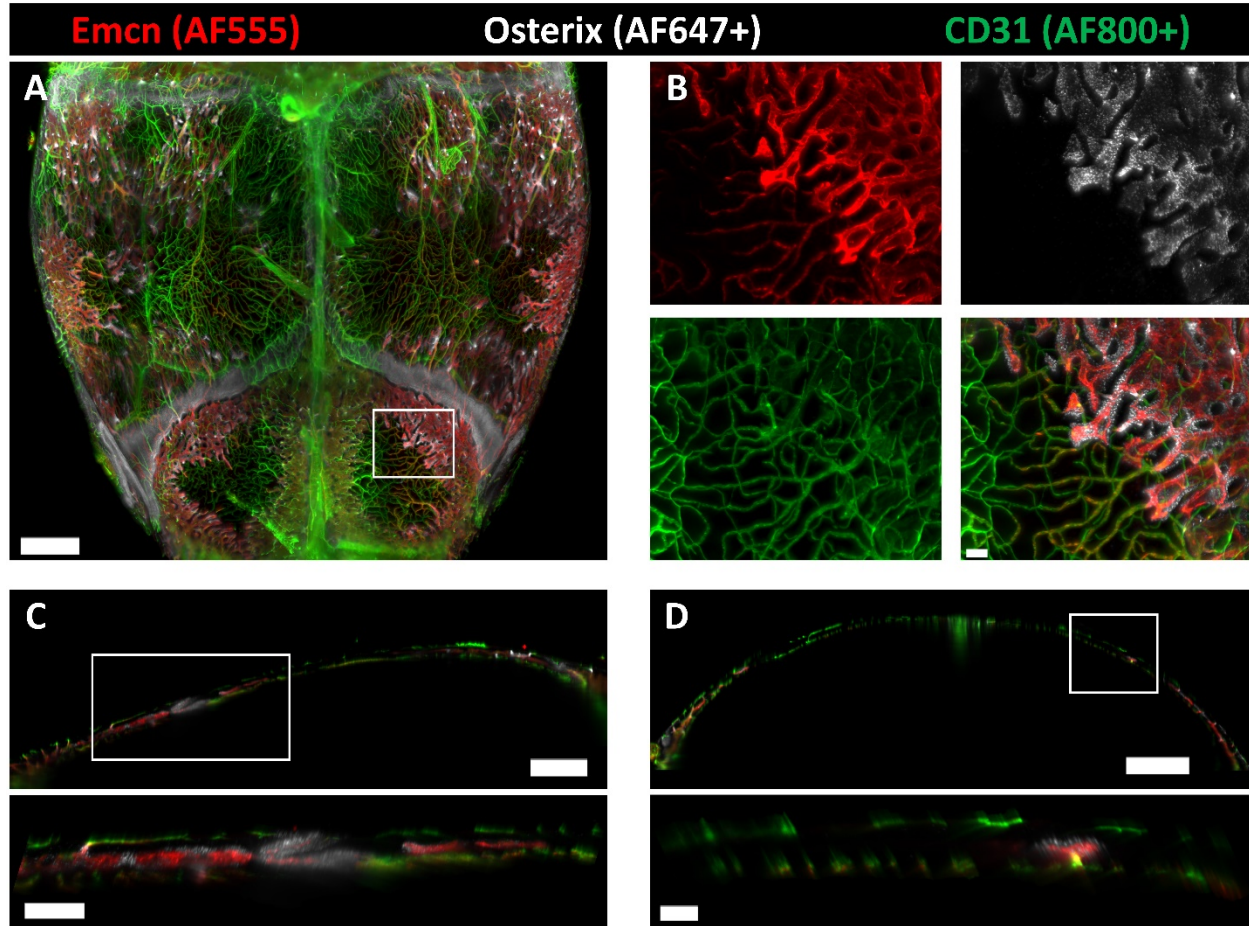


**Figure 2.2: 3D light-sheet imaging of the murine calvarium at single-cell resolution.** **A** Maximum intensity projection (MIP) of vessels and Osterix+ skeletal progenitors in the parietal and posterior frontal bones of the calvarium. **B** Images from the boxed region in **A** demonstrating the high resolution and signal quality obtained in each channel (i–iv). The dyes used for each channel are designated above (**A**) and (**B**): AF555 for Endomucin (i), AF647 plus for Osterix (ii), and AF800 plus for CD31 (iii). **C, D** Sagittal (**C**) and frontal (**D**) 40- $\mu$ m-thick optical sections demonstrating the location of vessels and Osterix+ cells along the thickness of the calvarium. Boxed regions from (**C**i) and (**D**i) are shown in **C**ii and **D**ii. Similar results were achieved for all the calvaria imaged in this study ( $n = 45$  calvaria). Scale bars: 1000  $\mu$ m (**A, D**i), 800  $\mu$ m (**C**i), 300  $\mu$ m (**C**ii), 100  $\mu$ m (**B**i–iv, **D**ii). Colors: Red: Endomucin (Emcn), Gray: Osterix, Green: CD31.

To analyze vessel phenotypes and skeletal progenitors, we developed a quantitative pipeline to enable 3D spatial characterization of high-resolution datasets (~500 GB raw, ~200 GB compressed, **Figure 2.3A**). We applied the spots and surfaces modules in Imaris software to segment blood vessels and skeletal progenitors, and then performed a series of masking and filtering algorithms to denote three vessel phenotypes: CD31<sup>hi</sup>Emcn<sup>-</sup> arteries and arterioles, CD31<sup>hi</sup>Emcn<sup>hi</sup> capillaries, and CD31<sup>lo</sup>Emcn<sup>hi</sup> capillaries and sinusoids<sup>81,83</sup> (**Figure 2.3B-D**). CD31<sup>lo</sup>Emcn<sup>lo</sup> sinusoids were not segmented due to their



low signal-to-noise ratio. We exported the spots and surfaces statistics into GraphPad Prism and XiT software<sup>80</sup> to analyze vessel volume, skeletal progenitor number, and vessel-skeletal progenitor spatial distances (**Figure 2.3E**). The resulting analysis provides a comprehensive characterization of the spatial coupling between vessels and skeletal progenitors by reflecting the native 3D environment across large tissue volumes (cm<sup>3</sup>).

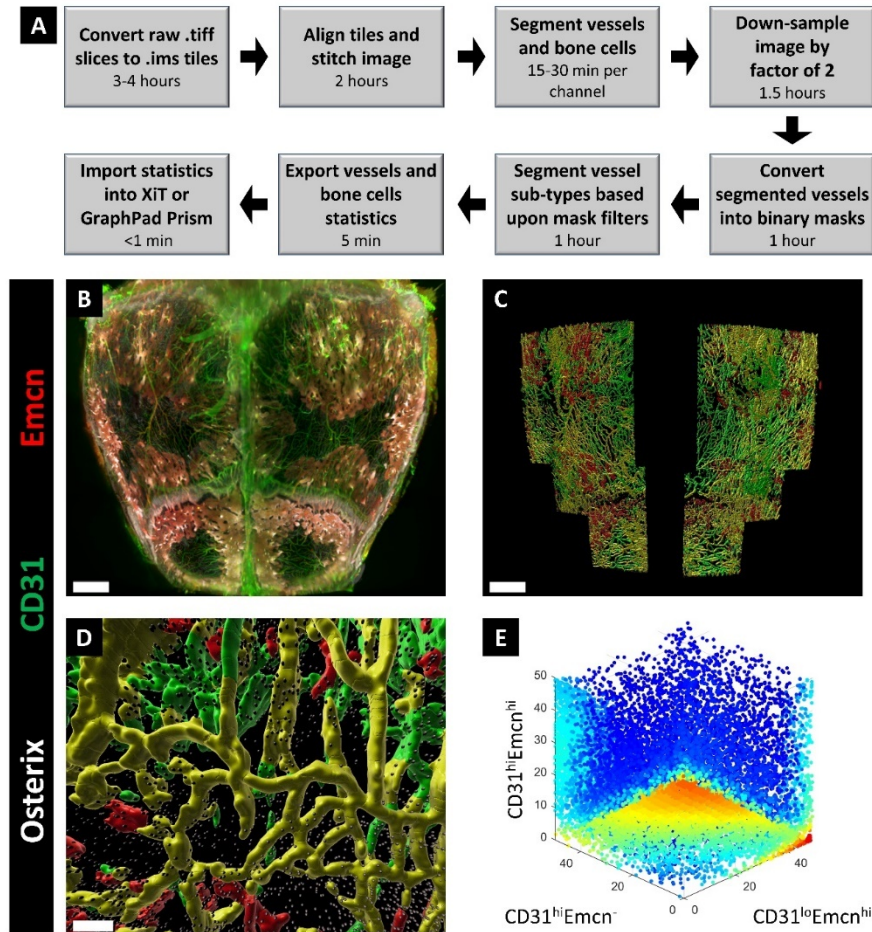


**Figure 2.3: Quantitative analysis pipeline for characterizing calvarial blood vessel phenotype and skeletal progenitor distribution in 3D.** **A** Diagram displaying the steps performed to analyze each dataset. The entire pipeline takes approximately 10 hours to complete using a high-performance workstation. **B** 3D projection of a calvarium stained for CD31, Emcn, and Osterix. **C** 3D segmentation of calvarial vessel phenotypes and Osterix+ cells in the volume of interest (sagittal suture not included due to the interference of signal from the sagittal sinus). **D** Zoomed-in portion of (C) displaying the spatial relationships of Osterix+ cells to each vessel phenotype. Segmented colors represent the following: CD31<sup>hi</sup>Emcn<sup>-</sup> vessels (green), CD31<sup>hi</sup>Emcn<sup>hi</sup> vessels (yellow), CD31<sup>lo</sup>Emcn<sup>hi</sup> vessels (red), Osterix+ cells (gray). Segmentation results are representative of the 32 whole calvaria imaged and analyzed in this study (different regions of interest were used to analyze the 12 calvaria with subcritical-sized defects). **E** 3D plot representing the distance of individual Osterix+ cells to each vessel phenotype from (C). Dot color represents the density of cells relative to their position in the plot (red=high density, blue=low density). Scale bars: 1000  $\mu$ m (B,C); 200  $\mu$ m (D). Colors (B-D): Red: Endomucin (Emcn), Gray: Osterix, Green: CD31

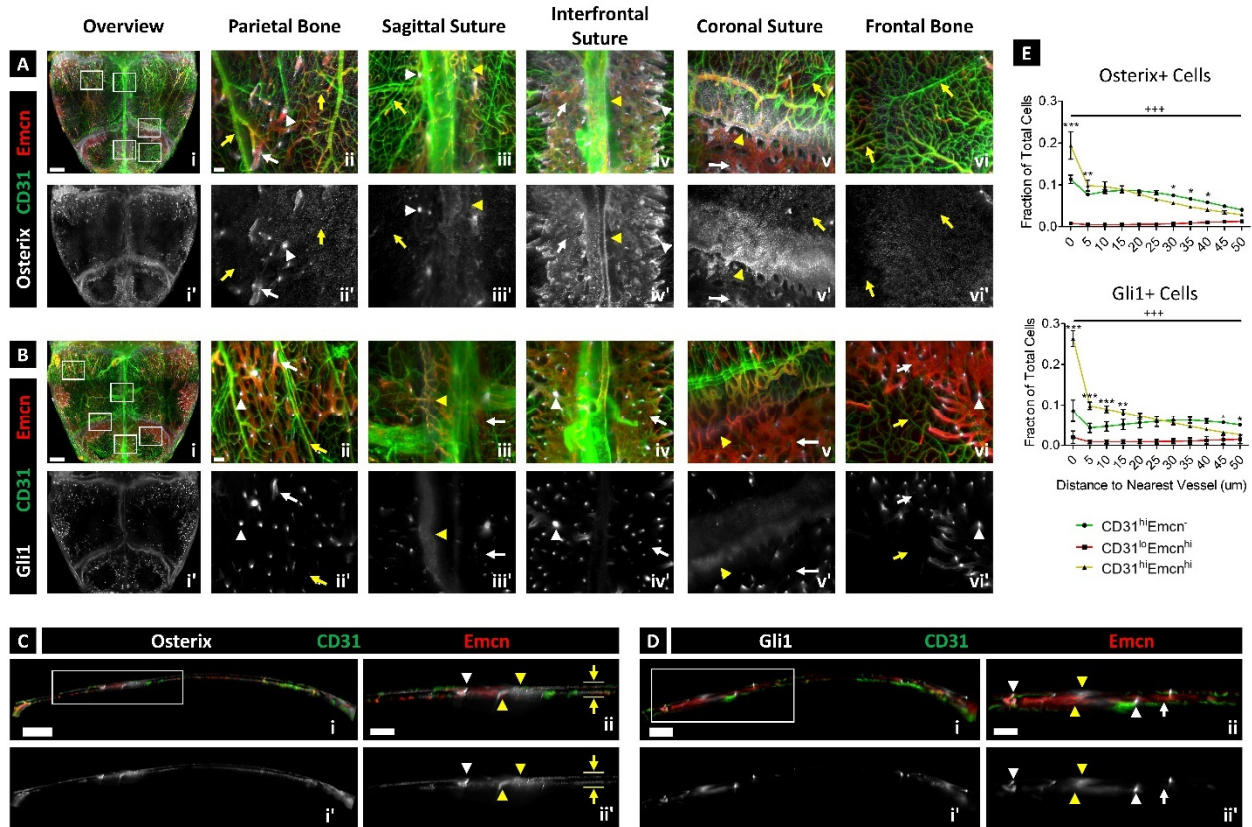
### 2.3.2 3D Map of Calvarial Vessels and Skeletal Progenitors

Using our imaging pipeline, we generated high-resolution 3D maps of vessel phenotypes, Osterix+ skeletal progenitors, and Gli1+ skeletal progenitors in the parietal and posterior frontal bones of juvenile 4-week-old mice. Vessels were located in the periosteum, dura mater, transcortical canals, marrow cavities, and osteogenic fronts adjacent to the sutures (**Figure 2.4A-D**). Marrow vessels in the parietal and frontal bones were observed near the sutures, while only periosteal and meningeal vessels were observed at the center of each bone. Vessel phenotypes were also differentially distributed in the calvarium: Most CD31<sup>hi</sup>Emcn<sup>-</sup> arteries and arterioles were present in the periosteum and dura mater, while CD31<sup>lo</sup>Emcn<sup>hi/lo</sup> sinusoids were restricted to the marrow cavities. CD31<sup>hi</sup>Emcn<sup>hi</sup> capillaries were present in the periosteum, dura mater, marrow cavities, and osteogenic fronts, connecting CD31<sup>hi</sup>Emcn<sup>-</sup> periosteal arterioles to CD31<sup>lo</sup>Emcn<sup>hi</sup> sinusoids. Expression of CD31 and Emcn in CD31<sup>hi</sup>Emcn<sup>hi</sup> capillaries was most intense at the transcortical canals—the regions that enable arterioles in the periosteum and dura mater to connect to venous sinusoids.

Similar to vessel phenotypes, skeletal progenitors varied in their spatial distribution. Osterix+ osteoprogenitors were prevalent in the periosteum and dura mater, osteogenic fronts nearby sutures, transcortical canals, and marrow cavities of the parietal and frontal bones (**Figure 2.4A, C**). Gli1+ progenitors—a marker for less-differentiated skeletal stem cells<sup>33,96</sup>—were concentrated at the sutures, transcortical canals, and marrow cavities adjacent to transcortical canals, but they were mostly absent from the periosteum and dura mater (**Figure 2.4B, D**). Interestingly, expression of Gli1 was visibly more intense at the transcortical canals compared to the sutures.

To determine whether skeletal progenitors exhibited a preferential spatial relationship to specific vessel phenotypes, we quantified the distribution of Osterix+ and Gli1+ progenitors relative to each vessel type. We found that both progenitor populations were preferentially associated with CD31<sup>hi</sup>Emcn<sup>hi</sup> vessels compared to other vessel phenotypes (**Figure 2.4E**). This relationship was most

apparent at the transcortical canals, where we observed the highest protein expression of CD31 and Emcn in vessels and Osterix or Gli1 in skeletal progenitors.



## 2.4 Conclusion

In this Chapter, I developed a quantitative 3D light-sheet imaging platform to study the cranial microvascular environment. I optimized a combination of techniques, including whole-mount immunostaining, optical tissue clearing, light-sheet microscopy, and 3D image analysis, to visualize and quantify cellular structures throughout the murine calvarium. Using this method, I generated 3D maps of the different types of blood vessels and skeletal progenitors in the calvaria of juvenile (4-week-old) mice. Through visualizing and quantifying these data, I found that CD31<sup>hi</sup>Emcn<sup>hi</sup> capillaries were spatially correlated with Osterix+ osteoprogenitors and Gli1+ skeletal stem cells—particularly at and nearby the transcortical canals. These data provide an initial framework for how blood vessels and skeletal progenitors interact during postnatal cranial bone growth.

# Chapter 3 : Changes to the Cranial Microvascular Environment During Postnatal Cranial Bone Growth and Remodeling

## 3.1 Introduction

Blood vessels are essential for bone maintenance and remodeling. In humans, vascular dysfunction or abnormalities have been linked to conditions such as osteoporosis and fracture non-unions<sup>71,97</sup>. Additionally, studies done in mice have shown that age-related changes to the bone microvasculature results in a reduction in bone mineral density, and that CD31<sup>hi</sup>Emcn<sup>hi</sup> vessels are important for stimulating osteogenesis during bone remodeling<sup>50,55</sup>. However, it is not known how the cranial microvasculature changes with age and different levels of bone remodeling activity.

In this Chapter, I study how the cranial microvasculature and its relationship to skeletal progenitor cells changes following postnatal growth and after perturbations to remodeling activity. To evaluate age-related changes, I compare the differences in the prevalence and spatial distribution of cranial blood vessels and skeletal progenitors between juvenile (4-week-old) and adult mice (12-week-old). Then, I employ two different murine models to study how altering bone remodeling activity affects the cranial microvascular environment. To increase bone remodeling activity, I treat adult mice with intermittent parathyroid hormone therapy (PTH), a regimen that is known to stimulate osteoblast activity and has been used to treat osteoporosis in humans<sup>98,99</sup>. To suppress remodeling activity, I use a transgenic mouse model where PDGF-BB is conditionally knocked down in TRAP+ osteoclasts and preosteoclasts<sup>55</sup>. This mouse model has been shown to reduce angiogenesis of CD31<sup>hi</sup>Emcn<sup>hi</sup> vessels and osteogenesis during long bone remodeling<sup>55</sup>. These experiments build upon Chapter 2 by broadening our understanding of how the relationship between blood vessels and skeletal progenitors changes with different ages and levels of remodeling activity.

## 3.2 Methods

### 3.2.1 Materials

All essential antibodies, reagents, animal drugs and materials, instruments and hardware, and software used in this chapter are provided in **Appendix I**.

### 3.2.2 Study Approval

All animal experiments were approved by the Johns Hopkins University Institutional Animal Care and Use Committee (Protocol No. MO18M188). Animals were housed and cared for in Johns Hopkins' Research Animal Resources central housing facilities.

### 3.2.3 Experimental Animals

We purchased the following mouse strains from Jackson Laboratories: C57BL/6J (Stock No. 000664) and *Pdgfb*<sup>fl/fl</sup> (Stock No. 017622). We obtained *Trap-cre* mice from J.J. Windle (Virginia Commonwealth University, Richmond, VA, USA). *Trap-cre Pdgfb*<sup>fl/fl</sup> mice were generated using a previously published protocol<sup>55</sup>. Briefly, hemizygous *Trap-cre* mice were crossed with *Pdgfb*<sup>fl/fl</sup> mice to produce *Trap-cre Pdgfb*<sup>fl/fl</sup> offspring (referred to as *Pdgfb*<sup>CKO</sup> in the Main section). *Pdgfb*<sup>fl/fl</sup> mice were used as a control and referred to as WT in the Main section. Mice genotype was confirmed by performing PCR on DNA isolated from mouse toes using primers designated previously<sup>55</sup>. All mice with the C57BL/6J genetic background were male and either 4 or 12 weeks old at the time of harvest (age specified in each experiment). WT (*Pdgfb*<sup>fl/fl</sup>) and *Pdgfb*<sup>CKO</sup> mice were female and 4-5 weeks old at the time of harvest.

### 3.2.4 PTH Administration

We administered parathyroid hormone (PTH) daily for one month to determine the effects of stimulated bone remodeling on calvarial vessels and skeletal progenitors. 40 µg/kg pTH (1-34) was injected subcutaneously into male 8-week-old C57BL/6J mice 5 days/week for 4 weeks. Mice were

harvested at 12 weeks of age on the day following the last PTH dose. 12-week-old male C57BL/6J mice without PTH treatment were used as the control for quantitative comparisons.

### **3.2.5 Murine Calvarial Harvest**

See Section 2.2.4 in Chapter 2.

### **3.2.6 Whole Mount Immunostaining and Optical Clearing**

See Section 2.2.5 in Chapter 2.

### **3.2.7 Light-sheet Imaging**

See Section 2.2.6 in Chapter 2.

### **3.2.8 Image Processing and Analysis**

See Section 2.2.7 in Chapter 2.

### **3.2.9 MicroCT Scanning**

We used  $\mu$ CT to analyze changes in bone microstructure between different experimental groups. Prior to scanning, TDE was gradually removed from the calvaria by washing in 50% TDE and then PBS several times at room temperature. Calvaria were scanned using a Bruker Skyscan 1275  $\mu$ CT with a 1 mm aluminum filter, 65 keV source voltage, 0.3° step rotation, and 9  $\mu$ m voxel size.

To analyze calvarial microstructure, we implemented a custom analysis pipeline in CTAN and CTVOL software. Scans were re-sliced along the transverse plane to provide a uniform scan orientation among all datasets. In the re-sliced scans, a rectangular VOI was selected at the mid-point of the parietal and posterior frontal bones with dimensions of 4.95 mm x 3.6 mm x 0.9 mm and 3.6 mm x 3.6 mm x 0.45 mm, respectively (first two dimensions along transverse plane; latter two dimensions along sagittal plane). For *Trap-cre Pdgfb<sup>fl/fl</sup>* mice and their WT littermates, the VOI dimensions were reduced to 4.05 mm x 2.7 mm x 0.9 mm in the parietal bone and 2.7 mm x 2.7 mm x 0.45 mm in the posterior frontal

bone. Calvarial bone was segmented using a pre-defined threshold that remained constant across all scans. The shrink wrap function was subsequently performed to reduce the VOI to the boundaries of the tissue volume. 3D analysis was performed on the final segmented structure to assess bone volume (BV), bone volume/tissue volume (BV/TV), and bone surface area to volume ratio (SA/V).

### 3.2.10 Statistics

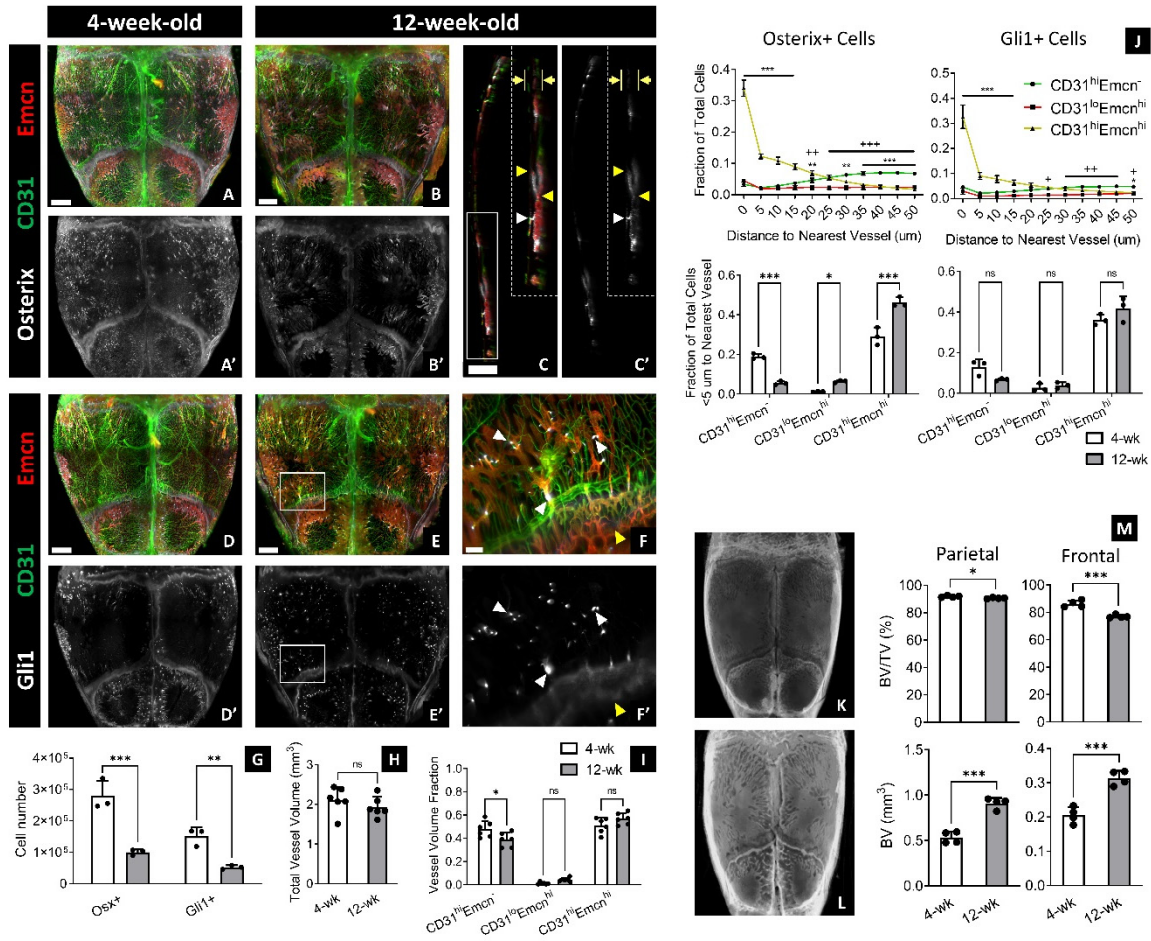
We used GraphPad Prism 5 software to perform all statistical analyses. All measurements were performed on distinct samples for each type of analysis. Statistical comparisons were performed using a two-tailed t-test, one-way ANOVA with Tukey's post-hoc test, or two-way ANOVA with Bonferroni's post-hoc test. Statistical tests performed and sample sizes for each dataset is designated in the figure captions. All p-values less than 0.05 were considered statistically significant.

## 3.3. Results

### 3.3.1 Post-natal Growth Shifts the Distribution of Vessel Phenotypes and Osterix+ Progenitors

We compared the calvaria of juvenile (4-week-old) and adult (12-week-old) mice to determine how vessel phenotype and skeletal progenitor distribution changes following post-natal growth. In adult mice, there were fewer CD31<sup>hi</sup>Emcn<sup>-</sup> periosteal and meningeal vessels and visible increases in CD31<sup>lo</sup>Emcn<sup>lo</sup> sinusoids (not quantified due to low fluorescence intensity, **Figure 3.1A-F, I**). These changes were corroborated by microCT data, which showed greater development of bone marrow cavities in adult calvaria (**Figure 3.1K-M**). There were no significant changes in the volume of CD31<sup>hi</sup>Emcn<sup>hi</sup> or CD31<sup>lo</sup>Emcn<sup>hi</sup> sinusoids, although fewer CD31<sup>hi</sup>Emcn<sup>hi</sup> vessels were observed in the periosteum and dura mater (**Figure 3.1A-F, I**). Additionally, total vessel volume remained the same (**Figure 3.1H**).





Along with changes in vessel phenotypes, the numbers of Osterix+ and Gli1+ skeletal progenitors decreased in adult calvaria, and their distribution was mainly restricted to sutures, transcortical canals, and bone marrow cavities (**Figure 3.1A-F, G**). While a decrease in progenitors was observed in different regions of the calvarium, the most significant decline occurred in the parietal bones (**Figure 3.2A**). Moreover, Osterix+ cells were mostly absent in the periosteum and dura mater of adult calvaria (**Figure 3.1A-C**). These results correlated with differences in vessel-progenitor relationships: The fraction of Osterix+ cells within 5  $\mu\text{m}$  of the nearest vessel in adult versus juvenile calvaria was significantly higher for CD31<sup>hi</sup>Emcn<sup>hi</sup> and CD31<sup>lo</sup>Emcn<sup>hi</sup> vessels and lower for CD31<sup>hi</sup>Emcn<sup>-</sup> vessels (**Figure 3.1J**). These trends held across different regions of the calvarium (**Figure 3.2B**). There were no significant changes in the relationship of Gli1+ cells to vessel phenotype between juvenile and adult calvaria (**Figure 3.1J**). Nonetheless, both progenitor cell types maintained a preferential spatial association with CD31<sup>hi</sup>Emcn<sup>hi</sup> vessels at 4 and 12 weeks of age.

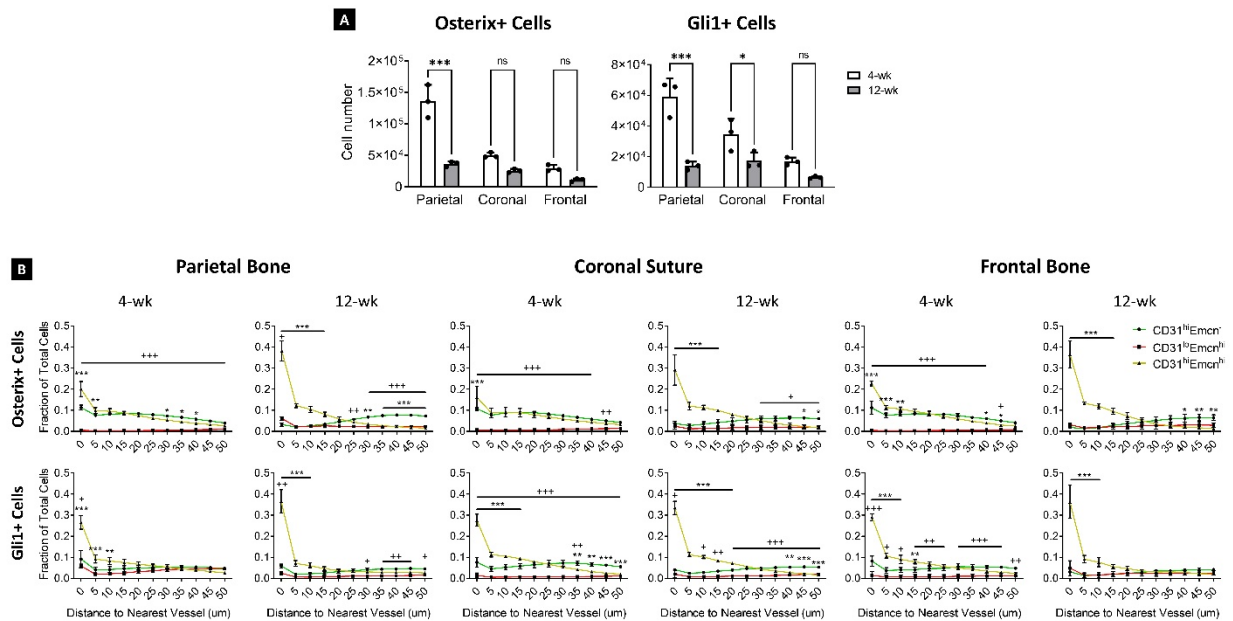
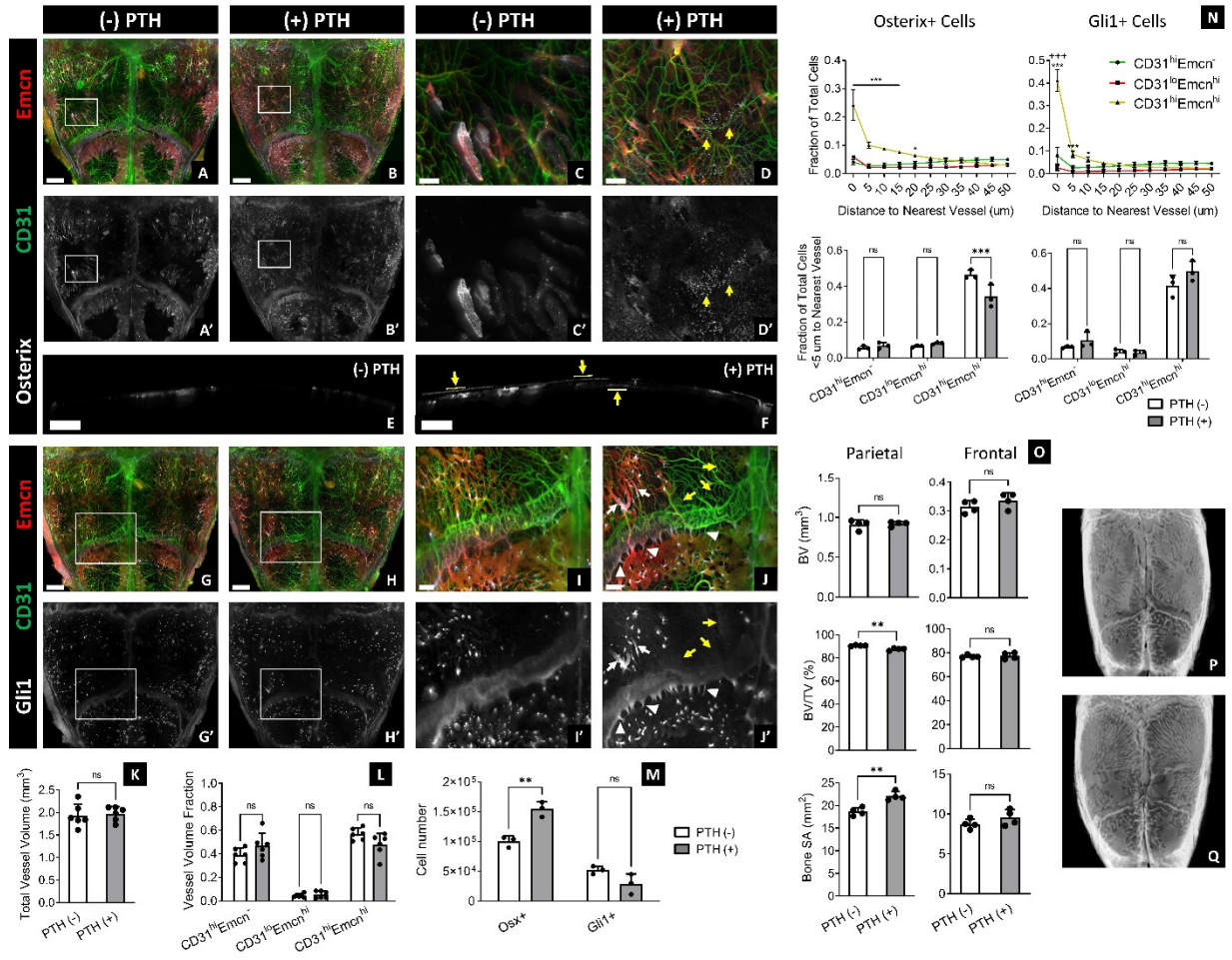


**Figure 3.2: Distribution of skeletal progenitors in different regions of the calvarium. A** Number of Osterix+ and Gli1+ cells in each region for 4-wk and 12-wk-old mice (n=3). **B** Plots showing the nearest distance of Osterix+ (top) and Gli1+ (bottom) progenitors to each vessel phenotype (n=3) in the parietal bones, frontal bones, and coronal suture (including parietal/frontal bones just adjacent to the suture). Data are mean  $\pm$  SD. Statistics were performed using a two-way ANOVA and Bonferroni post-hoc test. \*\*\*p<0.001, \*\*p<0.01, \*p<0.05 where designated or between CD31<sup>hi</sup>Emcn<sup>hi</sup> and CD31<sup>hi</sup>Emcn<sup>-</sup> vessels; +++p<0.001, ++p<0.01, +p<0.05 between CD31<sup>lo</sup>Emcn<sup>hi</sup> and CD31<sup>hi</sup>Emcn<sup>-</sup> vessels

### 3.3.2 PTH Stimulates Osterix+ Progenitor Proliferation, but Does Not Alter Vessel Phenotype Distribution

To provide insight on how vessel phenotypes and skeletal progenitors interact during calvarial bone remodeling, we administered a parathyroid hormone analogue (PTH 1-34) daily for one month, a regimen previously shown to increase osteoblast number and bone mineral deposition in murine long bone<sup>98</sup>. We found that PTH administration did not significantly change fractional volume for each vessel phenotype or total vessel volume; although, there were areas of increased *Emcn* signal intensity in sinusoids near the transcortical canals (**Figure 3.3A-D, G-J, K-L**). Furthermore, we observed increased marrow cavities and CD31<sup>lo</sup>*Emcn*<sup>lo</sup> sinusoids in the parietal bone with PTH administration—a finding complemented by decreased bone volume to total volume percentage (BV/TV) and increased bone surface area (SA) (**Figure 3.3O-Q**).

Despite a lack of significant change in vessel phenotypes, we found differences in the skeletal progenitor populations with PTH administration. PTH significantly increased the total number of Osterix+ progenitors, especially in the periosteum and dura mater (**Figure 3.3A-F, M**). By contrast, PTH did not increase the number of Gli1+ progenitors (**Figure 3.3G-J, M**). However, there were some changes in Gli1+ progenitor distribution. Cells moderately expressing Gli1 expanded in the marrow cavities adjacent to transcortical canals—particularly near vessels with high *Emcn* expression—and in periosteal and transcortical canals nearby the coronal suture (**Figure 3.3J**). Both Osterix+ and Gli1+ progenitors remained preferentially associated with CD31<sup>hi</sup>*Emcn*<sup>hi</sup> vessels following PTH administration, but the fraction of Osterix+ cells within 5  $\mu\text{m}$  of a CD31<sup>hi</sup>*Emcn*<sup>hi</sup> vessel was significantly reduced compared to the control (**Figure 3.3N**).



### 3.3.3 Loss of Preosteoclast PDGF-BB Secretion Decreases the Spatial Affinity of Skeletal Progenitors to CD31<sup>hi</sup>Emcn<sup>hi</sup> Vessels

Preosteoclast-derived PDGF-BB is required for angiogenesis with coupled osteogenesis during normal bone homeostasis and in disease conditions<sup>55,57</sup>. To determine the phenotypic changes in calvarial blood vessels and skeletal progenitors in response to decreased bone remodeling activity, we used Trap+ osteoclast lineage-specific conditional *Pdgfb* deletion mice (*Pdgfb*<sup>CKO</sup>) by crossing *Trap-Cre* mice with *Pdgfb*-floxed mice. In the calvaria of 4-week-old mice, we found that CD31<sup>hi</sup>Emcn<sup>hi</sup> fractional volume and total vessel volume decreased, while fractional CD31<sup>hi</sup>Emcn<sup>+</sup> vessel volume increased in *Pdgfb*<sup>CKO</sup> mice relative to *Pdgfb*-floxed (WT) mice (**Figure 3.4A-H, K-L**). While we did not find any statistical differences in the number of Osterix+ or Gli1+ cells, we found that the preferential association of these cells to CD31<sup>hi</sup>Emcn<sup>hi</sup> vessels was significantly reduced in *Pdgfb*<sup>CKO</sup> calvaria (**Figure 3.4I-J, M**). This effect was most apparent at the transcortical canals and osteogenic fronts, where the concentration of Osterix+ and Gli1+ cells was visibly lower in *Pdgfb*<sup>CKO</sup> versus WT calvaria (**Figure 3.4C-D, G-H**). We also observed alterations in bone microarchitecture: There was less bone marrow cavity development in the frontal bones of *Pdgfb*<sup>CKO</sup> calvaria, as demonstrated by a higher BV/TV percentage and lower bone SA (**Figure 3.4N-P**). To determine whether osteoclasts resided in close proximity to these regions, we stained for Vpp3—a marker known to exclusively stain osteoclasts in bone<sup>58</sup>. Most osteoclasts were found adjacent to CD31<sup>hi</sup>Emcn<sup>hi</sup> and CD31<sup>lo</sup>Emcn<sup>hi</sup> vessels in the marrow cavities and within proximity to the transcortical canals (**Figure 3.5A-C**).



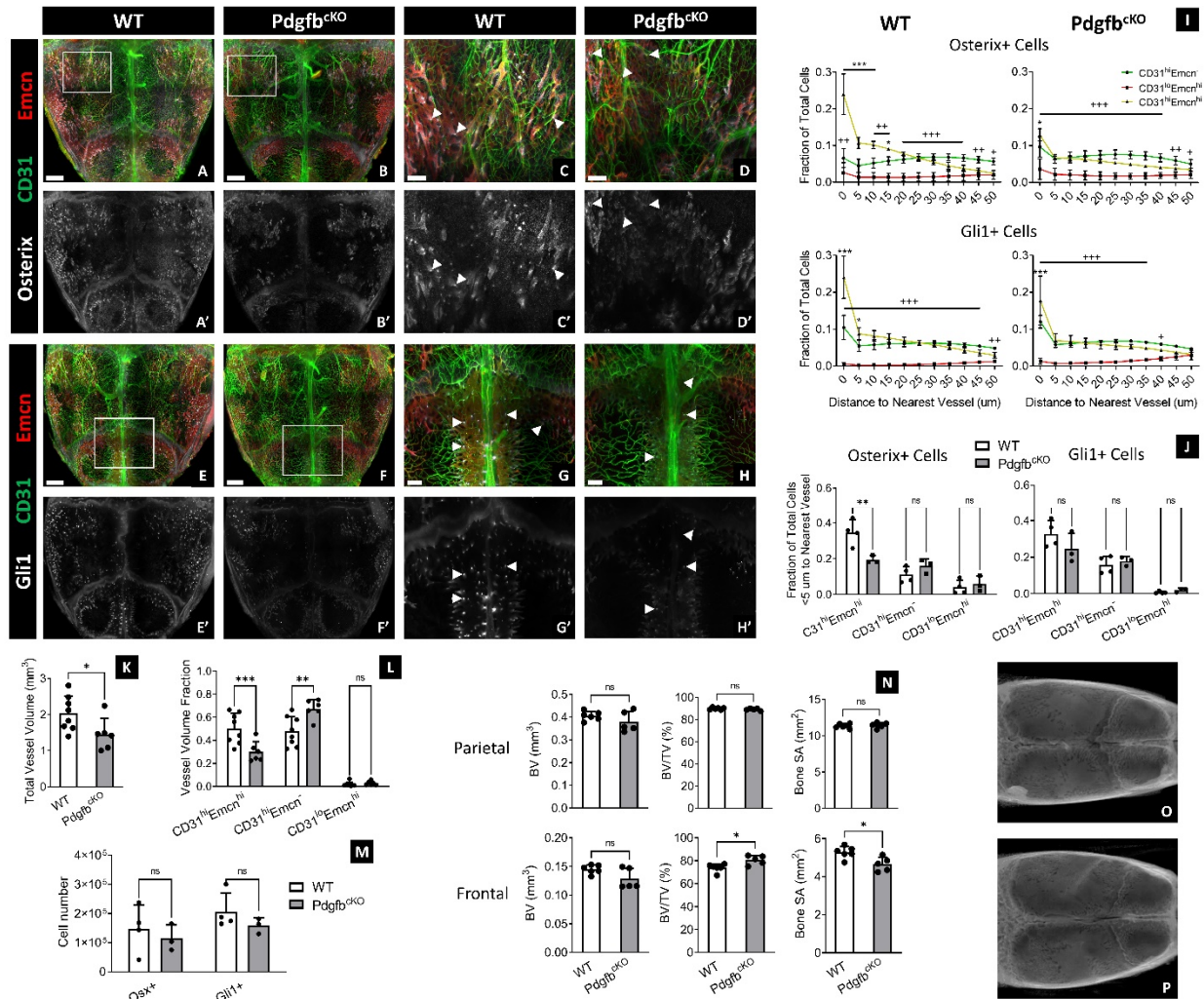


**Figure 3.4: Knocking out PDGF-BB expression in TRAP+ osteoclasts decreases CD31<sup>hi</sup>Emcn<sup>hi</sup> vasculature and their association with Osterix+ and Gli1+ skeletal progenitors.** A–H MIP of vessels (A–H), Osterix+ progenitors (A–D, A'–D'), and Gli1+ progenitors (E–H, E'–H') from the calvaria of 4-weeks-old WT and Pdgfb<sup>cko</sup> mice. Protein expression of CD31 and Emcn in vessels and Osterix or Gli1 in skeletal progenitors is markedly reduced in Pdgfb<sup>cko</sup> calvaria at the transcortical canals (arrowheads) and osteogenic fronts nearby the sutures. Results were replicated in 4 WT calvaria and 3 Pdgfb<sup>cko</sup> calvaria for each staining combination (14 total calvaria). I Spatial distribution of Osterix+ and Gli1+ cells relative to each vessel phenotype in WT and Pdgfb<sup>cko</sup> calvaria (WT: *n* = 4 Osterix, *n* = 4 Gli1; Pdgfb<sup>cko</sup>: *n* = 3 Osterix, *n* = 3 Gli1). J Fraction of Osterix+ and Gli1+ progenitors within 5 μm of their nearest vessel in WT and Pdgfb<sup>cko</sup> calvaria (WT: *n* = 4 Osterix, *n* = 4 Gli1; Pdgfb<sup>cko</sup>: *n* = 3 Osterix, *n* = 3 Gli1). Significantly fewer Osterix+ cells are associated with CD31<sup>hi</sup>Emcn<sup>hi</sup> vessels in Pdgfb<sup>cko</sup> calvaria compared to the WT control. K–M Total vessel volume (K), fractional vessel phenotype volume (L), and skeletal progenitor number (M) in the calvaria of WT versus Pdgfb<sup>cko</sup> mice (*n* = 8 for WT and *n* = 6 for Pdgfb<sup>cko</sup> in K–L; M: *n* is the same as in I and J). N MicroCT quantification of bone volume (BV), bone volume to tissue volume (BV/TV) percentage, and bone surface area (SA) in the parietal and posterior frontal bones of WT and Pdgfb<sup>cko</sup> calvaria (WT: *n* = 6; Pdgfb<sup>cko</sup>: *n* = 5). O, P MicroCT 3D volume projections of WT (O) and Pdgfb<sup>cko</sup> calvaria (P). Data are mean ± SD. Statistics were performed using a two-way ANOVA with Bonferroni post-hoc test (I, J, L, M) or two-tailed *t*-test (K, N). \*\*\**p* < 0.001, \*\**p* < 0.01, \**p* < 0.05 where designated or between CD31<sup>hi</sup>Emcn<sup>hi</sup> and CD31<sup>hi</sup>Emcn<sup>-</sup> vessels in I; +++*p* < 0.001 between CD31<sup>lo</sup>Emcn<sup>hi</sup> and CD31<sup>hi</sup>Emcn<sup>-</sup> vessels (I). Exact *p*-values for two-tailed *t*-tests: K *p* = 0.0112, N *p* = 0.2565 (top left), 0.0736 (bottom left), 0.2183 (top middle), 0.0152 (bottom middle), 0.6635 (top right), 0.0151 (bottom right). Scale bars: 1000 μm (A, B, E, F, O, P); 300 μm (C, D, G, H). Colors: Red: Endomucin (Emcn), Gray: Osterix (A–D) or Gli1 (E–H), Green: CD31.

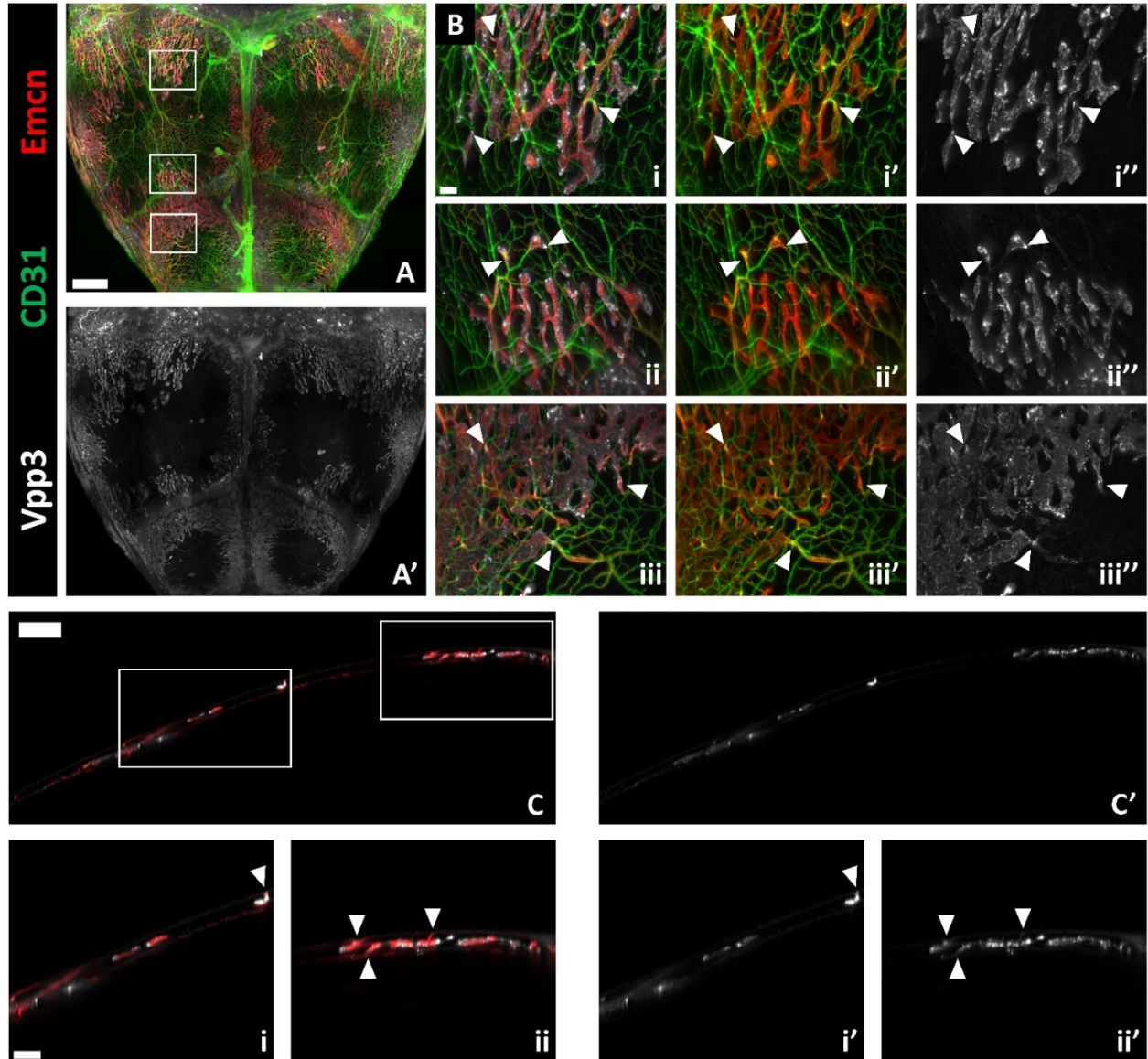


**Figure 3.5: Osteoclasts reside in the marrow cavities and transcortical canals.** **A** MIP of vessels and Vpp3+ osteoclasts in the calvarium from a 4-week-old mouse. **B** Zoomed-in regions from **(A)** demonstrating the spatial distribution of osteoclasts relative to vessels. Arrowheads point to regions where osteoclasts reside at or adjacent to transcortical canals. **C** 40 μm-thick sagittal section displaying the distribution of osteoclasts relative to Emcn<sup>hi</sup> transcortical and marrow vessels. Arrowheads indicate regions where osteoclasts reside nearby Emcn<sup>hi</sup> transcortical vessels. Images were acquired from 1 calvarium. Scale bars: 1000 μm (**A**); 500 μm (**C**); 200 μm (**Ci-ii**); 100 μm (**B**). Colors: Red: Endomucin (Emcn), Gray: Vpp3, Green: CD31

### 3.4 Conclusion

In this Chapter, I studied how the prevalence and distribution of blood vessels and skeletal progenitors change during postnatal growth and remodeling. After postnatal growth, skeletal

progenitors and CD31<sup>hi</sup>Emcn<sup>-</sup> arteries declined, but the preferential spatial relationship of skeletal progenitors and CD31<sup>hi</sup>Emcn<sup>hi</sup> vessels was maintained, and even more pronounced in adult compared to juvenile mice. This spatial relationship was also sustained following 4 weeks of PTH administration. However, the increased number of Osterix<sup>+</sup> osteoprogenitors in the periosteum and dura mater observed with PTH treatment was not coupled with an increase in CD31<sup>hi</sup>Emcn<sup>hi</sup> vessels. Moreover, osteoprogenitors appeared less spatially associated with blood vessels in the periosteum and dura mater of non-treated mice. These results suggest that there is a weaker relationship between blood vessels and osteoprogenitors in the periosteum and dura mater compared to other regions, such as the bone marrow cavities and transcortical canals. On the other hand, the spatial relationship between CD31<sup>hi</sup>Emcn<sup>hi</sup> vessels and skeletal progenitors was significantly weakened with a conditional knockout of PDGF-BB in TRAP<sup>+</sup> osteoclasts and preosteoclasts in juvenile mice. This suggests that PDGF-BB signaling by preosteoclasts may be critical for maintaining the intimate relationship of CD31<sup>hi</sup>Emcn<sup>hi</sup> vessels and skeletal progenitors during postnatal cranial bone growth. Collectively, these data build upon the findings from Chapter 2 to provide a framework for how blood vessels and skeletal progenitors spatially interact during postnatal cranial bone growth and remodeling.



# Chapter 4 : Relationship Between the Microvasculature and Skeletal Progenitors During Cranial Bone Healing

## 4.1 Introduction

Each year, thousands of patients worldwide suffer from critical-sized craniofacial bone defects as a result of trauma, cancer, or congenital conditions, resulting in over \$600 billion in annual healthcare costs<sup>100</sup>. Because these defects are unable to heal on their own, they require treatment with bone grafts to fill the void space in the skull and restore functionality. Autografts—autologous bone that is typically harvested from the iliac crest of fibula—are the current gold standard for treatment of craniofacial bone defects, but they have significant drawbacks, including a high risk of donor site morbidity and limited availability<sup>101</sup>. Alternatives such as allografts and synthetic grafts overcome these issues, but their poor biological properties and higher infection risk limits their application in the clinic<sup>101,102</sup>. There remains a critical need to develop regenerative therapies that enable complete restoration of the lost bone while mitigating the risks associated with current treatment methods.

One of the key limitations to developing regenerative bone graft therapies is the lack of fundamental knowledge of how native cranial bone healing takes place at a cellular and molecular level. In particular, inadequate vascularization has been linked to poor bone healing, but it remains unclear how blood vessels contribute to the overall healing process<sup>8</sup>. In this chapter, I first give an overview of the biology of cranial bone healing, with an emphasis on the role of vasculature and skeletal progenitors, and highlight the remaining knowledge gaps. Then, I apply QLSM to study the relationship of blood vessel and skeletal progenitor subtypes during cranial bone healing. The results from this

chapter will inform the development of next-generation bone grafts for treatment of critical-sized craniofacial bone defects.

#### 4.1.1 Critical-Sized Defect Determination

Determination of the critical size for craniofacial defects is essential for patient care and preclinical research. Critical sized defects were initially defined as “defects of a size that will not heal during the lifetime of the animal<sup>103</sup>.” More recently, some have applied more rigorous definitions of critical-sized defect, where a defect must show less than 10% regeneration during the animal’s lifetime<sup>104</sup>. Nonetheless, the critical size defect is difficult to precisely define, as it is dependent upon factors such as anatomical location, soft tissue environment, age, and comorbidities<sup>104</sup>. In this section, I provide an overview of the preclinical studies defining critical-sized defects in murine models and discuss the different variables that affect critical-sized defect determination.

Cowan *et al.* (2004)<sup>105</sup> was one of the first studies to define the critical size of a cranial defect in wild type adult mice. They created parietal bone defects ranging from 0.8- to 5.0-mm in size in male FBV adult mice (2- to 3-month-old) and evaluated healing after 12 weeks<sup>105</sup>. They found that only the 0.8-mm-sized defects spontaneously healed, while defects 2-mm or greater in size did not completely heal<sup>105</sup>. However, they used the 4-mm size in the rest of the study to evaluate stem cell-based therapies, implying that a 4-mm size was needed to satisfy the most rigorous definition of a critical-sized defect<sup>105</sup>. Another study done by Aalami *et al.* (2003)<sup>106</sup> found that parietal bone defects 3-, 4-, and 5-mm in size healed less than 5% over an 8-week period, further reinforcing that these sizes could be considered critical. Most studies since have employed the 3-4-mm-sized parietal bone defect model to evaluate regenerative bone graft therapies<sup>107</sup>.

While Cowan *et al.* and Aalami *et al.* established the critical size for parietal bone defects, it was still unclear whether defects >0.8-mm in size would heal over longer time intervals. Cooper *et al.*

(2010)<sup>108</sup> addressed this question by evaluating healing in parietal bone defects over a 1-year timespan. They found that 1.8-mm defects only healed up to a maximum of 52% at 1-year post-injury, and that minimal healing occurred after 8 weeks following injury. These data reinforce the results from the previous studies finding that parietal bone defects >0.8-mm do not spontaneously heal and suggest that most healing takes place within the first 8 weeks of injury.

Although these studies establish the critical-sized defect in the parietal bone of adult mice, the amount of healing that takes place is dependent on various factors, including age, anatomical location, and immune system function. Multiple studies have shown that parietal bone defects heal significantly better in juvenile compared to adult mice (6-7-day- versus 60-day-old mice)<sup>106,109,110</sup>. For instance, Aalami *et al.* (2003)<sup>106</sup> showed that 4-mm parietal bone defects were 65% healed by 8 weeks in juvenile mice, while healing in adult mice was less than 5%. While the mechanisms of this enhanced healing response are not completely understood, one study found that expression of osteogenic ECM proteins, growth factors, and growth factor receptors in the defects of juvenile mice was significantly higher compared to adult mice<sup>110</sup>. Additionally, there was a higher expression of osteoclast genes, which implied that the juvenile mice had increased bone mineralization and remodeling activity during cranial bone healing<sup>110</sup>.

While studies have demonstrated differences in healing during postnatal development, minimal research has been done to study how aging affects the cranial healing process. One study performed by Charles *et al.* (2015)<sup>111</sup> compared the parietal bone healing in young adult (2-4-month-old) versus aged mice (24-month-old) and did not find significant differences between the groups when treated with a scaffold alone or with BMP-2. However, as aging is known to negatively impact bone mineral density and long bone fracture healing<sup>112</sup>, further research should be done to better understand how cranial bone healing changes with age.

Besides age, anatomical location also affects the critical defect size in cranial bone. Multiple studies have shown that the frontal bone—which originates from the neural crest—heals better than the mesoderm-derived parietal bone<sup>109,113–115</sup>. For instance, Behr *et al.* (2010)<sup>113</sup> showed that healing in 2-mm defects was >20x higher in the frontal compared to parietal bones 12 weeks after injury. The superior healing capacity of the frontal bones may be due to the higher levels of canonical Wnt, FGF, and BMP signaling and lower levels of TGF $\beta$  signaling in frontal versus parietal bone osteoblasts<sup>116</sup>. Studies have shown that enhancing Wnt and FGF signaling increases healing in the parietal bone, while inhibiting Wnt signaling decreases healing in the frontal bone<sup>113–115</sup>. Besides the differences between the cranial bones, the proximity of the defect to the sutures in either of the bones could potentially affect healing outcomes, as skeletal stem cells derived from the sutures are known to contribute to cranial bone healing<sup>33,117,118</sup>. However, more research is needed to determine whether the distance between the injury and adjacent suture significantly affects regenerative outcomes.

Another factor affecting cranial bone healing is the immune status of the animal. Many studies have evaluated healing in immunocompromised mouse models in order to test experimental stem cell-based therapies. Immunocompromised mice—which lack T cells and lack or have dysfunctional B cells—are used to prevent rejection of stem cells derived from different mouse strains or species. However, the adaptive immune system is known to be important for tissue regeneration, including long bone fracture healing<sup>119</sup>. While no studies have performed a direct comparison between wild type versus immunocompromised mice, results from separate reports with comparable defect models have shown markedly reduced healing in immunocompromised mice, regardless of the anatomical location of the defect<sup>109,114</sup>. Besides immunocompromising conditions, studies have also shown that chronic inflammation and some forms of acute inflammation may impair bone fracture healing, suggesting that the immune system could impair cranial bone healing under some circumstances<sup>120,121</sup>. Therefore,

further consideration should be made regarding the immune status of the animal when evaluating cranial bone healing.

While the collective findings of these studies highlight the different variables that affect critical-sized defect determination in mice, other factors such as gender, disease/co-morbidities, and prior history of cranial injury could affect cranial bone healing outcomes. Such factors should be studied in the future in order to provide a broader understanding of how innate biological and physiological characteristics affect cranial bone healing.

#### **4.1.2 Biology of Cranial Bone Healing**

Bone healing involves a complex coordination of different cell types, including skeletal progenitors, osteoblasts, vascular cells, and immune cells, that contribute to different stages of the healing process<sup>122</sup>. While long bone fracture healing—which follows an endochondral pathway—is well characterized, cranial bone healing typically heals via intramembranous pathway, and the cellular interactions governing the healing process are less known<sup>123</sup>. For instance, while it has been shown that vascularization is critical for proper cranial bone healing<sup>8</sup>, it is not fully understood how blood vessels interact with osteoblasts and skeletal progenitors during the healing process. Here, I outline the current knowledge of the spatiotemporal cellular dynamics of cranial bone healing with an emphasis on vascularization.

Studies using intravital microscopy and transgenic mouse reporters have been able to visualize the timing of skeletal progenitor, osteoblast, and vessel infiltration during cranial bone healing. Huang *et al.* (2015)<sup>77</sup> used these techniques to characterize osteoblast infiltration, angiogenesis, and bone matrix deposition in 1-mm parietal bone defects. They found that blood vessels rapidly grew into the injury site during the first two weeks of injury, followed by infiltration of Col1+ osteoblasts at the leading edges of the defect region<sup>77</sup>. Osteoblasts in the defect appeared to reside in close proximity to the blood vessels;

although, no quantification was performed to characterize their spatial relationships<sup>77</sup>. After the first three weeks of healing, the blood vessels pruned and remodeled—with some forming sinusoidal-like vessels—and the rate of osteoblast infiltration decreased compared to the early stages of healing<sup>77</sup>. Most of the bone matrix deposition also occurred within the first four weeks of injury<sup>77</sup>. These data suggest that the cellular events at the early stages of healing dictate the overall regenerative response.

Some studies have also evaluated skeletal progenitor (skeletal stem cells and osteoprogenitors) migration into the defect, showing that they rapidly infiltrate into the defect and directly contribute to the early stages of healing<sup>76,124</sup>. Park *et al.* (2014)<sup>76</sup> developed a Mx1-Tomato reporter in mice to track skeletal progenitor fate after a frontal bone defect injury. They found that Tomato+ skeletal progenitors were present in the defect by Day 3 after injury and proliferated across the entire defect by Day 10<sup>76</sup>. Ortinau *et al.* (2019)<sup>124</sup> built upon these results by showing that by Day 21, Mx1+ $\alpha$ SMA+ periosteal skeletal progenitors restored the periosteal layer above the defect region and directly contributed to new bone formation by differentiating into osteoblasts and osteocytes. Other studies have also shown that suture-derived skeletal stem cells migrate to and proliferate around the injury site, suggesting that multiple skeletal progenitor sources likely contribute to the healing process<sup>33,117,118</sup>. Nevertheless, these studies did not evaluate the relationship of the skeletal progenitors to the neovasculature in the defect region, so it remains unclear whether there are interactions between these cell types during healing.

While the papers reviewed in this Section have established the timing by which blood vessels, skeletal progenitors, and osteoblasts infiltrate into cranial defect injuries, it remains unknown whether different the blood vessel phenotypes observed during long bone growth and healing are also present during cranial bone healing. Furthermore, while it has been assumed that blood vessels are spatially coupled with skeletal progenitors during cranial bone healing, no studies have quantitatively assessed the spatial relationships of these cell types during this process. In this Chapter, I address these

knowledge gaps by evaluating the prevalence and spatial distribution of different blood vessel and skeletal progenitor subtypes using a 1-mm-sized parietal bone defect model.

## **4.2 Methods**

### **4.2.1 Materials**

All essential antibodies, reagents, animal drugs and materials, instruments and hardware, and software used in this chapter are provided in **Appendix I**.

### **4.2.2 Study Approval**

All animal experiments were approved by the Johns Hopkins University Institutional Animal Care and Use Committee (Protocol No. MO18M188). Animals were housed and cared for in Johns Hopkins' Research Animal Resources central housing facilities.

### **4.2.3 Experimental Animals**

Surgeries were performed on 8-week-old male C56BL/6J mice from Jackson Laboratories (Stock No. 000664) for all experiments in this chapter. Mice were harvested at 11 and 16 weeks of age..

### **4.2.4 Calvarial Defect Procedure**

We created a subcritical 1-mm sized defect in the parietal bone to characterize the response by vessel phenotypes and skeletal progenitors during calvarial healing. 8-week-old male C57BL/6J mice were weighed and anesthetized via a single intraperitoneal injection using ketamine (100 mg/kg) and xylazine (10 mg/kg). The paw-pitch test was performed to determine the level of sedation. Then, mice were placed on a stereotactic frame to fix the head. Buprenorphine SR (1 mg/kg) was injected subcutaneously to provide sustained analgesia following the procedure. To access the parietal bone, the skin was shaved, treated with alcohol and betadine, and draped under sterile conditions. Sterile gloves

and masks were used by all surgical personnel, and all the surgical procedures were performed under an operating microscope by a single surgeon. A mid-sagittal incision was made over the center of calvarium. Following identification of anatomical landmarks, a 1-mm defect was created approximately 1-2 mm away from the sagittal suture using a microsurgical drill and 1 mm carbide inverted bone burr. Special precaution was taken to preserve the underlying dura mater. Following defect creation, the skin incision was closed using 6-0 nylon monofilament sutures. Mice were monitored daily up to one week following surgery for any neurological deficit, infection, pain or distress. After 21- and 56-days following surgery, all mice were euthanized and calvaria were harvested according to the same procedure described in Section 2.2.4 of Chapter 2.

#### **4.2.5 Murine Calvarial Harvest**

See Section 2.2.4 in Chapter 2.

#### **4.2.6 Whole Mount Immunostaining and Optical Clearing**

See Section 2.2.5 in Chapter 2.

#### **4.2.7 Light-sheet Imaging**

See Section 2.2.6 in Chapter 2.

#### **4.2.8 Image Processing and Analysis**

See Section 2.2.7 in Chapter 2 for full details on the image processing and analysis pipelines. To quantify vasculature and skeletal progenitors in our defect model, we applied the same approach using modified VOIs. A VOI with a 1 mm x 1 mm x-y area was placed in the defect region to calculate vessel volume and skeletal progenitor number within the defects. Additionally, to assess the systemic response to injury, an expanded VOI with a 2.3 mm x 3.6 mm x-y area was positioned in the ipsilateral and



contralateral parietal bone approximately 1 mm away from the sagittal suture. The z-dimension of all VOIs spanned the full thickness of the calvarial bone.

#### **4.2.9 MicroCT Scanning**

We used  $\mu$ CT to analyze changes in bone microstructure between different experimental groups. Prior to scanning, TDE was gradually removed from the calvaria by washing in 50% TDE and then PBS several times at room temperature. Calvaria were scanned using a Bruker Skyscan 1275  $\mu$ CT with a 1 mm aluminum filter, 65 keV source voltage, 0.3° step rotation, and 9  $\mu$ m voxel size. For the analysis, we quantified newly formed bone in the defects using Mimics 14 software. Bone was segmented using a pre-defined threshold that was held constant among all datasets. Cylindrical VOIs with a 1 mm diameter were placed within the defect and in the contralateral parietal bone to allow for quantification of defect/contralateral bone volume.

#### **4.2.10 Statistics**

We used GraphPad Prism 5 software to perform all statistical analyses. All measurements were performed on distinct samples for each type of analysis. Statistical comparisons were performed using a two-tailed t-test, one-way ANOVA with Tukey's post-hoc test, or two-way ANOVA with Bonferroni's post-hoc test. Statistical tests performed and sample sizes for each dataset is designated in the figure captions. All p-values less than 0.05 were considered statistically significant

### **4.3 Results**

#### **4.3.1 CD31<sup>hi</sup>Emcn<sup>hi</sup> vessels and Gli1+ progenitors infiltrate into calvarial defect following injury**

In this study, we investigated the contribution of vessel phenotypes and skeletal progenitors to calvarial bone healing. We created 1-mm sub-critical sized defects in the parietal bone of adult mice and

evaluated healing at 21- and 56-days following fracture (PFD21, PFD56; PFD: post-fracture day). At PFD21, defects were highly vascularized, and the majority of vessels were CD31<sup>hi</sup>Emcn<sup>hi</sup> (**Figure 4.1A-B, E-F, L, N**). Gli1<sup>+</sup> cells were highly concentrated across the entire defect region, while Osterix<sup>+</sup> cells resided in regions of active bone formation (**Figure 4.1A-B, E-F; Figure 4.2A**). In addition, there was a substantial expansion of Osterix<sup>+</sup> and Gli1<sup>+</sup> cells in the periosteum extending from the defect to nearby sutures (**Figure 4.1A-B, E-F, I-J**). This effect was unique to the periosteum, as there were few Osterix<sup>+</sup> and Gli1<sup>+</sup> cells detected in the dura mater—the only layer that remained uninjured following creation of the defect (**Figure 4.1I-J**). By PFD56, total vessel volume, fractional CD31<sup>hi</sup>Emcn<sup>hi</sup> volume, Osterix<sup>+</sup> cell number, and Gli1<sup>+</sup> cell number decreased in the defect relative to PFD21, but vessel and Gli1<sup>+</sup> cell density remained higher relative to the surrounding un-injured bone (**Figure 4.1C-D, G-H, L-N**). Furthermore, there was no significant change in defect bone volume, suggesting that most healing happened within the first three weeks of injury (**Figure 4.1O, Figure 4.2A-B**). Nevertheless, both Osterix<sup>+</sup> and Gli1<sup>+</sup> progenitors remained preferentially associated with CD31<sup>hi</sup>Emcn<sup>hi</sup> vessels at PFD21 and PFD56 (**Figure 4.1K**).

### **4.3.2 Localized Defect Injury Stimulates Systemic Expansion of Gli1<sup>+</sup> Progenitors in the Periosteum**

Since there was a significant expansion of skeletal progenitors around the defect region, we evaluated whether there was a systemic response to injury. We quantified skeletal progenitors in the ipsilateral and contralateral sides of the parietal bone and compared them to the number of progenitors in uninjured adult mice. Surprisingly, there were elevated levels of Gli1<sup>+</sup> cells in both the ipsilateral and contralateral sides of the injured calvaria at PFD21 compared to the uninjured calvaria (**Figure 4.2D-S**). Most of this expansion occurred in the periosteum, especially in the regions nearby the suture (**Figure 4.2D, G, J, M**). By PFD56, Gli1<sup>+</sup> and Osterix<sup>+</sup> cell number significantly decreased to levels comparable to

the uninjured calvaria (**Figure 4.2P-S**). However, alterations in bone surface topography and regions of excess mineral formation remained at PFD56 (**Figure 4.2A-C**).

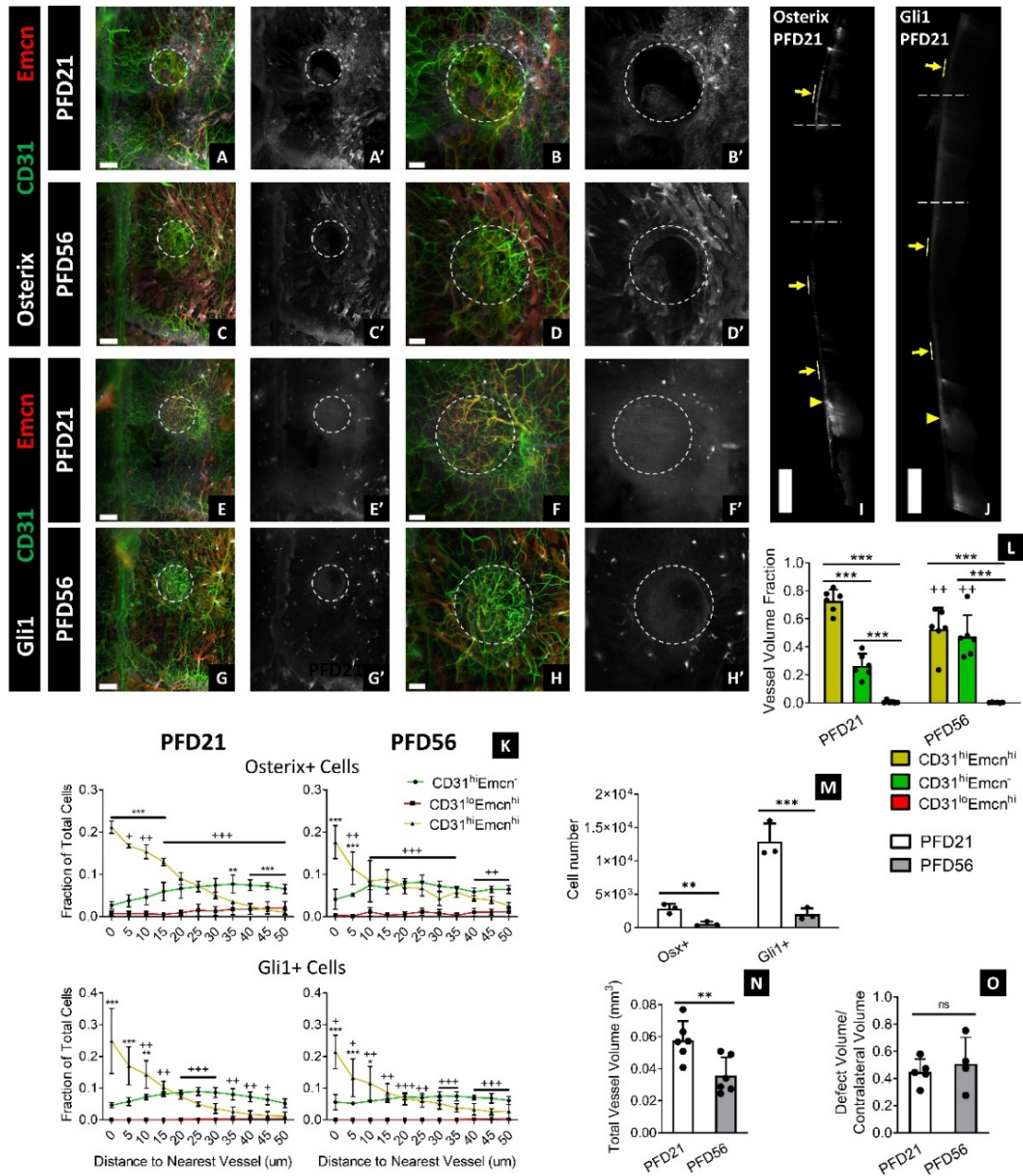


**Figure 4.1: CD31<sup>hi</sup>Emcn<sup>hi</sup> vessels and skeletal progenitors expand and infiltrate into subcritical-sized defects during healing.** A–H Blood vessels (A–H), Osterix+ progenitors (A–D, A'–D'), and Gli1+ progenitors (E–H, E'–H') inside and around 1-mm parietal bone defects at PFD21 (A, B, E, F) and PFD56 (C, D, G, H). The dotted circle marks the defect region. I, J Expansion of Osterix+ and Gli1+ progenitors in the periosteum (yellow arrows) nearby the defect region (dotted lines) and sutures (yellow arrowheads) at PFD21. Progenitors were sparsely populated in the dura mater—the only portion of the calvarium that remained intact following defect injury. Results were replicated in 3 calvaria for each timepoint and staining combination (12 total calvaria). **K** Spatial relationship of skeletal progenitors to different vessel phenotypes at PFD21 and PFD56 ( $n = 3$ ). **L–N** Fractional vessel phenotype volume (**L**), skeletal progenitor number (**M**), and total vessel volume (**N**) in the defect at PFD21 and PFD56 ( $n = 6$  for **L, N**;  $n = 3$  for **M**). **O** MicroCT quantification of defect to contralateral bone volume ratio at PFD21 and PFD56 ( $n = 4$ ). Data are mean  $\pm$  SD. Statistics were performed using a two-way ANOVA with Bonferroni post-hoc test (**K–M**) or two-tailed  $t$ -test (**N–O**). \*\*\* $p < 0.001$ , \*\* $p < 0.01$ , \* $p < 0.05$  where designated or between CD31<sup>hi</sup>Emcn<sup>hi</sup> and CD31<sup>hi</sup>Emcn<sup>lo</sup> vessels in **K**; \*\*\* $p < 0.001$  between CD31<sup>lo</sup>Emcn<sup>hi</sup> and CD31<sup>hi</sup>Emcn<sup>lo</sup> vessels. Exact  $p$ -values for two-tailed  $t$ -tests: **N**  $p = 0.0094$ , **O**  $p = 0.5660$ . Scale bars: 500  $\mu$ m (I, J); 300  $\mu$ m (A, C, E, G); 200  $\mu$ m (B, D, F, H). Colors: Red: Endomucin (Emcn), Gray: Osterix (A–D, I, J) or Gli1 (E–H), Green: CD31.

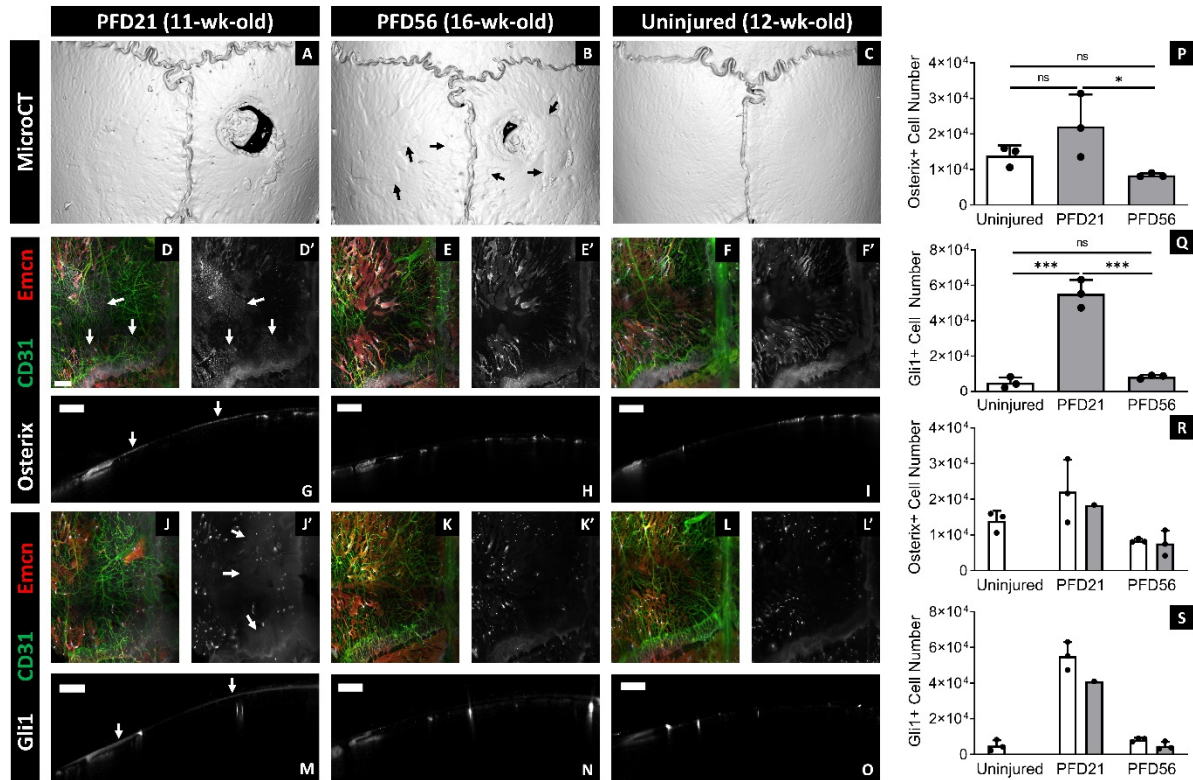


**Figure 4.2: Localized calvarial injury stimulates systemic skeletal progenitor expansion.** A-C MicroCT 3D surface renderings of injured calvaria at PFD21 (A) and PFD56 (B) compared to an uninjured calvarium (C). Black arrows point to regions of excess mineral deposition along the cortical surface of injured calvaria (B). Results were replicated in 3 calvaria from the 11- and 12-wk-old mice and 4 calvaria from the 16-wk-old mice. D-F MIP of calvarial vessels and Osterix+ skeletal progenitors in the contralateral parietal bone at PFD21 (D) and PFD56 (E) compared to an uninjured control (F). G-I 40  $\mu$ m-thick sagittal sections from (D-F) displaying distribution of Osterix+ progenitors along the thickness of the contralateral parietal bone. J-L MIP of calvarial vessels and Gli1+ skeletal progenitors in the contralateral parietal bone at PFD21 (J) and PFD56 (K) compared to an uninjured control (L). M-O 40  $\mu$ m-thick sagittal sections from (J-K) displaying distribution of Gli1+ progenitors along the thickness of the contralateral parietal bone. White arrows mark regions of skeletal progenitor expansion within the periosteum at PFD21 (D, G, J, M). Images were acquired in 1 calvarium for each experimental group (D-O). P-Q Quantification of skeletal progenitors in the ipsilateral side of the injured parietal bone (gray) compared to the uninjured control (white; n=3). R-S Quantification of skeletal progenitors in the ipsilateral (white) and contralateral sides (gray) of the injured parietal bone compared to the uninjured control (white; n=3 for control, ipsilateral PFD21, ipsilateral and contralateral PFD56; n=1 for contralateral PFD21). Data are mean  $\pm$  SD. Statistics were performed using a one-way ANOVA with Tukey post-hoc test (P, Q). \*\*\*p<0.001, \*p<0.05 where designated. Scale bars: 500  $\mu$ m (D-O). Colors: Red: Endomucin (Emcn), Gray: Osterix (D-I) or Gli1 (J-O), Green: CD31

## 4.4 Conclusion

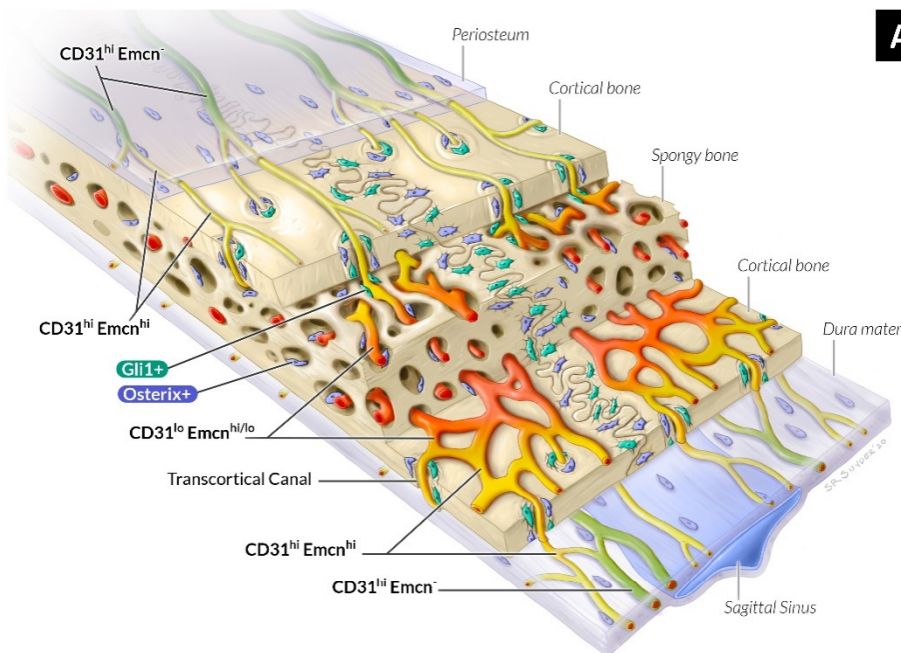
In this Chapter, I investigated how different blood vessel and skeletal progenitor subtypes respond to cranial bone injury. I found that CD31<sup>hi</sup>Emcn<sup>hi</sup> capillaries were the predominant vessel subtype during the early stages of healing and were coupled with a significant expansion of Gli1+

skeletal stem cells across the entire defect area. At the later stages of healing, there was a decline in CD31<sup>hi</sup>Emcn<sup>hi</sup> vessels and skeletal progenitors, but their spatial relationships were maintained. Outside of the defect region, there was a systemic expansion of Gli1+ skeletal stem cells—and Osterix+ osteoprogenitors, to a lesser extent—in the periosteum of the ipsilateral and contralateral parietal bones. These observations suggest that there could be a global response to localized cranial bone injuries, stressing the importance of imaging the entire calvarial structure when evaluating the healing response. Collectively, the results from this Chapter suggest that CD31<sup>hi</sup>Emcn<sup>hi</sup> vessels are coupled with skeletal progenitors during the healing response—especially at the early stages when most bone mineralization takes place—and could be essential for proper cranial bone healing.

# Chapter 5 : Conclusions and Future Perspectives

## 5.1 Conclusions and Impact

Intimate spatial interactions between blood vessels and skeletal progenitors are essential for proper bone growth, remodeling, and healing, but it remains unclear how these relationships manifest in craniofacial bones. In this thesis, I provide a foundational framework for understanding how distinct vessel phenotypes and skeletal progenitors spatially interact in the calvarium (**Figure 5.1**).



**A**

**Figure 5.1: Schematic representing the spatial distribution and prevalence of vessels and skeletal progenitors in the calvarium. A** Illustration showing the relative locations of the vessel and skeletal progenitor subtypes in the parietal bones from 4-weeks-old mice, as derived from **Figure 2.4**. **B** Table demonstrating how the fractional volume of vessel subtypes and number of skeletal progenitors change during postnatal growth, alterations to remodeling, and healing.

**B**

	Blood Vessel Volume Fraction			Number of Cells	
	CD31 <sup>hi</sup> Emcn <sup>-</sup>	CD31 <sup>hi</sup> Emcn <sup>hi</sup>	CD31 <sup>lo</sup> Emcn <sup>hi</sup>	Osterix+	Gli1+
Adulthood	↓	-	-	↓↓↓	↓↓
PTH Administration	-	-	-	↑↑	-
Pdgfb <sup>CKO</sup> in Trap+ Osteoclasts	↑↑	↓↓↓	-	-	-
Healing (Early compared to late stage)	↓↓	↑↑	-	↑↑	↑↑↑

In long bone, recent studies have discovered distinct capillary subtypes—characterized by their expression of CD31 and endomucin (Emcn)—that exhibit divergent spatial relationships to active sites of bone growth and remodeling<sup>50,51</sup>. CD31<sup>hi</sup>Emcn<sup>hi</sup> vessels are spatially associated with Osterix+ osteoprogenitors, provide signaling cues to support osteoprogenitors and perivascular cells, and are abundant in the primary spongiosa, periosteum, and endosteum of the long bone<sup>50,55</sup>. By contrast, CD31<sup>lo</sup>Emcn<sup>lo</sup> vessels comprise the sinusoids of the diaphyseal bone marrow, where there are low numbers of osteoprogenitors<sup>50</sup>. CD31<sup>hi</sup>Emcn<sup>hi</sup> vessels couple angiogenesis to osteogenesis in long bone through Notch signaling and secretion of pro-angiogenic factors and are necessary for maintaining bone mass in adulthood<sup>51,62</sup>. Further, it has been shown that a conditional knockout of PDGF-BB in TRAP+ osteoclasts reduces CD31<sup>hi</sup>Emcn<sup>hi</sup> vessels in the periosteum and bone marrow and disrupts angiogenic-osteogenic coupling<sup>55</sup>. Collectively, these studies demonstrate the necessity of maintaining CD31<sup>hi</sup>Emcn<sup>hi</sup> vessels to support proper growth and remodeling in long bone.

The studies in this thesis sought to characterize the distribution of vessel subtypes in the calvarium and determine whether a similar preferential spatial relationship between CD31<sup>hi</sup>Emcn<sup>hi</sup> vessels and skeletal progenitors exists in cranial bone. First, we developed a 3D quantitative light-sheet imaging platform that illustrates the calvarial microvascular environment at a scale and resolution superior to other techniques. The most widely used imaging modalities used to study calvarial vasculature—immunohistochemistry and intravital microscopy—only allow for visualization of small regions and do not reflect the distinct 3D microenvironments in different regions of the calvarium. Recent advances in light-sheet imaging have enabled visualization of bone vasculature and cells over larger volumes, but these methods rely on endogenous fluorescence and do not allow for simultaneous visualization of multiple cellular markers<sup>12,13</sup>. Our light-sheet imaging platform overcomes these limitations by combining whole-mount immunostaining with an optical clearing reagent compatible with a wide range of antibodies and fluorophores—including endogenous fluorescent



proteins<sup>80,125,126</sup>—and enables the study of spatial interactions between a variety of cell types. Even though our method requires long immunostaining incubations (2-3 weeks), our platform does not require decalcification or complex clearing processes—both of which generally take at least one week to perform<sup>12,127</sup>. Furthermore, our semi-automated quantitative pipeline allows for high-throughput and consistent analysis of large datasets (>100 GB)—a challenging feat due to the advanced computational requirements for processing 3D light-sheet images. Our versatile imaging platform can be readily adapted to unveil other elusive biological phenomena in cranial bone biology that have been difficult to study with established techniques.

Using our imaging method, we present high-resolution 3D maps that illustrate the regional diversity in vessel phenotypes and skeletal progenitor populations. Prior to this report, studies have been limited to showing vessels and cells in small regions of the calvarium, and it was unclear how these structures are distributed through the entire volume. Our experiments demonstrate that most arteries and arterioles—high in CD31 and negative in *Emcn* expression<sup>83</sup>—are present in the periosteum and dura mater, while CD31<sup>hi</sup>*Emcn*<sup>hi</sup> capillaries connect arterioles to bone marrow sinusoids via transcortical canals. Transcortical vessels and marrow sinusoids are primarily located near the sutures during adolescence, but they further develop toward the center of the frontal and parietal bones during cranial maturation. We also show that skeletal progenitors are concentrated at select regions near CD31<sup>hi</sup>*Emcn*<sup>hi</sup> vessels—particularly at the transcortical canals and osteogenic fronts—and that Osterix+ osteoprogenitors are prevalent in the periosteal layers during active periods of bone growth. These regional differences reflect the importance of characterizing the microvascular environment throughout the calvarium as opposed to select areas of interest.

Our study is the first to demonstrate that Gli1+ skeletal stem cells exhibit an intimate spatial relationship with CD31<sup>hi</sup>*Emcn*<sup>hi</sup> vessels in bone. Previous studies have shown that Gli1+ skeletal stem cells mainly reside in the calvarial sutures<sup>33,128,129</sup>, and reported that they are not associated with

vasculature<sup>33</sup>. However, our results suggest that a subset of these cells is associated with CD31<sup>hi</sup>Emcn<sup>hi</sup> vasculature—particularly near the transcortical canals and marrow cavities, where there were also high concentrations of Osterix+ progenitors. Additionally, the Gli1 protein expression was brighter and more concentrated at the transcortical canals compared to the sutures. The discrepancy between this finding and earlier reports highlights the advantages intrinsic to using our established method to visualize these cells: Prior studies primarily used transgenic reporter mice to label skeletal stem cells—a method less sensitive to differences in protein expression levels compared to antibody staining<sup>130</sup>. Additionally, these studies used thin tissue sections to characterize Gli1+ cell distribution, making it difficult to capture the transcortical canals in calvarial bone<sup>28</sup>.

Our results also demonstrate key differences in the relationship between Osterix+ osteoprogenitors and CD31<sup>hi</sup>Emcn<sup>hi</sup> vessels in the calvarium compared to long bone. While we found that Osterix+ osteoprogenitors are preferentially associated with CD31<sup>hi</sup>Emcn<sup>hi</sup> vessels, the volume of these vessels was not directly correlated with the total number of Osterix+ cells. In our experiments evaluating post-natal growth, we found that Osterix+ cell number was higher in the calvaria of juvenile mice compared to adult mice, yet CD31<sup>hi</sup>Emcn<sup>hi</sup> volume remained the same in both groups. Similarly, when exploring stimulated remodeling via PTH administration, we found that the number of Osterix+ cell was greater in PTH-treated versus non-PTH-treated mice, without concomitant changes in the volume of CD31<sup>hi</sup>Emcn<sup>hi</sup> vessels. These findings differ from those observed in long bone, where increases of CD31<sup>hi</sup>Emcn<sup>hi</sup> vessels lead to higher Osterix+ osteoprogenitor numbers and bone mineral deposition<sup>68,69</sup>. The distinct niches that are present in long bone versus the calvarium may account for this discrepancy. In instances when Osterix+ cells were elevated in the calvarium, much of the increase occurred in the periosteum and dura mater, where CD31<sup>hi</sup>Emcn<sup>hi</sup> vessels appeared to have a less direct spatial relationship with osteoprogenitors. By contrast, most studies in long bone have evaluated vessels in the metaphyseal region adjacent to the growth plates—an anatomical feature that is not present in

calvarial bone. These differences demonstrate the necessity in studying angiogenic-osteogenic coupling in cranial bone separately from other bone types.

Additionally, we found that osteoclast signaling may be important for maintaining the spatial relationship of CD31<sup>hi</sup>Emcn<sup>hi</sup> vessels and skeletal progenitors in the calvarium. When we employed a mouse model where PDGF-BB is conditionally knocked out in TRAP+ osteoclasts, the percentage of Osterix+ and Gli1+ progenitors in close proximity (<5 μm) to CD31<sup>hi</sup>Emcn<sup>hi</sup> vessels significantly decreased despite the total number of each cell type remaining the same. These data are similar to trends observed in long bone, where loss of TRAP+ cell-secreted PDGF-BB reduces the number of CD31<sup>hi</sup>Emcn<sup>hi</sup> vessels and migration of periosteal skeletal progenitors to the cortical bone surface<sup>55,56</sup>. In the calvarium, loss of this spatial coupling was most apparent at the transcortical canals. Other studies have shown that osteoclasts are important for maintaining the structure and function of these canals as channels for vascular-mediated nutrient and immune cell transport<sup>27,28</sup>. Furthermore, a recent study has demonstrated that vessel-associated osteoclasts at the primary spongiosa are critical for maintaining CD31<sup>hi</sup>Emcn<sup>hi</sup> vessel homeostasis in the metaphysis<sup>58</sup>. Given the strong association of osteoclasts to CD31<sup>hi</sup>Emcn<sup>hi</sup> vessels in the bone marrow and transcortical canals, our experimental observations suggest that osteoclasts support a regenerative niche for cranial bone growth and remodeling.

With regards to bone healing, our study provides insights into the contributions of vessel phenotypes and skeletal progenitors to cranial bone regeneration. While studies have documented spatial relationships between blood vessels and osteoblasts during calvarial healing<sup>77,88</sup>, it has remained unclear whether specific vessel phenotypes are involved with this process. We found that the majority of vessels present at the early stages of healing (PFD21) were high in CD31 and Emcn expression—the stage at which most bone mineral deposition also took place. Furthermore, CD31<sup>hi</sup>Emcn<sup>hi</sup> vessels were most associated with Gli1+ and Osterix+ cells within the defects at early and later stages of healing, despite the fact that CD31<sup>hi</sup>Emcn<sup>hi</sup> vessels had regressed at PFD56. Provided that little bone formed

between PFD21 and PFD56, our data suggest that CD31<sup>hi</sup>Emcn<sup>hi</sup> vessels may be critical in driving calvarial defect healing.

We also found that Gli1+ cells systemically expanded following injury—an observation that has not been previously documented. Other studies have suggested that cranial skeletal stem cells—including Gli1+ cells—migrate from the sutures to the surrounding bone following injury<sup>33,117,118</sup>. Furthermore, studies have shown that stem cells in the periosteum expand and contribute to calvarial defect healing<sup>76,124</sup>. However, these studies only evaluated regions near the site of injury, and it was unknown whether skeletal progenitors expanded in non-injured areas of the calvarium. In our experiments, Gli1+ cells proliferated in the periosteum over and around the defect site, as well as nearby the sagittal and coronal sutures. At PFD56, we observed excess mineral deposits along the superficial cortical surface of uninjured bone, suggesting that this systemic response contributed to bone mineral deposition outside of the defect region. These observations provide a rationale for future studies to evaluate the effects of this systemic healing response to determine how it impacts calvarial structure and function.

This thesis provides an essential foundation for studying calvarial bone that will enable others to build upon our findings and progress the field of craniofacial bone biology. While we have provided detailed insight into the spatial coupling of skeletal progenitors to vessel phenotypes, there still remains significant knowledge gaps in how other cell types, such as neurons and immune cells, contribute to angiogenic-osteogenic coupling during calvarial growth, healing, and remodeling. Our versatile and inexpensive platform can be readily adapted to observe these different cell types and systematically study a variety of biological processes in the calvarium. Harnessing the powerful capabilities of our 3D quantitative imaging approach will broaden our understanding of craniofacial bone biology and accelerate the development of effective treatments for debilitating craniofacial bone injuries and disorders.

## 5.2 Future Directions

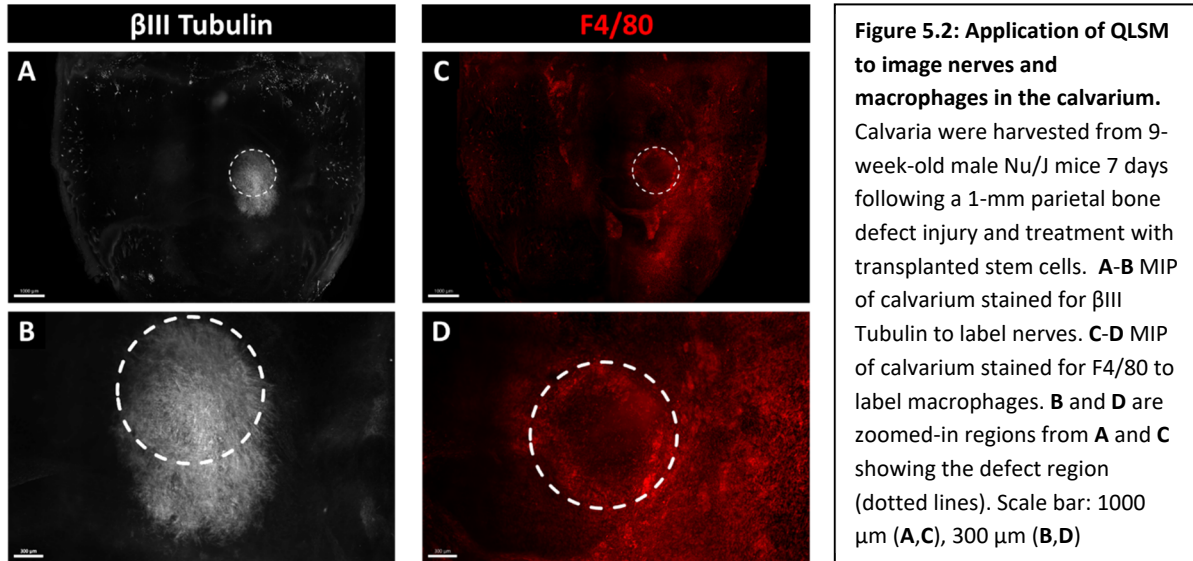
While this thesis focused on developing an imaging platform to better understand how blood vessels interact with skeletal progenitors in cranial bone, numerous potential future directions can be pursued to build upon our findings. In this section, I outline three research avenues that would help provide a broader understanding of how cranial bone grows and heals to aid in the advancement of regenerative therapies.

### 5.2.1 Mapping Nerves and Immune Cells in Native and Injured Calvaria

Sensory nerves and immune cells are known to be important for angiogenesis and osteogenesis during bone healing. A recent study done by Li *et al.* (2019)<sup>65</sup> showed that adequate vascularization and mineralization during bone fracture healing was dependent upon early innervation by sensory nerves (nerve infiltration happened within 3 days). Likewise, Meyers *et al.* (2020)<sup>131</sup> found that sensory nerves infiltrate frontal bone defects during the first 4 weeks of healing, and inhibiting neural ingrowth significantly reduced bone mineral deposition in the defect. Secretion of nerve growth factor by LysM-expressing monocytes and macrophages was critical for this response, suggesting that neuro-immune interactions may regulate the early stages of cranial bone healing<sup>131</sup>. It has also been shown that macrophages are important for stimulating CD31<sup>hi</sup>Emcn<sup>hi</sup> vessel formation during long bone fracture healing<sup>66</sup>. These studies collectively suggest that sensory nerves and immune cells could play a role in regulating the angiogenic-osteogenic coupling processes during cranial bone healing. Of note, the current approaches, such as classical confocal immunofluorescence staining, are difficult to visualize intact nerve fibers and their distribution in bone clearly. Therefore, our established QLSM platform can be readily adapted to assess the cranial bone innervation during bone healing.

Given the potential importance of nerves and immune cells in cranial bone healing, future studies should explore the interactions of these cell types with blood vessels and skeletal progenitors.

Our QLSM platform can be adapted to study these different cell populations by using antibodies specific to each cell type, such as  $\beta$ III-tubulin for neurons and F4/80 for macrophages (**Figure 5.2**). Maps should be created both in uninjured and injured bone to understand the prevalence and spatial distribution of these cells during homeostasis and healing. These experiments would help identify which specific cell populations are involved in the angiogenic-osteogenic coupling processes in cranial bone.



## 5.2.2 Studying Cellular Response to Transplanted Stem Cells and Biomaterials During Cranial Bone Healing

Tissue engineering therapies are a promising avenue for treating critical-sized cranial bone defects, but there is a lack of fundamental understanding of how transplanted stem cells, biomaterials, and host cells interact during the regenerative process. QLSM could provide a more robust method for assessing cranial bone regeneration in tissue-engineered grafts by enabling the analysis of cell-cell and cell-biomaterial interactions throughout the implant region. For instance, in preliminary experiments, I have successfully used QLSM to study the interactions of blood vessels and transplanted adipose-derived stem cells administered within a fibrin hydrogel (**Figure 5.3**). QLSM enabled us to track the fate of transplanted stem cells over time and analyze their spatial relationship to blood vessels in the defect

region. Future studies should build upon this approach to study how transplanted stem cells and different types of biomaterials affect the cranial bone healing response. These data would provide tremendous insight into the mechanisms of cranial bone regeneration and would accelerate the optimization of bone graft design for clinical application.

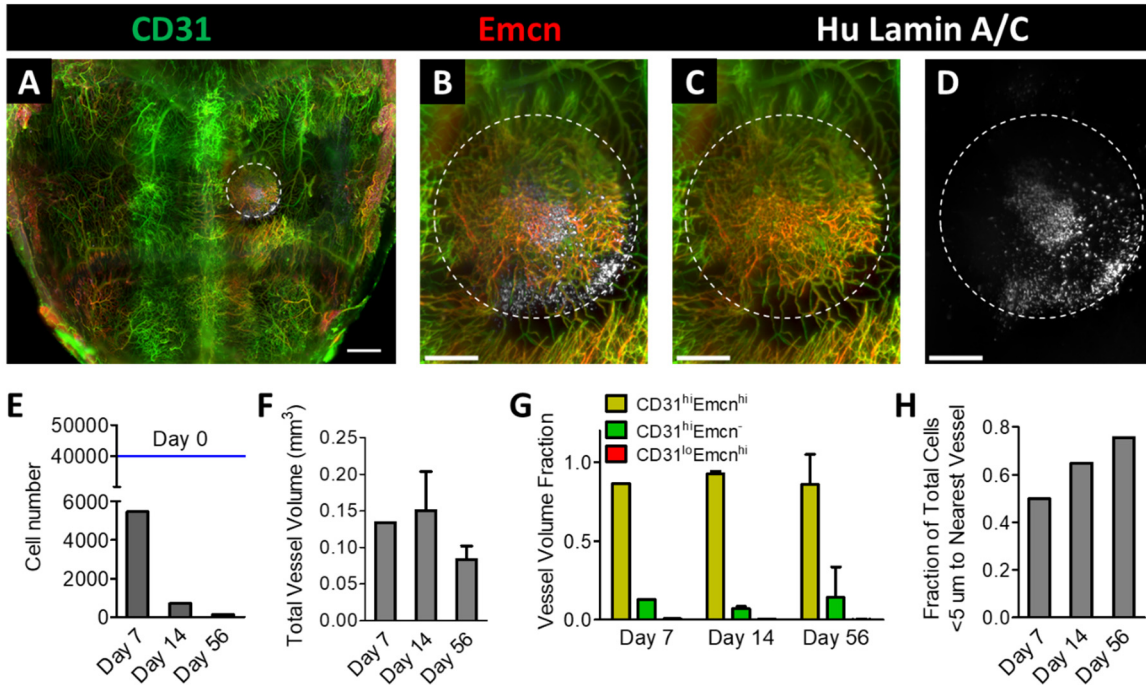


**Figure 5.3: Application of QLSM to study the interactions of transplanted stem cells and blood vessels following injury.** 1-mm parietal bone defects were created in 8-week-old male Nu/J mice and were immediately treated with transplanted human adipose-derived stem cells in a fibrin gel carrier. Calvaria were harvested at 1-, 2-, and 8-weeks post-injury. **A-D** Representative image displaying blood vessels (CD31 and Emcn) and transplanted human stem cells (Human Lamin A/C) at 7 days following injury and transplantation. **E-H** Quantification in the defect region of transplanted stem cell number (**E**), total vessel volume (**F**), volume fraction of different vessel subtypes (**G**), and fraction of transplanted stem cells within 5 μm of their nearest blood vessel (**H**). Data are mean ± SD with n=1 or 2. Scale bar: 1000 μm (**A**), 400 μm (**B-D**)

## 5.2.3 Adapting Quantitative Light-sheet Microscopy to Study the Human Skull

### Microvasculature

While much insight can be gained about the cranial microvascular environment using murine models, it will be important to confirm these findings in the human skull. Some clearing protocols have been developed in human bone to visualize macrophages and blood vessels in and nearby the

transcortical canals<sup>28,132</sup>. However, these studies visualized only two molecular markers simultaneously and imaged with small fields of view, so it is unclear whether their methods would be adequate to study the spatial relationships of different cell types, such as blood vessels and skeletal progenitors. Therefore, the methods presented in this thesis should be adapted to stain, clear, and image large bone tissues (>1 cm<sup>3</sup>) in order to visualize and analyze the human cranial microvascular environment. If successful, this research would revolutionize our understanding of the cellular microenvironments in the human skull during homeostatic and pathological conditions.



# Bibliography

1. Filipowska, J., Tomaszewski, K. A., Niedźwiedzki, Ł., Walocha, J. A. & Niedźwiedzki, T. The role of vasculature in bone development, regeneration and proper systemic functioning. *Angiogenesis* (2017). doi:10.1007/s10456-017-9541-1
2. Percival, C. J. & Richtsmeier, J. T. Angiogenesis and intramembranous osteogenesis. *Developmental Dynamics* (2013). doi:10.1002/dvdy.23992
3. Wiszniak, S. *et al.* Neural crest cell-derived VEGF promotes embryonic jaw extension. *Proc. Natl. Acad. Sci. U. S. A.* (2015). doi:10.1073/pnas.1419368112
4. Robinson, L. K., Hoyme, H. E., Edwards, D. K. & Jones, K. L. Vascular pathogenesis of unilateral craniofacial defects. *J. Pediatr.* (1987). doi:10.1016/S0022-3476(87)80074-4
5. Hill, C. *et al.* Cranial neural crest deletion of VEGFa causes cleft palate with aberrant vascular and bone development. *Cell Tissue Res.* (2015). doi:10.1007/s00441-015-2150-7
6. Copeland, A. E. *et al.* Clinical significance of venous anomalies in syndromic craniosynostosis. *Plast. Reconstr. Surg. - Glob. Open* (2018). doi:10.1097/GOX.0000000000001613
7. Fang, T. D. *et al.* Angiogenesis is required for successful bone induction during distraction osteogenesis. *J. Bone Miner. Res.* (2005). doi:10.1359/JBMR.050301
8. Hyzy, S. L. *et al.* Inhibition of angiogenesis impairs bone healing in an in vivo murine rapid resynostosis model. *J. Biomed. Mater. Res. - Part A* (2017). doi:10.1002/jbm.a.36137
9. Lo Celso, C. *et al.* Live-animal tracking of individual haematopoietic stem/progenitor cells in their niche. *Nature* **457**, 92–96 (2009).
10. Spencer, J. A. *et al.* Direct measurement of local oxygen concentration in the bone marrow of live animals. *Nature* (2014). doi:10.1038/nature13034
11. Bixel, M. G. *et al.* Flow Dynamics and HSPC Homing in Bone Marrow Microvessels. *Cell Rep.* **18**, 1804–1816 (2017).
12. Greenbaum, A. *et al.* Bone CLARITY: Clearing, imaging, and computational analysis of osteoprogenitors within intact bone marrow. *Sci. Transl. Med.* **9**, (2017).
13. Jing, D. *et al.* Tissue clearing of both hard and soft tissue organs with the pegasos method. *Cell Res.* (2018). doi:10.1038/s41422-018-0049-z
14. Wilkie, A. O. M. & Morriss-Kay, G. M. Genetics of craniofacial development and malformation. *Nat. Rev. Genet.* **2001 26 2**, 458–468 (2001).
15. Anderson, B. W., Kortz, M. W. & Kharazi, K. A. Al. Anatomy, Head and Neck, Skull. *StatPearls* (2021).
16. Barreto, S., González-Vázquez, A., Cameron, R. A., O'Brien, F. J. & Murray, D. J. Identification of stiffness-induced signalling mechanisms in cells from patent and fused sutures associated with craniosynostosis. *Sci. Reports* **2017 71 7**, 1–12 (2017).

17. Badve, C. A., Mallikarjunappa, M. K., Iyer, R. S., Ishak, G. E. & Khanna, P. C. Craniosynostosis: Imaging review and primer on computed tomography. *Pediatr. Radiol.* **43**, 728–742 (2013).
18. Russell, W. P. & Russell, M. R. Anatomy, Head and Neck, Coronal Suture. *StatPearls* (2020).
19. Marathe, R. S., Yogesh, A. S., Pandit, S. V., Joshi, M. & Trivedi, G. N. Inca - interparietal bones in neurocranium of human skulls in central India. *J. Neurosci. Rural Pract.* **1**, 14 (2010).
20. Slater, B. J. *et al.* Cranial sutures: A brief review. *Plast. Reconstr. Surg.* **121**, (2008).
21. Nahian, A. & Chauhan, P. R. Histology, Periosteum And Endosteum. *StatPearls* (2021).
22. Woldenberg, R. F. & Kohn, S. A. Dura Mater. *Encycl. Neurol. Sci.* 1039–1042 (2014). doi:10.1016/B978-0-12-385157-4.01143-X
23. Gagan, J. R., Tholpady, S. S. & Ogle, R. C. Cellular dynamics and tissue interactions of the dura mater during head development. *Birth Defects Res. Part C Embryo Today Rev.* **81**, 297–304 (2007).
24. Levi, B. *et al.* Dura mater stimulates human adipose-derived stromal cells to undergo bone formation in mouse calvarial defects. *Stem Cells* (2011). doi:10.1002/stem.670
25. Gomez, C. K., Schiffman, S. R. & Bhatt, A. A. Radiological review of skull lesions. *Insights Imaging* **9**, 857–882 (2018).
26. Klein, B. M. & Bordonni, B. Anatomy, Head and Neck, Emissary Veins. *StatPearls* (2021).
27. Herisson, F. *et al.* Direct vascular channels connect skull bone marrow and the brain surface enabling myeloid cell migration. *Nat. Neurosci.* (2018). doi:10.1038/s41593-018-0213-2
28. Grüneboom, A. *et al.* A network of trans-cortical capillaries as mainstay for blood circulation in long bones. *Nat. Metab.* (2019). doi:10.1038/s42255-018-0016-5
29. D’Souza, R. N., Ruest, L.-B., Hinton, R. J. & Svoboda, K. K. H. Development of the Craniofacial Complex. *Bone Dev.* 153–181 (2010). doi:10.1007/978-1-84882-822-3\_10
30. Lenton, K. A., Nacamuli, R. P., Wan, D. C., Helms, J. A. & Longaker, M. T. Cranial Suture Biology. *Curr. Top. Dev. Biol.* **66**, 287–328 (2005).
31. Ishii, M., Sun, J., Ting, M. C. & Maxson, R. E. The Development of the Calvarial Bones and Sutures and the Pathophysiology of Craniosynostosis. *Curr. Top. Dev. Biol.* **115**, 131–156 (2015).
32. Tubbs, R. S., Bosmia, A. N. & Cohen-Gadol, A. A. The human calvaria: A review of embryology, anatomy, pathology, and molecular development. *Child’s Nervous System* (2012). doi:10.1007/s00381-011-1637-0
33. Zhao, H. *et al.* The suture provides a niche for mesenchymal stem cells of craniofacial bones. *Nat. Cell Biol.* (2015). doi:10.1038/ncb3139
34. Menon, S. *et al.* Skeletal stem and progenitor cells maintain cranial suture patency and prevent craniosynostosis. *Nat. Commun.* **2021 121 12**, 1–14 (2021).
35. Jin, S. W., Sim, K. B. & Kim, S. D. Development and growth of the normal cranial vault: An embryologic review. *Journal of Korean Neurosurgical Society* (2016). doi:10.3340/jkns.2016.59.3.192

36. Grova, M. *et al.* Models of cranial suture biology. *J. Craniofac. Surg.* **23**, (2012).
37. Noden, D. M. & Trainor, P. A. Relations and interactions between cranial mesoderm and neural crest populations. *J. Anat.* **207**, 575–601 (2005).
38. Dasgupta, K. & Jeong, J. Developmental biology of the meninges. *genesis* **57**, e23288 (2019).
39. White, H. E., Goswami, A. & Tucker, A. S. The Intertwined Evolution and Development of Sutures and Cranial Morphology. *Front. Cell Dev. Biol.* **9**, 690 (2021).
40. Riddle, R. C., Khatri, R., Schipani, E. & Clemens, T. L. Role of hypoxia-inducible factor-1 $\alpha$  in angiogenic-osteogenic coupling. *J. Mol. Med.* **87**, 583–590 (2009).
41. Mosteo, L. *et al.* The Dynamic Interface Between the Bone Marrow Vascular Niche and Hematopoietic Stem Cells in Myeloid Malignancy. *Front. Cell Dev. Biol.* **9**, 418 (2021).
42. Grosso, A. *et al.* It takes two to tango: Coupling of angiogenesis and osteogenesis for bone regeneration. *Front. Bioeng. Biotechnol.* **5**, 68 (2017).
43. Pechak, D. G., Kujawa, M. J. & Caplan, A. I. Morphological and histochemical events during first bone formation in embryonic chick limbs. *Bone* **7**, 441–458 (1986).
44. Pechak, D. G., Kujawa, M. J. & Caplan, A. I. Morphology of bone development and bone remodeling in embryonic chick limbs. *Bone* **7**, 459–472 (1986).
45. Thompson, T. J., Owens, P. D. A. & Wilsont, D. J. Intramembranous osteogenesis and angiogenesis in the chick embryo. *J. Anat.* **166**, 55 (1989).
46. Caplan, A. I. Mesenchymal stem cells. *J. Orthop. Res.* **9**, 641–650 (1991).
47. Caplan, A. I. Mesenchymal stem cells. *J. Orthop. Res.* **9**, 641–650 (1991).
48. Wang, Y. *et al.* The hypoxia-inducible factor  $\alpha$  pathway couples angiogenesis to osteogenesis during skeletal development. *J. Clin. Invest.* (2007). doi:10.1172/JCI31581
49. Shimoda, L. A. 55th Bowditch Lecture: Effects of chronic hypoxia on the pulmonary circulation: Role of HIF-1. *J. Appl. Physiol.* **113**, 1343–1352 (2012).
50. Kusumbe, A. P., Ramasamy, S. K. & Adams, R. H. Coupling of angiogenesis and osteogenesis by a specific vessel subtype in bone. *Nature* **507**, 323–328 (2014).
51. Ramasamy, S. K., Kusumbe, A. P., Wang, L. & Adams, R. H. Endothelial Notch activity promotes angiogenesis and osteogenesis in bone. *Nature* **507**, 376–380 (2014).
52. Kusumbe, A. P., Ramasamy, S. K., Starsichova, A. & Adams, R. H. Sample preparation for high-resolution 3D confocal imaging of mouse skeletal tissue. *Nat. Protoc.* **10**, 1904–1914 (2015).
53. Blanco, R. & Gerhardt, H. VEGF and Notch in tip and stalk cell selection. *Cold Spring Harb. Perspect. Med.* (2013). doi:10.1101/cshperspect.a006569
54. Väänänen, H. K. & Laitala-Leinonen, T. Osteoclast lineage and function. *Arch. Biochem. Biophys.* **473**, 132–138 (2008).
55. Xie, H. *et al.* PDGF-BB secreted by preosteoclasts induces angiogenesis during coupling with osteogenesis. *Nat. Med.* **20**, 1270–1278 (2014).

56. Gao, B. *et al.* Macrophage-lineage TRAP+ cells recruit periosteum-derived cells for periosteal osteogenesis and regeneration. *J. Clin. Invest.* (2019). doi:10.1172/JCI98857
57. Su, W. *et al.* Angiogenesis stimulated by elevated PDGF-BB in subchondral bone contributes to osteoarthritis development. *JCI Insight* (2020). doi:10.1172/jci.insight.135446
58. Romeo, S. G. *et al.* Endothelial proteolytic activity and interaction with non-resorbing osteoclasts mediate bone elongation. *Nat. Cell Biol.* (2019). doi:10.1038/s41556-019-0304-7
59. Liu, X. *et al.* Osteoclasts protect bone blood vessels against senescence through the angiogenin/plexin-B2 axis. *Nat. Commun.* 2021 121 **12**, 1–20 (2021).
60. Cackowski, F. C. & Roodman, G. D. Perspective on the Osteoclast. *Ann. N. Y. Acad. Sci.* **1117**, 12–25 (2007).
61. Cackowski, F. C. *et al.* Osteoclasts are important for bone angiogenesis. *Blood* **115**, 140–149 (2010).
62. Ramasamy, S. K. *et al.* Blood flow controls bone vascular function and osteogenesis. *Nat. Commun.* **7**, 13601 (2016).
63. Xu, R. *et al.* Targeting skeletal endothelium to ameliorate bone loss. *Nat. Med.* 2018 246 **24**, 823–833 (2018).
64. Tomlinson, R. E. *et al.* NGF-TrkA Signaling by Sensory Nerves Coordinates the Vascularization and Ossification of Developing Endochondral Bone. *Cell Rep.* **16**, 2723–2735 (2016).
65. Li, Z. *et al.* Fracture repair requires TrkA signaling by skeletal sensory nerves. *J. Clin. Invest.* (2019). doi:10.1172/JCI128428
66. Stefanowski, J. *et al.* Spatial Distribution of Macrophages During Callus Formation and Maturation Reveals Close Crosstalk Between Macrophages and Newly Forming Vessels. *Front. Immunol.* **10**, 2588 (2019).
67. Lee, S. H. *et al.* Runx2 protein stabilizes hypoxia-inducible factor-1 $\alpha$  through competition with von Hippel-Lindau protein (pVHL) and stimulates angiogenesis in growth plate hypertrophic chondrocytes. *J. Biol. Chem.* **287**, 14760–14771 (2012).
68. Sivaraj, K. K. *et al.* YAP1 and TAZ negatively control bone angiogenesis by limiting hypoxia-inducible factor signaling in endothelial cells. *Elife* (2020). doi:10.7554/eLife.50770
69. Yang, M. *et al.* MiR-497~195 cluster regulates angiogenesis during coupling with osteogenesis by maintaining endothelial Notch and HIF-1 $\alpha$  activity. *Nat. Commun.* **8**, 16003 (2017).
70. McCarthy, I. The Physiology of Bone Blood Flow: A Review. *J. Bone Jt. Surg.* **88**, 4–9 (2006).
71. Sloan, A., Hussain, I., Maqsood, M., Eremin, O. & El-Sheemy, M. The effects of smoking on fracture healing. *Surg.* **8**, 111–116 (2010).
72. Ashcroft, G. P. *et al.* Measurement of blood flow in tibial fracture patients using positron emission tomography. <https://doi.org/10.1302/0301-620X.74B5.1527111> **74**, 673–677 (1992).
73. Tomlinson, R. E. & Silva, M. J. Skeletal Blood Flow in Bone Repair and Maintenance. *Bone Res.* 2013 11 **1**, 311–322 (2013).

74. Wang, D. *et al.* Calvarial Versus Long Bone: Implications for Tailoring Skeletal Tissue Engineering. *Tissue Eng. - Part B Rev.* **26**, 46–63 (2020).
75. Ramasamy, S. K. *et al.* Regulation of Hematopoiesis and Osteogenesis by Blood Vessel–Derived Signals. *Annu. Rev. Cell Dev. Biol.* **32**, 649–675 (2016).
76. AU - Park, D., AU - Spencer, J. A., AU - Lin, C. P. & AU - Scadden, D. T. Sequential In vivo Imaging of Osteogenic Stem/Progenitor Cells During Fracture Repair. *JoVE* e51289 (2014). doi:doi:10.3791/51289
77. Huang, C. *et al.* Spatiotemporal Analyses of Osteogenesis and Angiogenesis via Intravital Imaging in Cranial Bone Defect Repair. *J. Bone Miner. Res.* (2015). doi:10.1002/jbmr.2460
78. Wan, C. *et al.* Role of HIF-1 $\alpha$  in skeletal development. in *Annals of the New York Academy of Sciences* (2010). doi:10.1111/j.1749-6632.2009.05238.x
79. De Spiegelaere, W., Cornillie, P., Casteleyn, C., Burvenich, C. & Van den Broeck, W. Detection of Hypoxia Inducible Factors and Angiogenic Growth Factors during Foetal Endochondral and Intramembranous Ossification. *J. Vet. Med. Ser. C Anat. Histol. Embryol.* (2010). doi:10.1111/j.1439-0264.2010.01005.x
80. Coutu, D. L., Kokkaliaris, K. D., Kunz, L. & Schroeder, T. Multicolor quantitative confocal imaging cytometry. *Nat. Methods* **15**, 39–46 (2017).
81. Kusumbe, A. P. *et al.* Age-dependent modulation of vascular niches for haematopoietic stem cells. *Nature* (2016). doi:10.1038/nature17638
82. Acar, M. *et al.* Deep imaging of bone marrow shows non-dividing stem cells are mainly perisinusoidal. *Nat.* 2015 5267571 **526**, 126–130 (2015).
83. Coutu, D. L., Kokkaliaris, K. D., Kunz, L. & Schroeder, T. Three-dimensional map of nonhematopoietic bone and bone-marrow cells and molecules. *Nat. Biotechnol.* **35**, 1202–1210 (2017).
84. Mendez, A. *et al.* Phenotyping the Microvasculature in Critical-Sized Calvarial Defects via Multimodal Optical Imaging. *Tissue Eng. Part C Methods* **24**, 430–440 (2018).
85. Schilling, K. *et al.* Electrospun Fiber Mesh for High-Resolution Measurements of Oxygen Tension in Cranial Bone Defect Repair. *ACS Appl. Mater. Interfaces* (2019). doi:10.1021/acsami.9b08341
86. Vaghela, R., Arkudas, A., Horch, R. E. & Hessenauer, M. Actually Seeing What Is Going on – Intravital Microscopy in Tissue Engineering. *Frontiers in Bioengineering and Biotechnology* (2021). doi:10.3389/fbioe.2021.627462
87. Khosravi, N., DaCosta, R. S. & Davies, J. E. New insights into spatio-temporal dynamics of mesenchymal progenitor cell ingress during peri-implant wound healing: Provided by intravital imaging. *Biomaterials* (2021). doi:10.1016/j.biomaterials.2021.120837
88. Khosravi, N. *et al.* Intravital imaging for tracking of angiogenesis and cellular events around surgical bone implants. *Tissue Eng. - Part C Methods* (2018). doi:10.1089/ten.tec.2018.0252
89. Ortinau, L. C. *et al.* Identification of Functionally Distinct Mx1+ $\alpha$ SMA+ Periosteal Skeletal Stem Cells. *Cell Stem Cell* **25**, 784-796.e5 (2019).

90. Ueda, H. R. *et al.* Tissue clearing and its applications in neuroscience. *Nature Reviews Neuroscience* (2020). doi:10.1038/s41583-019-0250-1
91. Power, R. M. & Huisken, J. A guide to light-sheet fluorescence microscopy for multiscale imaging. *Nature Methods* (2017). doi:10.1038/nmeth.4224
92. Stelzer, E. H. K. *et al.* Light sheet fluorescence microscopy. *Nat. Rev. Methods Prim.* 2021 11 1, 1–25 (2021).
93. Langen, U. H. *et al.* Cell-matrix signals specify bone endothelial cells during developmental osteogenesis. *Nat. Cell Biol.* (2017). doi:10.1038/ncb3476
94. Novotny, L. & Hecht, B. Propagation and focusing of optical fields. in *Principles of Nano-Optics* 45–88 (Cambridge University Press, 2006). doi:10.1017/CBO9780511813535.004
95. Gaussian beams, explained by RP Photonics Encyclopedia; laser beam, fundamental transverse modes. Available at: [https://www.rp-photonics.com/gaussian\\_beams.html](https://www.rp-photonics.com/gaussian_beams.html). (Accessed: 10th August 2021)
96. Shi, Y. *et al.* Gli1 identifies osteogenic progenitors for bone formation and fracture repair. *Nat. Commun.* (2017). doi:10.1038/s41467-017-02171-2
97. Marenzana, M. & Arnett, T. R. The Key Role of the Blood Supply to Bone. *Bone Res.* 2013 11 1, 203–215 (2013).
98. Li, C. *et al.* Disruption of LRP6 in osteoblasts blunts the bone anabolic activity of PTH. *J. Bone Miner. Res.* (2013). doi:10.1002/jbmr.1962
99. Neer, R. M. *et al.* Effect of Parathyroid Hormone (1-34) on Fractures and Bone Mineral Density in Postmenopausal Women with Osteoporosis. *N. Engl. J. Med.* (2001). doi:10.1056/nejm200105103441904
100. Elder, M. *Advanced Orthopedic Technologies, Implants and Regenerative Products.* (2014).
101. Kalluri, L. & Duan, Y. Biomaterials for Bone Grafting and Craniofacial Bone Regeneration. in *Advances in Dental Implantology using Nanomaterials and Allied Technology Applications* (2021). doi:10.1007/978-3-030-52207-0\_6
102. Lee, F. H., Shen, P. C., Jou, I. M., Li, C. Y. & Hsieh, J. L. A population-based 16-year study on the risk factors of surgical site infection in patients after bone grafting. *Med. (United States)* (2015). doi:10.1097/MD.0000000000002034
103. Schmitz, J. P. & Hollinger, J. O. The critical size defect as an experimental model for craniomandibulofacial nonunions. *Clin. Orthop. Relat. Res.* (1986). doi:10.1097/00003086-198604000-00036
104. Schemitsch, E. H. Size Matters: Defining Critical in Bone Defect Size! *J. Orthop. Trauma* 31, S20–S22 (2017).
105. Cowan, C. M. *et al.* Adipose-derived adult stromal cells heal critical-size mouse calvarial defects. *Nat. Biotechnol.* (2004). doi:10.1038/nbt958
106. Aalami, O. O. *et al.* Applications of a mouse model of calvarial healing: Differences in regenerative abilities of juveniles and adults. *Plast. Reconstr. Surg.* 114, 713–720 (2004).

107. Murphy, M. P., Quarto, N., Longaker, M. T. & Wan, D. C. Calvarial Defects: Cell-Based Reconstructive Strategies in the Murine Model. *Tissue Eng. - Part C Methods* **23**, 971–981 (2017).
108. Cooper, G. M. *et al.* Testing the critical size in calvarial bone defects: Revisiting the concept of a critical-size defect. *Plast. Reconstr. Surg.* **125**, 1685–1692 (2010).
109. Quarto, N. *et al.* Origin matters: Differences in embryonic tissue origin and Wnt signaling determine the osteogenic potential and healing capacity of frontal and parietal calvarial bones. *J. Bone Miner. Res.* **25**, 1680–1694 (2010).
110. Wan, D. C. *et al.* Global age-dependent differences in gene expression in response to calvarial injury. *J. Craniofac. Surg.* **19**, 1292–1301 (2008).
111. Charles, L. F. *et al.* Effects of low dose FGF-2 and BMP-2 on healing of calvarial defects in old mice. *Exp. Gerontol.* **64**, 62–69 (2015).
112. Clark, D., Nakamura, M., Miclau, T. & Marcucio, R. Effects of Aging on Fracture Healing. *Curr. Osteoporos. Rep.* **15**, 601–608 (2017).
113. Behr, B., Panetta, N. J., Longaker, M. T. & Quarto, N. Different endogenous threshold levels of Fibroblast Growth Factor-ligands determine the healing potential of frontal and parietal bones. *Bone* **47**, 281–294 (2010).
114. Zhang, L. *et al.* Frontal bone healing is sensitive to wnt signaling inhibition via lentiviral-encoded beta-catenin short hairpin RNA. *Tissue Eng. - Part A* **24**, 1742–1752 (2018).
115. Li, S. *et al.* Enhanced Activation of Canonical Wnt Signaling Confers Mesoderm-Derived Parietal Bone with Similar Osteogenic and Skeletal Healing Capacity to Neural Crest-Derived Frontal Bone. *PLoS One* **10**, e0138059 (2015).
116. Li, S., Meyer, N. P., Quarto, N. & Longaker, M. T. Integration of Multiple Signaling Regulates through Apoptosis the Differential Osteogenic Potential of Neural Crest-Derived and Mesoderm-Derived Osteoblasts. *PLoS One* **8**, e58610 (2013).
117. Wilk, K. *et al.* Postnatal Calvarial Skeletal Stem Cells Expressing PRX1 Reside Exclusively in the Calvarial Sutures and Are Required for Bone Regeneration. *Stem Cell Reports* (2017). doi:10.1016/j.stemcr.2017.03.002
118. Maruyama, T., Jeong, J., Sheu, T. J. & Hsu, W. Stem cells of the suture mesenchyme in craniofacial bone development, repair and regeneration. *Nat. Commun.* (2016). doi:10.1038/ncomms10526
119. Shanley, L. C., Mahon, O. R., Kelly, D. J. & Dunne, A. Harnessing the innate and adaptive immune system for tissue repair and regeneration: Considering more than macrophages. *Acta Biomater.* **133**, 208–221 (2021).
120. Wang, D. *et al.* Enhanced Calvarial Bone Healing in CD11c-TLR4<sup>-/-</sup> and MyD88<sup>-/-</sup> Mice. in *Plastic and Reconstructive Surgery* (2017). doi:10.1097/PRS.00000000000003206
121. Maruyama, M. *et al.* Modulation of the Inflammatory Response and Bone Healing. *Frontiers in Endocrinology* (2020). doi:10.3389/fendo.2020.00386
122. Bahney, C. S. *et al.* Cellular biology of fracture healing. *Journal of Orthopaedic Research* (2019). doi:10.1002/jor.24170

123. Ko, F. C. & Sumner, D. R. How faithfully does intramembranous bone regeneration recapitulate embryonic skeletal development? *Developmental Dynamics* (2021). doi:10.1002/dvdy.240
124. Ortinau, L. C. *et al.* Identification of Functionally Distinct Mx1+ $\alpha$ SMA+ Periosteal Skeletal Stem Cells. *Cell Stem Cell* (2019). doi:10.1016/j.stem.2019.11.003
125. Aoyagi, Y., Kawakami, R., Osanai, H., Hibi, T. & Nemoto, T. A rapid optical clearing protocol using 2,2'-thiodiethanol for microscopic observation of fixed mouse brain. *PLoS One* (2015). doi:10.1371/journal.pone.0116280
126. Costantini, I. *et al.* A versatile clearing agent for multi-modal brain imaging. *Sci. Rep.* (2015). doi:10.1038/srep09808
127. Matsumoto, K. *et al.* Advanced CUBIC tissue clearing for whole-organ cell profiling. *Nat. Protoc.* (2019). doi:10.1038/s41596-019-0240-9
128. Luo, W. *et al.* Investigation of Postnatal Craniofacial Bone Development with Tissue Clearing-Based Three-Dimensional Imaging. *Stem Cells Dev.* (2019). doi:10.1089/scd.2019.0104
129. Guo, Y. *et al.* BMP-IHH-mediated interplay between mesenchymal stem cells and osteoclasts supports calvarial bone homeostasis and repair. *Bone Res.* (2018). doi:10.1038/s41413-018-0031-x
130. Swenson, E. S., Price, J. G., Brazelton, T. & Krause, D. S. Limitations of Green Fluorescent Protein as a Cell Lineage Marker. *Stem Cells* (2007). doi:10.1634/stemcells.2007-0241
131. Meyers, C. A. *et al.* A Neurotrophic Mechanism Directs Sensory Nerve Transit in Cranial Bone. *Cell Rep.* (2020). doi:10.1016/j.celrep.2020.107696
132. Kolabas, Z. I. *et al.* Multi-omics and 3D-imaging reveal bone heterogeneity and unique calvaria cells in neuroinflammation. *bioRxiv* **18**, 2021.12.24.473988 (2021).



## Appendix I: Key Reagents and Resources

Reagent or resource	Source	Identifier
<b>Antibodies</b>		
Goat anti-mouse/rat CD31 (1:100)	R&D Systems	AF3628
Rat anti-mouse/rat Endomucin (1:50)	Santa Cruz Biotechnology	sc-65495
Rabbit anti-mouse/rat/human Osterix (1:200)	Abcam	ab209484
Rabbit anti-mouse/human Gli1 (1:100)	Sigma Aldrich	SAB4301901-100UL
Rabbit anti-mouse/rat/human Vpp3 (ATP6V1B1 + ATP6V1B2; 1:200)	Abcam	ab200839
Rabbit anti-human Anti-Lamin A + Lamin C antibody (1:500)	Abcam	ab108595
Rabbit anti-mouse/rat/human $\beta$ - Tubulin III (1:100 with 50% glycerol 0.35 mg/mL stock)	Sigma Aldrich	T2200
Rat anti-mouse F4/80 (1:100)	Bio-Rad	MCA497GA
Donkey anti-goat AF800 plus, 0.67 mg/mL, (1:50)	Thermo Fisher Scientific	A32930

<b>Reagent or resource</b>	<b>Source</b>	<b>Identifier</b>
Donkey anti-rabbit AF647 plus, 0.67 mg/mL (1:150)	Thermo Fisher Scientific	A32795
Donkey anti-rat biotin, 0.75 mg/mL (1:100)	Thermo Fisher Scientific	A18749
Streptavidin AF555 conjugate, 0.67 mg/mL (1:100)	Thermo Fisher Scientific	S32355
<b>Reagents</b>		
Heparin sodium salt from porcine mucosa	Sigma Aldrich	H3393-50KU
Paraformaldehyde, 16% aq. soln., methanol free	Alfa Aesar	433689M
Normal donkey serum	Sigma Aldrich	D9663-10ML
Trizma base	Sigma Aldrich	T6066-1KG
Trizma hydrochloride	Sigma Aldrich	T5941-1KG
Sodium chloride	Sigma Aldrich	S5886
Tween 20	Sigma Aldrich	P7949
Dimethylsulfoxide	Thermo Fisher Scientific	PI20688
Streptavidin/Biotin Blocking Kit	Vector Laboratories	SP-2002

<b>Reagent or resource</b>	<b>Source</b>	<b>Identifier</b>
2,2-thiodiethanol	Sigma Aldrich	166782-500G
<b><i>Animal drugs and materials</i></b>		
Ketamine HCl (100 mg/mL)	VetOne	501072
Xylazine Injection (20 mg/mL)	Akorn, Inc.	N/A
pTH (1-34)	Bachem	4011474
Povidone-Iodine Swabsticks	Fisher Scientific	06-669-83
6-0 nylon monofilament sutures	Ethicon	1665G
Buprenorphine SR-LAB (0.5 mg/mL)	ZooPharm	N/A
Ideal Micro-Drill	Harvard Apparatus	72-6065
1 mm carbide inverted cone burr	Roboz Surgical Instrument Co.	RS-6282C-35
Stereotactic frame	KOPF, David Kopf Instruments	900LS
Surgical microscope	Carl Zeiss	NC-4
<b><i>Instruments and hardware</i></b>		
Ultramicroscope II, 2x zoom body configuration	Miltenyi Biotec (formerly manufactured by LaVision Biotec)	N/A
LVMI-Fluor 2x objective lens with dipping cap (0.5 NA, 1.33-1.57 RI range, 5.6 mm WD)	Miltenyi Biotec (formerly manufactured by LaVision Biotec)	N/A

<b>Reagent or resource</b>	<b>Source</b>	<b>Identifier</b>
Dell Precision 7820 Tower	Dell	T7820X
Portable SSD T5 USB 3.1 2 TB	Samsung	MU-PA2T0B
Skyscan 1275 $\mu$ CT	Bruker	N/A
<b><i>Software</i></b>		
Imaris 9.5 Single Full with ClearView plus Stitcher	Bitplane Inc.	N/A
XiT	See ref. [80]	N/A
CTAn, CTVol, and CTVox	Bruker	N/A
Mimics 14	Materialise	N/A
Microsoft Excel 2019	Microsoft	N/A
GraphPad Prism 5	GraphPad Software	N/A

# Appendix II: List of Publications

## Publications completed during my PhD:

1. Rindone AN\*, Liu X, Farhat S, Perdomo-Pantoja A, Witham TF, Coutu DL, Wan M, Grayson WL. "Quantitative 3D Imaging of the Cranial Microvascular Environment at Single-Cell Resolution." *Nature Communications* 12, 1-13 (2021). \*Introduction and Chapters 2-5 are adapted from this publication.
2. Rindone AN, Grayson WL. "Illuminating the Regenerative Microenvironment: Emerging Quantitative Imaging Technologies for Craniofacial Bone Tissue Engineering." *ACS Biomaterials Science & Engineering*. In press.
3. Singh S, Nyberg EL, O'Sullivan AN, Farris A, Rindone AN, Zhang N, Whitehead EC, Zhou Y, Mihaly E, Achebe CC, Zbijewski W, Grundy W, Garlick D, Jackson ND, Taguchi T, Takawira C, Lopez J, Lopez MJ, Grant MP, Grayson WL. "Point-of-Care Treatment of Geometrically Complex Midfacial Critical-Sized Bone Defects with 3D-Printed Scaffolds and Autologous Stromal Vascular Fraction." *Biomaterials*. In press.
4. Farris AL, Lambrechts D, Zhou Y, Zhang NY, Sarkar N, Moorner MC, Rindone AN, Nyberg EL, Perdomo-Pantoja A, Burris SJ, Free K, Witham TF, Riddle RC, Grayson WL. "3D-printed oxygen-releasing scaffolds improve bone regeneration in mice." *Biomaterials* 280, 121318 (2021).
5. Horenberg AL, Rindone AN, Grayson WL. "Engineering Bone from Fat: A Review of the Mechanisms of Adipose Derived Stem Cell-Mediated Bone Regeneration." *Progress in Biomedical Engineering* 3, 042002 (2021).
6. Perdomo-Pantoja A, Holmes C, Cottrill E, Rindone AN, Ishida W, Taylor M, Tomberlin C, Lo SL, Grayson WL, Witham TF. "Comparison of Freshly Isolated Adipose Tissue-derived Stromal Vascular Fraction and Bone Marrow Cells in a Posterolateral Lumbar Spinal Fusion Model." *Spine* 46, 631-637 (2021).
7. Morrissette-McAlmon J, Ginn B, Somers S, Fukunishi T, Thanitcul C, Rindone A, Hibino N, Tung L, Mao HQ, Grayson W. "Biomimetic Model of Contractile Cardiac Tissue with Endothelial Networks Stabilized by Adipose-Derived Stromal/Stem Cells." *Scientific Reports* 10, 8387 (2020).
8. Rindone AN\*, Kachniarz B, Achebe C, O'Sullivan A, Riddle RC, Dorafshar D, Grayson WL. "Heparin-Conjugated Decellularized Bone Particles Promote Enhanced Osteogenic Signaling of PDGF-BB to Adipose-Derived Stem Cells in Tissue Engineered Bone Grafts." *Advanced Healthcare Materials* 8, 1801565 (2019). \*Featured on cover
9. Mendez A, Rindone AN, Batra N, Abbasnia P, Senarathna J, Gil S, Hadjiabadi DH, Grayson WL, Pathak AP. "Phenotyping the Microvasculature in Critical-Sized Calvarial Defects via Multimodal Optical Imaging." *Tissue Engineering Part C* 24, 430-440 (2018).

10. Nyberg E, Rindone A, Dorafshar A, Grayson WL. "Comparison of 3D-Printed Poly-ε-Caprolactone Scaffolds Functionalized with Tricalcium Phosphate, Hydroxyapatite, Bio-Oss, or Decellularized Bone Matrix." *Tissue Engineering Part A* 23, 503-514 (2017).
11. Rindone AN\*, Nyberg E\*, Grayson WL. "3D-Printing Composite Polycaprolactone-Decellularized Bone Matrix Scaffolds for Bone Tissue Engineering Applications." *Methods in Molecular Biology* 1577, 209-226 (2017). \*Co-first authors
12. Farris AL\*, Rindone AN\*, Grayson WL. "Oxygen delivering biomaterials for tissue engineering." *Journal of Materials Chemistry B* 4, 3422-3432 (2016). \*Co-first authors; article featured in "2016 Journal of Materials Chemistry B Hot Papers" collection